Attitude Control of an Underactuated LEO CubeSat in presence of Uncertainties with State Estimation

by

Naeimeh Najafizadeh Sari

August 2022

A thesis

presented to the University of Manitoba

in fulfilment of the

thesis requirement for the degree of

Master of Science

in

Mechanical Engineering

Winnipeg, Manitoba, Canada 2022

©Naeimeh Najafizadeh 2022

Abstract

This thesis addresses the nonlinear attitude control of an underactuated satellite equipped with only three magnetorquers. The problem involves stabilizing the sun-pointing 3U CubeSat in the presence of environmental perturbations and sensor noises from launch separation and deployment until the nominal mode. The sensors include a three-axis gyroscope, a three-axis magnetometer and a two-axis sun sensor.

A detumbling and a proportional-derivative(PD) controller are applied to the underactuated dynamic system. Since a spin-stabilized configuration is naturally stable, a spin-stabilized mode is selected given the spin-axis is a major axis of inertia. Further, a power management strategy has been applied, which requires a small amount of control effort. The proposed linear control law achieves attitude convergence for three-axis stability within the 0.18 degrees attitude error and $1\ deg/s$ spin rate norm.

The design has been implemented using a high fidelity real-time simulation in Simulink/-MATLAB while considering the environmental effects to study the in-orbit behaviour and the effectiveness of the system's stability in overcoming the disturbance torques, including gravity gradient torque, residual dipole torque, dynamic uncertainties, and sensors noise.

Since sun sensors do not provide any measurements in the eclipse, an Extended Kalman Filter (EKF) is embedded in the simulation to give estimates of the attitude angles in the eclipse based on gyroscope measurements. The estimator benefits from a dimension reduction technique to increase the estimation reliability and reduce the onboard computational and power usage.

Numerical simulations successfully corroborate the effectiveness of the controller and the estimator.

Acknowledgments

I would like to express my gratitude first and foremost to my thesis advisor, Dr. Philip Ferguson, for the opportunity to work on the Iris CubeSat project and for his supervision and help during this work and all the immensely valuable lessons.

Further, I would like to thank the members of my dissertation committee - not only for their time and patience, but for their intellectual contributions to my research development.

Additionally, this research would not have been possible without the financial support from the Canadian Space Agency(CSA). I also thank my lab mates in STARLab for their editing help and feedback.

Finally, but not least, I would like to thank my mother who always believed in me and helped me achieve everything I aimed for.

Table of Contents

Abstract **1**

Table of Contents **iii**

List of Tables **vi**

List of Figures **vii**

Chapter 1:

Introduction **1**

1.1 Motivation 1

1.2 Hypotheses and Contributions of Thesis 4

1.3 Literature Review on Hypothesis 1: Magnetic Attitude Control 5

1.4 Literature Review on Hypothesis 2: Attitude Estimation using Kalman Filtering . 8

1.5 Outline of Thesis 10

Chapter 2:

Spacecraft Dynamics **11**

2.1 Iris Mission Description 11

2.2 Coordinate Reference frames 13

2.2.1 Earth Centered Inertial (ECI) frame 13

2.2.2 Satellite Body frame 14

2.2.3 Orbital frame 14

2.3 Attitude Dynamics of a rigid body 15
2.4 Quaternion-derived Rotation Matrix 16

Chapter 3:

Simulation design **18**

3.1 SGP4 Orbit Propagator 19
3.2 Earth Magnetic Field Block 23
3.3 Environment Block 26
3.3.1 Gravity-Gradient Torque 27
3.3.2 Residual Magnetic Torque 28
3.4 Kinematics and Dynamics 30
3.5 Solar Ephemeris 31
3.6 Attitude Determination 33
3.7 Controller Block 36
3.7.1 Detumbling Mode 36
3.7.2 Fine pointing Mode 37
3.7.3 MOI Tensor 40
3.8 Magnetorquers Power Consumption 43
3.9 Power Analysis Block 44
3.10 Summary of the Chapter 47

Chapter 4:

EKF Based Sun Vector Estimation **48**

4.1 System Model 49
4.2 Sun Sensor Representation of Sun Position Vector 51
4.2.1 Dimension Reduction Strategy in EKF 53
4.3 EKF Algorithm and Definitions 55
4.3.1 EKF Model Linearization 57

4.3.2 EKF Model Discretization 60
4.3.3 Estimation Phase 62
4.3.4 Update Phase 63
4.4 Conclusion 64

Chapter 5:

Results and Discussion **65**

5.1 Detumbling Controller Analysis 67
5.1.1 1 Orbit Detumbling 68
5.2 Fine Pointing 71
5.3 Extended Kalman Filter Approach for State Estimation 75
5.3.1 Measurement Noise 76
5.3.2 Process Noise 77
5.3.3 EKF including 2 sensors and 5 states 78
5.4 Attitude Control of Satellite with Power Management Strategy 87
5.5 Real time EKF-based attitude feedback in Simulink 88
5.6 Worst Power Generation Scenario 94
5.7 Conclusion 100

Chapter 6:

Summary and Conclusion **101**

6.1 Future Work 102

Appendix A: Fine Pointing Perturbation Analysis **104**

A.1 Mode 1: Fine Pointing 104
A.2 Mode 2: Fine Pointing 108
A.3 Mode 3: Fine Pointing 110

Bibliography **113**

List of Tables

3.1 TLE Orbital Elements 20

3.2 ADCS Hardware specifications [54] 44

3.3 Power consumption offsets in stowed configuration mode by components 46

3.4 Power consumption offsets in deployed configuration mode by components . . . 46

5.1 Common properties used in all simulations 67

5.2 Detumbling Simulation Summary for various initial body rates 70

5.3 Sensor's properties used in EKF simulation 76

5.4 EKF Estimation Error Summary 84

5.5 Detumbling-Spin Simulation Summary 88

A.1 4 modes of Perturbation Analysis 104

List of Figures

2.1 Illustration of the Iris 3U CubeSat with a sun sensor and sun-facing solar panels . 12

2.2 Iris Orbit visualization in terms of sun lit and eclipse phase 12

2.3 ECI frame 13

2.4 Orbital frame 14

3.1 Simplified block diagram of ADCS simulation 19

3.2 Simplified block diagram of SGP4 propagator algorithm 20

3.3 Schematic of Earth magnetic field 23

3.4 Simplified block diagram of Earth's magnetic field algorithm 23

3.5 Azimuth angle is measured in degrees clockwise from x axis or the North 24

3.6 Simplified block diagram of disturbance torques 27

3.7 Gravitational Force exerted on the satellite regarding Newton's Law of Gravitation 28

3.8 Simplified block diagram of Dynamics algorithm 30

3.9 Simplified block diagram of Kinematics algorithm 31

3.10 Simplified block diagram of B_{body} algorithm 31

3.11 The tilt angle between ECI frame and Elliptic Frame 32

3.12 Simplified block diagram of solar ephemeris algorithm 32

3.13 Simplified block diagram of attitude determination algorithm 34

3.14 Simplified block diagram of EKF Block 35

3.15 Simplified block diagram of controller algorithm 36

3.16 Saturation block will adjust the dipole moment below threshold while preventing actuators saturation at the same time 39

3.17 Negating torque in order to control the angle not to stabilize backward 40
3.18 Iris full assembly stowed 41
3.19 Iris full assembly deployed 42
3.20 Simplified block diagram of torque rod's power algorithm 43
3.21 Simplified block diagram of power analysis algorithm [55] 45

4.1 Geometric representation of the Sun sensor and sun sensor's mask. The unit sun vector is shown with $\hat{s}$ and the angle θ_1 is the satellite's attitude angle towards sun. α is the angle between the sun vector projection and $-x$ axis. Similarly, β is the angle between the sun vector projection on the $x-z$ plane and $-x$ axis. . . . 51
4.2 2D Projection of sun vector on the x-y plane 52
4.3 2D Projection of sun vector on the x-z plane 52
4.4 EKF general flow diagram 56

5.1 ADCS Algorithm Functional Flow Block Diagram 66
5.2 Body rates of Iris during detumbling with initial angular velocity of $[5, 5, 5]\ deg/sec$ after 1 orbit 68
5.3 Torque rod power consumption of satellite during detumbling with initial angular velocity of $[5, 5, 5]\ deg/sec$ after 1 orbit 69
5.4 Noisy measurements of the magnetic Field ($\vec{B}$) strength in the body frame during the first orbit while detumbling measured by the magnetometers 70
5.5 Body rates of Iris during fine pointing with initial angular velocity of $[0.5, 0.5, 0.5]\ deg/sec$ after 15 orbits 71
5.6 Close up view of residual body rates of Iris during fine pointing with initial angular velocity of $[0.5, 0.5, 0.5]\ deg/sec$ after 15 orbits 72
5.7 Attitude angle of satellite during fine pointing with initial angular velocity of $[0.5, 0.5, 0.5]\ deg/sec$ including all perturbation after 15 orbits 73

5.8 A close up view of attitude angle of satellite during fine pointing with initial angular velocity of $[0.5, 0.5, 0.5]$ deg/sec with all perturbation after 15 orbits 73
5.9 A close up view of attitude angle of satellite at 6th orbit during fine pointing with initial angular velocity of $[0.5, 0.5, 0.5]$ deg/sec when the pointing accuracy enters the 21 deg window 74
5.10 Torque rod power consumption of satellite during fine pointing with initial angular velocity of $[0.5, 0.5, 0.5]$ deg/sec with all perturbation after 15 orbits and power management strategy 75
5.11 Sun vector Projection on $y - z$ plane while the sun pointing CubeSat is spinning with $[1, 0, 0]$ deg/sec 77
5.12 Estimated sun attitude vector projection vs sun sensor output within the 4th orbit 79
5.13 A close-up view of estimated sun attitude vector projection vs sun sensor output within the eclipse time of the 4th orbit 80
5.14 Estimation error of sun attitude vector projection within the 4th orbit 80
5.15 A close up view of estimation error of sun attitude vector projection within the illumination phase of the 4th orbit 81
5.16 Square root of estimated error covariance matrix corresponding to sun vector projection during the 1st second 82
5.17 Square root of error covariance matrix corresponding to estimation error of sun attitude vector projection on y and z axes in the 4th orbit 83
5.18 A close up view of estimation error of sun vector projection in y and z axes bounded by square root of the error covariance matrix in 4th orbit 84
5.19 Estimated body rates vs the actual data during the 4th orbit (after spin-up) 85
5.20 A close up view of the estimated body rates vs the actual data during the 4th orbit (after spin-up) 85
5.21 Estimation error of body rates during the 4th orbit (after spin-up) 86

5.22 Square root of error covariance matrix corresponding to body rates during the 1st second 86
5.23 Estimation error of body rates bounded by the square root of error covariance matrix within 4th orbit 87
5.24 Pointing error during detumbling and spin stabilization with initial angular velocity of $[5, 5, 5]\ deg/sec$ within 15 orbits with real time EKF-based attitude feedback from 4th orbit 90
5.25 A close up view of pointing error during spin stabilization with initial angular velocity of $[5, 5, 5]\ deg/sec$ after 15 orbits with real time EKF-based attitude feedback from 3rd orbit 91
5.26 Body rates during detumbling and spin stabilization with initial values of $[5, 5, 5]\ deg/sec$ within 15 orbits with real time EKF-based attitude feedback from 4th orbit 91
5.27 Torque rod power consumption of satellite with initial angular velocity of $[5, 5, 5]\ deg/sec$ with all perturbations after 15 orbits with real time EKF-based attitude feedback and power management strategy 92
5.28 A close-up view of torque rod power consumption on x-axis during the eclipse of fourth orbit with real-time EKF-based attitude feedback 93
5.29 State of charge during detumbling and spin stabilization with initial angular velocity of $[5, 5, 5]\ deg/sec$ within 15 orbits with real time EKF-based attitude feedback from 4th orbit 94
5.30 State of charge of the satellite during worst power scenario with an initial angular velocity of [0,-5,0]deg/sec 96
5.31 Discontinuity in the battery charge current (SOC rate) of the satellite during the solar panel deployments after detumbling (worst power scenario) 96
5.32 Body rates of the satellite during worst power scenario with an initial angular velocity of [0,-5,0]deg/sec 97

5.33 Attitude angle during worst power case scenario with initial angular velocity of [0,-5,0]deg/sec 97
5.34 A close-up view of steady state attitude error during worst power case scenario with an initial angular velocity of [0,-5,0] deg/sec 98
5.35 Torque rod power consumption of satellite with initial angular velocity of $[0, -5, 0]\ deg/sec$ with all perturbations (worst power case) after 15 orbits and power management strategy 99

A.1 Body rates of Iris during detumbling and fine pointing with initial angular velocity of $[5, 5, 5]\ deg/sec$ with no perturbation (Mode 1) after 15 orbits 105
A.2 Attitude Angle of satellite during detumbling and fine pointing with initial angular velocity of $[5, 5, 5]\ deg/sec$ with no perturbation (Mode 1) after 15 orbits . . . 105
A.3 A close up view of attitude angle during detumbling and fine pointing with initial angular velocity of $[5, 5, 5]\ deg/sec$ with no perturbation (Mode 1) after 15 orbits . 106
A.4 Torque rod power consumption of satellite during detumbling with initial angular velocity of $[5, 5, 5]\ deg/sec$ with no perturbation (Mode 1) after 15 orbits and power management strategy 107
A.5 Body rates of Iris during detumbling and fine pointing with initial angular velocity of $[5, 5, 5]\ deg/sec$ with residual dipole torque (Mode 2) after 15 orbits 108
A.6 A close up view of body rates during fine pointing with initial angular velocity of $[5, 5, 5]\ deg/sec$ with with residual dipole torque (Mode 2) after 15 orbits 108
A.7 Attitude Angle of satellite during detumbling and fine pointing with initial angular velocity of $[5, 5, 5]\ deg/sec$ with with residual dipole torque (Mode 2) after 15 orbits 109
A.8 A close up view of attitude angle during spin stabilization with initial angular velocity of $[5, 5, 5]\ deg/sec$ with with residual dipole torque (Mode 2) after 15 orbits 109

A.9 Torque rod power consumption of satellite during detumbling and fine pointing with initial angular velocity of $[5, 5, 5]\ deg/sec$ in mode 2 and power management strategy 110

A.10 Body rates of Iris during detumbling and fine pointing with initial angular velocity of $[5, 5, 5]\ deg/sec$ with residual dipole and gravity gradient torques (Mode 3) after 15 orbits 111

A.12 Steady state attitude angle of satellite during Spin Stabilization with initial angular velocity of $[5, 5, 5]\ deg/sec$ with residual dipole and gravity gradient torques (Mode 3) after 15 orbits 111

A.11 Attitude angle of satellite during detumbling and fine pointing with initial angular velocity of $[5, 5, 5]\ deg/sec$ with residual dipole and gravity gradient torques (Mode 3) after 15 orbits 112

A.13 Torque rod power consumption of satellite during detumbling and fine pointing with initial angular velocity of $[5, 5, 5]\ deg/sec$ in mode 3 and power management strategy 113

Chapter 1

Introduction

The attitude determination and control subsystem (ADCS) of a satellite is vital to accomplishing a space mission. This thesis describes the design and analysis of an ADCS for the Iris CubeSat, the next satellite from the University of Manitoba. This chapter starts with the motivation of the research, which describes the need for transitioning from traditional satellites to CubeSats and further discusses the dynamics and controllability of magnetic actuators. Then the hypothesis and contributions of the research are presented. The chapter closes with an outline of this MSc thesis.

1.1 Motivation

Until 1980 satellites were large, heavy and were made of expensive pieces of hardware, which also included a high degree of redundancy [1]. The governmental agencies and federal budgets mainly funded the spacecraft. Since then, the historical trend of publications and research shows a gradually increasing interest in small satellites [2]. In the year 2000, to promote innovative partnerships with the private sector and to provide a mechanism for affordable technology, governmental space sectors such as NASA and ESA launched small satellite programs [2][3]. Afterward, the budget dedication fell from 4.5% of the federal budget in 1965 to 0.5% federal budget in 2012 in US Civil Space [3]. In the EU, in a survey conducted in 2012 from 8 European companies, 90% of them preferred small systems for future constellations [3]. As a result, the small satellites

that were once introduced into the space industry became enduring and popular as lower-cost alternatives to traditional satellites [4].

Any satellite less than $1000\ kg$ is considered a small satellite [5]. Nanosatellites weigh around $1 - 10\ kg$. A CubeSat is one particular class of nanosatellites that has been gaining popularity in the past decade. It is made up of multiples of $10 \times 10 \times 10\ cm$ cubic units, each with a mass of about $1.5\ kg$ [3]. The popularity is mainly due to the low-cost, commercial off-the-shelf (COTS) reliant design, which improves with increasing computational power and miniaturization of components[6].

Due to inflexible mass, size, and monetary budget requirements, these small satellites depend on low-cost sensors and the most inexpensive actuators, such as torque rods [7][8]. More expensive high-accuracy actuators such as thrusters and reaction wheels often use more onboard power and propellant. Alternatively, torque rods or magnetorquers are compact, simple to manufacture, small in size, lightweight, and have minimal power consumption [9]. For CubeSats, magnetorquer-only control provides significant benefits. These magnetic actuators could be designed according to the geometry of the satellite, contrary to most other actuators [10]. For instance, their size could be adjusted to the dimensions of the units. Moreover, it would also eliminate the jitter associated with reaction wheels [11]. This research uses torque rods to perform a robust attitude control system to point a spacecraft at the sun after deployment from a launch vehicle or following an eclipse.

Many missions have been done on satellites with magnetic torque rods as the only attitude control actuator [12][13][14]. By using only torque rods, controllability is not possible in all three axes at a time, and the system would become underactuated [15].

In mechanics, a magnetically actuated satellite is a nonlinear system with fewer actuators than degrees of freedom. Therefore the system becomes an underactuated system in which not all three axes are controllable at a time, i.e. the uncontrollable axis varies as a function of orbit position, and attitude [16]. This condition is what makes attitude control much more challenging.

In summary, magnetorquers are not ideal for satellites requiring a high degree of pointing

accuracy [17][18]. However, this actuation seems reasonable for CubeSats, which has a modest budget and pointing requirements.

Euler's equation is a starting point to examine an underactuated problem from a mathematical point of view which could represent the dynamics of the rigid spacecraft as follows [19][20]:

$$\vec{T}_{mag} + \vec{T}_d = I\dot{\vec{\omega}} + \vec{\omega} \times I\vec{\omega} \tag{1.1}$$

where $\vec{\omega} \in \mathbb{R}^3$ is the vector of spacecraft angular velocity, expressed in body frame, $I \in \mathbb{R}^{3\times3}$ is the moment of inertia tensor, $\vec{T}_{\text{mag}} \in \mathbb{R}^3$ is the vector of magnetic control torques and $\vec{T}_d \in \mathbb{R}^3$ the vector of external disturbance torques.

The torque rods are assumed to be aligned with the spacecraft's principal axes and generate torque according to the same law as a compass needle [21][22]:

$$\vec{T}_{\text{mag}} = \vec{m} \times \vec{B}_b \tag{1.2}$$

where $\vec{m} \in \mathbb{R}^3$ is the vector of magnetic dipoles for the three coils (which represent the actual control variables for the coils), and $\vec{B}_b \in \mathbb{R}^3$ is the column vector of the Earth's magnetic field in the body frame of reference. The cross product in the above equation can be expressed more simply as a matrix-vector product as:

$$\vec{T}_{\text{mag}} = -\mathbf{B}_b^{\times}\vec{m} \tag{1.3}$$

where $\mathbf{B}_b^{\times}$ is called the skew symmetric matrix. If the $\mathbf{B}_b$ components are as below:

$$\mathbf{B}_b = \begin{bmatrix} b_x \\ b_y \\ b_z \end{bmatrix} \tag{1.4}$$

So the $\mathbf{B}_b^{\times}$ is defined by:

$$\mathbf{B}_b^{\times} = \begin{bmatrix} 0 & -b_z & b_y \\ b_z & 0 & -b_x \\ -b_y & b_x & 0 \end{bmatrix} \tag{1.5}$$

Regarding equation 1.3 magnetorquers-only satellites have a serious control limitation. Mathematically, the challenge of controllability can be expressed as follows. Since $\mathbf{B}_b^{\times}$ can not be inverted so, determining the magnetic dipole ($\vec{m}$) in all three axes is not possible. That is, at each instant, it is impossible to apply a control torque to all three spacecraft axes independently. So the nonlinear dynamic system with three torque rods is called underactuated. To overcome this condition, the control algorithm should be able to dampen the body rates of the CubeSat and provide the proper stability.

1.2 Hypotheses and Contributions of Thesis

The thesis investigates the attitude control techniques of a nonlinear and underactuated spacecraft in its nominal orbit. The satellite uses three torque rods as active magnetic actuators. This study examines a spin-stabilized control strategy and extended Kalman filter to estimate the spacecraft's attitude by adding existing known attitude perturbations and unknown uncertainties.

The first hypothesis hypothesizes that the CubeSat setup, including three torque rods, a three-axis magnetometer, three-axis gyroscope and two-axis Sun sensor, could be controlled via an active control strategy. This should happen while the known perturbations and unknown uncertainties are modelled. The second hypothesis claims that attitude control can be improved with a proper estimator such as Extended Kalman Filter (EKF). The second hypothesis relies on the results from the first hypothesis.

The specific hypotheses to be studied for this research program are as follows:

- **Hypothesis 1: Magnetic Attitude Control**

  The Iris Satellite can be controlled adequately with a spin-stabilized control strategy using three orthogonal magnetorquers, a three-axis magnetometer, a three-axis gyroscope, and a two-axis Sun sensor.

- **Hypothesis 2: Attitude Estimation using Kalman Filtering**

  An extended Kalman filter can ensure appropriate control accuracy even during an eclipse.

Further achievements were made in order to fulfill the hypotheses. A list of the main contributions is given below.

- **Contribution 1: Attitude Control Simulation**

  I established a robust spin-stabilized control strategy based on a PD algorithm for the Iris CubeSat with a $4\ deg$ pointing accuracy.

- **Contribution 2: EKF algorithm with dimension reduction technique**

  I established an extended Kalman filter that uses a dimension reduction technique for the sun sensor measurement to estimate the sun position vector throughout the trajectory (sunlit and eclipse) which improved the pointing error to $0.18\ deg$.

The following section summarizes some notable research and traces the development in the field. All CubeSats considered in the literature review have three torque rods and at least one magnetometer, gyroscope, and sun sensor.

1.3 Literature Review on Hypothesis 1: Magnetic Attitude Control

Since the beginning of the space era, satellites have carried magnetic actuation to stabilize the spacecraft. In the first decades of space exploration, passive magnetic systems such as permanent magnets, hysteresis rods and magnetic dampers were popular [23]. They did not require any

onboard computational effort and consumed little power. As one of the oldest studies in this field, in 1961, Fischell presented a passive magnetic control design that was introduced to dampen the undesired motion of the spacecraft [24].

However, after 60 years, passive magnetic stabilization is still being used in many nanosatellites where an agile controller is not needed, the pointing accuracy requirements are low, and the computational effort and power are limited. Good examples of passive magnetic stabilization are KySat-1 and KySat-2, the University of Kentucky CubeSats, launched in 2011 and 2013, respectively [25].

Active magnetic actuation such as magnetorquers was mainly used for body rate damping in detumbling mode until the 90s. It was not widespread in the fine pointing phase until researchers proved the functionality of using only three torque rods without passive actuation [22][26]. Since then, much research has been carried out regarding the attitude control problem with only active magnetic actuation for an underactuated spacecraft [27][28].

Psiaki has proposed active magnetic torque to stabilize the roll axis and provide damping in pitch and yaw for a nadir-pointing LEO spacecraft. The simulations showed the worst-case scenarios of $25\ (deg)$ attitude error at altitudes below 450 (km) [29].

In order to study the functionality of magnetic actuated control, Sofyali et al. [30] studied two cases. The first case tested the efficacy of pure magnetic actuators, and the second situation tested the layout of three magnetorquers and one momentum wheel along the pitch axis. They have clearly shown the results of magnetic control moments in which the second scenario(momentum-based algorithm) consumes approximately ten times more energy than the purely magnetic algorithm.

In 2018, Carletta et al. [31] developed a detumbling algorithm with different sampling rates, unknown deployment rates and unknown inclination, stabilizing the CubeSat within two orbits. Similarly, in terms of testing magnetic underactuated systems, a team of students at the University of Granada presented an ADCS conceptual design for an educational 1U CubeSat. The CubeSat was a magnetorquer-only satellite with software implemented in both Matlab and C++ [32].

Many researchers have proposed different control algorithms to better compromise the underactuated system issue. In 2015, Walker et al. [33] compared a fuzzy-based controller with a Linear Quadratic Regulator (LQR) for a magnetically actuated CubeSat and successfully proved the effectiveness of the fuzzy inference engines with faster convergence. In [34] a robust backstepping control technique was introduced to handle fast-rotating magnetorquer-only satellites. In this research, the feedback control was enhanced with averaging techniques and the errors in the inertia matrix estimation.

In order to research a new algorithm, Cruz et al. introduced a retrospective cost adaptive control(RCAC) method to address the rank deficiency. The nonlinear, continuous spacecraft dynamics were linearized to obtain Markov parameters. For high inclination orbits, the authors developed an inertia-free stabilizing control law using the averaged Markov parameter [35].

A spin stabilization controller for the Japan Canada Joint Collaboration Satellite – Formation Flying (JC2Sat-FF) was designed to stabilize an asymmetric spacecraft. The results successfully show stabilization even under the failure of up to two magnetic torque rods and magnetic torque rod saturation if the remaining magnetic torque rod was not aligned with the spin axis. The experiment has been proven in test only on Earth testbeds [36].

In [37], the authors propose a spin-stabilization strategy for sequentially maneuvers which take place at the apogee point. In this maneuver, the magnetic attitude control of spacecraft has to align the spin axis direction with the direction of its velocity.

In a similar spin stabilization scenario, Bolandi et al. [38] considered an only magnetic actuated satellite with a supervisory-adaptive controller. The authors' design choice is to lower the attitude error and power consumption and, on the other hand, improve the speed of response while proving the stability of the spinning satellite.

Torczynski et al. [39] presented a magnetically actuated educational CubeSat(Delfi-n3Xt) with an accuracy of five degrees on each axis. Actuator constraints and other perturbations such as solar radiation, residual dipoles, and gravity gradient torques were considered.

In summary, the recent literature has considered different methods such as conventional

controllers and adaptive controllers. However, compared to this thesis, the literature has not demonstrated a fully integrated simulation with a propagator, two independent controllers, and a conventional estimator in an only-magnetic actuated system with a precise attitude pointing to $0.18\ deg$ considering all known perturbation and unknown dynamics. In this research, the spin stabilization maneuver is done with only magnetorquers. However, in the literature, the authors mostly use other actuators such as thrusters and reaction wheels to help spin up the spacecraft.

1.4 Literature Review on Hypothesis 2: Attitude Estimation using Kalman Filtering

Since most satellites use sun sensors for attitude determination, they need to estimate their attitude during an eclipse when the sun sensor measurements are not available. Moreover, a partial sensor failure may happen, and an estimator may prevent an early mission failure. For example, in 2008, Mimasu et al. [40] introduced both linear and extended Kalman filter for attitude determination of a CubeSat. They successfully used magnetometers and the gyro rate sensor feedback to estimate and maintain the attitude during the eclipse.

Ni et al. [41] presented an attitude control system using three sets of sun sensors, magnetometers and gyroscopes. Additionally, an extended Kalman filter was used to filter the sensor noises. The integrated simulation proved to have promising results of meeting $0.05\ Deg$ pointing accuracy by fusing three sensors of gyroscope, magnetometer and sun sensor measurement output.

Abdelrahman et al. [42] have presented an eleven-dimensional extended Kalman filter using only magnetometer measurements. The states include angular velocity, quaternion parameters, residual dipole and the drag coefficient. The authors proved the functionality of the estimator via Monte-Carlo simulations.

In 2017 Hajiyev et al. [43] proposed a nontraditional EKF method integrated with singular value decomposition(SVD). The estimation algorithm has only good performance in the eclipse

short time intervals. The authors finally concluded that neither traditional nor nontraditional attitude estimation approaches could give attitude knowledge in an acceptable range and therefore recommended to use of other methods for the eclipse period. In the same year, Messman et al. [44] designed the ADC subsystem for the first CubeSat of the Technical University of Munich (TUM) using six magnetorquers on each side panel. They considered an EKF algorithm to estimate the attitude and the gyroscope bias.

Sugimura et al. [45] suggested an extended Kalman filter using a magnetometer's measurements for the eclipse period of a satellite. They further have introduced a robust singularity method based on the PD algorithm for attitude control of a nadir-pointing CubeSat.

In 2018 Ivanov et al. [46] considered a CubeSat with an active controller actuated with three torque rods. They designed an extended Kalman filter considering the states as body rates and quaternion parameters. They demonstrated an attitude estimation with 2 degrees accuracy error in the nominal orbit. In another work, they considered an EKF to track the magnetometer bias to help in attitude determination accuracy [47].

In 2020 Chirame et al. [48] discussed the ADC subsystem of an educational CubeSat of IIT university. The authors used the Quest algorithm and Multiplicative EKF to estimate the attitude vector and angular rate bias. Similarly, a deorbiting space probe is studied in [49] for tethering space debris. The probe was equipped with three magnetorquers, gyroscopes and magnetometers, a sunsensor, and a Global Navigation Satellite System(GNSS). A multiplicative Extended Kalman Filter was designed to estimate the pointing of the space probe.

Compared to this thesis, no research has considered a 5-dimensional conventional extended Kalman filter. Most researchers tried to develop a new algorithm and increase its accuracy by increasing the order of the state space, eventually increasing the computational effort, which may not be capable of being implemented onboard. In this research, the state space uses the measurement output from the 2-axis sun sensors to estimate the satellite's attitude. The proposed method is different from most research that uses a three-dimensional sun position vector, eventually increasing the computational effort and model complexity.

1.5 Outline of Thesis

This thesis analyzes the attitude determination and control subsystem(ADCS) using Matlab/Simulink simulation. Effort has been put into keeping the Simulink model reusable, and it can easily be extended for future satellites. The mathematical model of the actuators and sensors used for this satellite is based on hardware specifications. This simulation helps the reader understand the mission and how the satellite design is able to meet requirements.

The Iris CubeSat is modelled as an example in Simulink. Further, an extended Kalman filter algorithm is written in MATLAB and embedded in Simulink for attitude estimation based on three-axis gyroscope and two-axis sun sensor measurements. Simulations characterize the attitude dynamics of the satellite, and a classic strategy is suggested to estimate the sun vector position onboard with a state reduction technique. Subsequently, the detumbling and sun pointing spin-stabilized algorithm are tested with simulated perturbation sources and unknown dynamic uncertainties, which robustly identifies and cancels out the satellite's external perturbations and residual dipole to satisfy mission requirements. For a fully guaranteed performance, the estimator is tested with all perturbation and unknown dynamic uncertainties.

The motivation for this thesis, literature review, hypotheses and contributions are introduced in this chapter. The second chapter reviews the dynamics of an underactuated satellite and introduces Iris's mission, coordinate frames, and perturbation torques. The third chapter elaborates on the simulation design, including the orbit propagator, environmental blocks and controller design. The fourth chapter describes the EKF principles and the dimension reduction strategy of the EKF. Chapter five presents the power management strategy followed by the simulation results and discusses the plots before a research conclusion is given at the end of this thesis.

Chapter 2

Spacecraft Dynamics

This section presents the background required for the proceeding chapters. First, an explanation of the Iris CubeSat mission will be given. Further, the orientation of reference frames used in this research will be illustrated. The chapter follows with the attitude dynamics equations of a rigid body satellite. Finally, the quaternion-based rotation matrix will be presented.

2.1 Iris Mission Description

Iris, previously known as the Manitoba satellite, is a 3U underactuated CubeSat scheduled to be launched in 2022 [50]. Iris has a space weathering mission that is at the final stages of development at the University of Manitoba in the Space Technologies and Advanced Research Laboratory (STARLab). Within this mission, the Iris team will study the modification of materials while in space and being exposed to sunlight and other radiation effects [51]. The materials include 24 geological samples, which are accounted as the main payload in the Iris mission. The mission requires the ADCS to hold sun pointing attitude with $\pm 21\ (deg)$ pointing error and recover from the ensuing tumble after being ejected from the launcher. As seen in Fig. 2.1 sun pointing ensures enough power from the solar arrays for the satellite while maintaining the orientation of the payload.

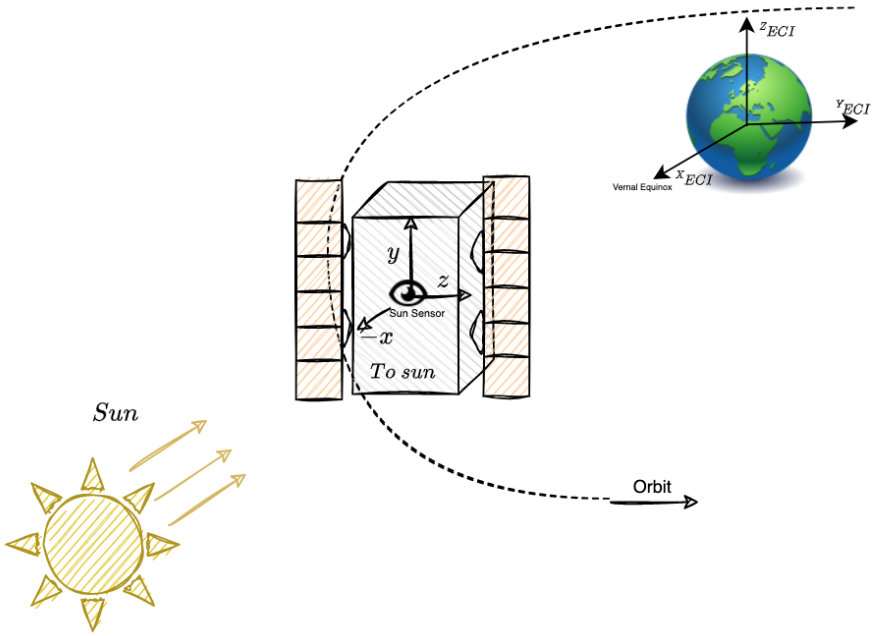


Figure 2.1: Illustration of the Iris 3U CubeSat with a sun sensor and sun-facing solar panels

Given the Iris orbit, an approximately circular orbit with a 54-degree inclination, roughly 40 percent of each orbit is spent in the eclipse. The schematic of this orbit is shown in Fig. 2.2. The orbital parameters will be presented in Section 3.1 while elaborating the orbit simulation.

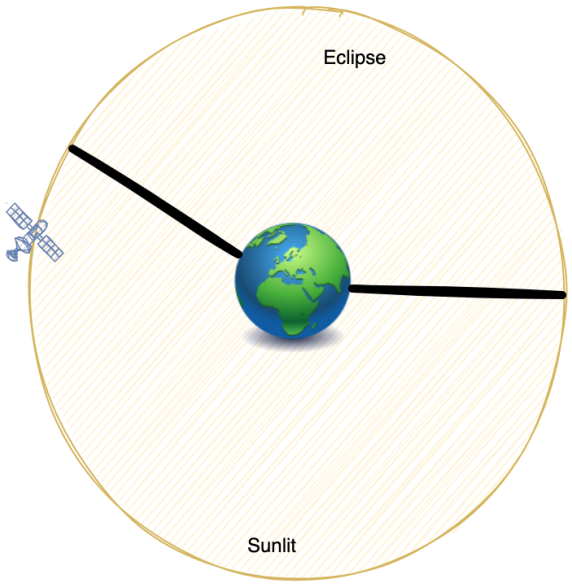


Figure 2.2: Iris Orbit visualization in terms of sun lit and eclipse phase

2.2 Coordinate Reference frames

The reference frame is a three-dimensional system that provides information about the position of a specific object. To define the orientation of the satellite, a reference frame must be defined. In this research, for the ADC subsystem of a sun-pointing spacecraft in a circular orbit, the earth-centred inertial(ECI) and body frame are adopted, which are described in the following. The satellite's attitude is the rotation between the body-fixed frame and ECI, which is the focus of this study. That is why defining the coordinate frames before the motion dynamics is essential.

2.2.1 Earth Centered Inertial (ECI) frame

The frame's origin is at the center of Earth, but it does not rotate with the Earth. As seen from Fig. 2.3, the coordinates' axes are as the following:

- x-axis points to the vernal equinox direction
- z-axis points upwards to the north pole
- y-axis completes the right-hand system

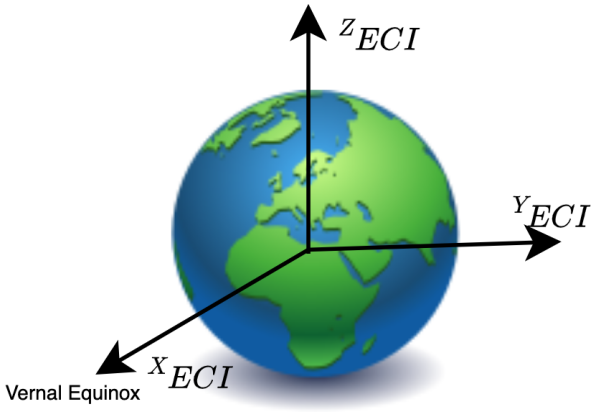


Figure 2.3: ECI frame

2.2.2 Satellite Body frame

The body frame axes correspond to the principal inertial axes of the satellite and rotate with the satellite. The origin of the body frame is the satellite's center of mass. As seen from Fig. 2.1, the coordinates are the following:

- $-x$-axis normal to the satellite sample plate
- y-axis points upwards opposite the geology samples
- z-axis completes the right-hand system

2.2.3 Orbital frame

The origin of the orbital frame is the satellite's center of mass. As seen in Fig. 2.4, the coordinates are as the following:

- x-axis is in the direction of the velocity of the satellite
- z-axis points towards the centre of mass of the earth
- y-axis completes the right-hand system

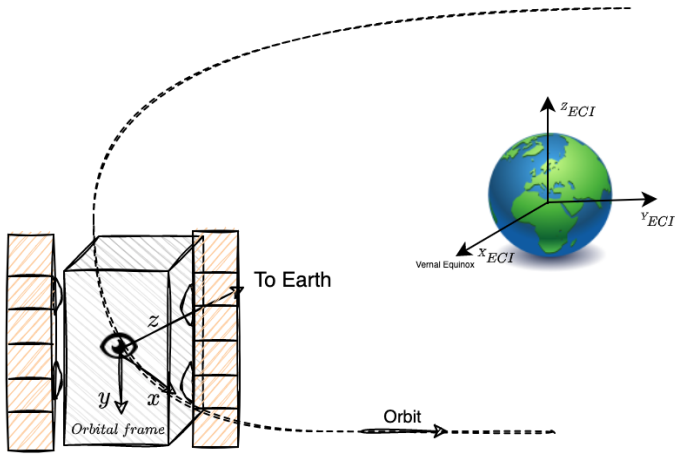


Figure 2.4: Orbital frame

2.3 Attitude Dynamics of a rigid body

A rigid body is the simplest model that can be used for spacecraft attitude dynamics. As opposed to the point mass, a rigid body occupies a finite volume and is known for the fixed distance between any two elements [19].
In the matrix form, let's examine the Euler's equation as:

$$\vec{T} = I\dot{\vec{\omega}} + \vec{\omega} \times (I\vec{\omega}) \tag{2.1}$$

where ω is the satellite's angular velocity expressed in the body frame. I is the moment of inertia, and $\vec{T}$ is the total external torque in the body frame. Also, the moment of inertia is always calculated from the center of mass.

The principal axis assumption shown in equation 2.2 makes it possible to create expressions for the angular accelerations that are not functions of other angular accelerations. Added to that, this will make it possible to perform independent axis control and analysis. If the moment of inertia tensor is not diagonal, it can be diagonalized by finding eigenvalues and eigenvectors.

$$I = \begin{bmatrix} I_1 & 0 & 0 \\ 0 & I_2 & 0 \\ 0 & 0 & I_3 \end{bmatrix} \tag{2.2}$$

If $\mathscr{F}_b$ is the principal-axis frame as seen in equation 2.2, the product moments vanishes, resulting in the below set of equations.

$$\begin{aligned} T_1 &= I_1\dot{\omega}_1 + (I_3 - I_2)\,\omega_2\omega_3 \\ T_2 &= I_2\dot{\omega}_2 + (I_1 - I_3)\,\omega_3\omega_1 \\ T_3 &= I_3\dot{\omega}_3 + (I_2 - I_1)\,\omega_1\omega_2 \end{aligned} \tag{2.3}$$

Now if all components of moment of Inertia (MOI) tensor are known, I is always symmetric

$\left(I = I^T\right)$ and positive definite. In this case, since the body is considered as rigid, the MOI tensor is also constant.

2.4 Quaternion-derived Rotation Matrix

Although quaternions are not used in the estimator and the control algorithm, they can define the rotation matrix well alongside Euler's theorem. Euler's theorem declares that the satellite's motion with one point fixed can be defined as a single rotation about an axis through that fixed point[52][19][53]. By defining the eigenvalue and eigenvector of rotation matrix C, the axis and the corresponding angular rotation could be determined. The symbol a is the Euler's axis of rotation and the ϕ is the Euler's angle of rotation. Consequently, the following matrix of rotation could be derived [19] as seen in equation 2.4.

$$\mathrm{C} = \cos\phi 1 + (1 - \cos\phi)\mathbf{a}\mathbf{a}^T - \sin\phi\mathbf{a}^\times \tag{2.4}$$

The quaternion parameters present the standard angular displacement parameterization for spacecraft attitude as:

$$\eta = \cos\frac{\phi}{2}, \quad \boldsymbol{\epsilon} = \mathbf{a}\sin\frac{\phi}{2} = \begin{bmatrix} a_1\sin(\phi/2) \\ a_2\sin(\phi/2) \\ a_3\sin(\phi/2) \end{bmatrix} \tag{2.5}$$

η and ϵ often stack together into a 4×1 column vector known as quaternion:

$$\boldsymbol{q} = \begin{bmatrix} \eta \\ \boldsymbol{\epsilon} \end{bmatrix} \tag{2.6}$$

Finally, expressing the rotation matrix from ECI to the body in terms of quaternions and plugging in the equation 2.4, the C_{body}^{ECI} is obtained [19]:

$$C_{body}^{ECI} = (\eta^2 - \epsilon^T\epsilon)1 + 2\epsilon\epsilon^T - 2\eta\epsilon^\times = \begin{bmatrix} 1-2(\epsilon_2^2+\epsilon_3^2) & 2(\epsilon_1\epsilon_2+\epsilon_3\eta) & 2(\epsilon_1\epsilon_3-\epsilon_2\eta) \\ 2(\epsilon_2\epsilon_1-\epsilon_3\eta) & 1-2(\epsilon_3^2+\epsilon_1^2) & 2(\epsilon_2\epsilon_3+\epsilon_1\eta) \\ 2(\epsilon_3\epsilon_1+\epsilon_2\eta) & 2(\epsilon_3\epsilon_2-\epsilon_1\eta) & 1-2(\epsilon_1^2+\epsilon_2^2) \end{bmatrix} \tag{2.7}$$

Furthermore, if equation 2.5 is differentiated it would lead to the following attitude kinematics model [53]:

$$\dot{\mathbf{q}} = \frac{1}{2}\mathbf{W}(\omega)\mathbf{q}, \tag{2.8}$$

where $\mathbf{q} \in \mathbb{R}^4$ on the right hand side is the unit norm vector of quaternions and

$$\mathbf{W}(\omega) = \begin{bmatrix} 0 & \omega_z & -\omega_y & \omega_x \\ -\omega_z & 0 & \omega_x & \omega_y \\ \omega_y & -\omega_x & 0 & \omega_z \\ -\omega_x & -\omega_y & -\omega_z & 0 \end{bmatrix} \tag{2.9}$$

Chapter 3

ADCS Simulation design

This chapter presents a detailed analysis of the simulation done in MATLAB/Simulink. It describes the ADCS software algorithm, the reasons for design choices, and how the ADCS integrates with the rest of the spacecraft, specifically power subsystem. The section closes with a summary.

Initially, the whole simulation block diagram is brought into view. Then the simulation is divided into nine blocks, as seen in the following.

- The Simplified General Perturbations (SGP4) Orbit Propagator
- Earth's magnetic field
- Environmental Block including gravity gradient torque and residual magnetic disturbances
- Kinematics and Dynamics
- Solar Ephemeris
- Attitude Determination including EKF block
- Controller block including detumbling and spin stabilization controller
- Magnetorquers power consumption
- Power Analysis Block

In Fig. 3.1 a simplified block diagram of the ADCS simulation is shown:

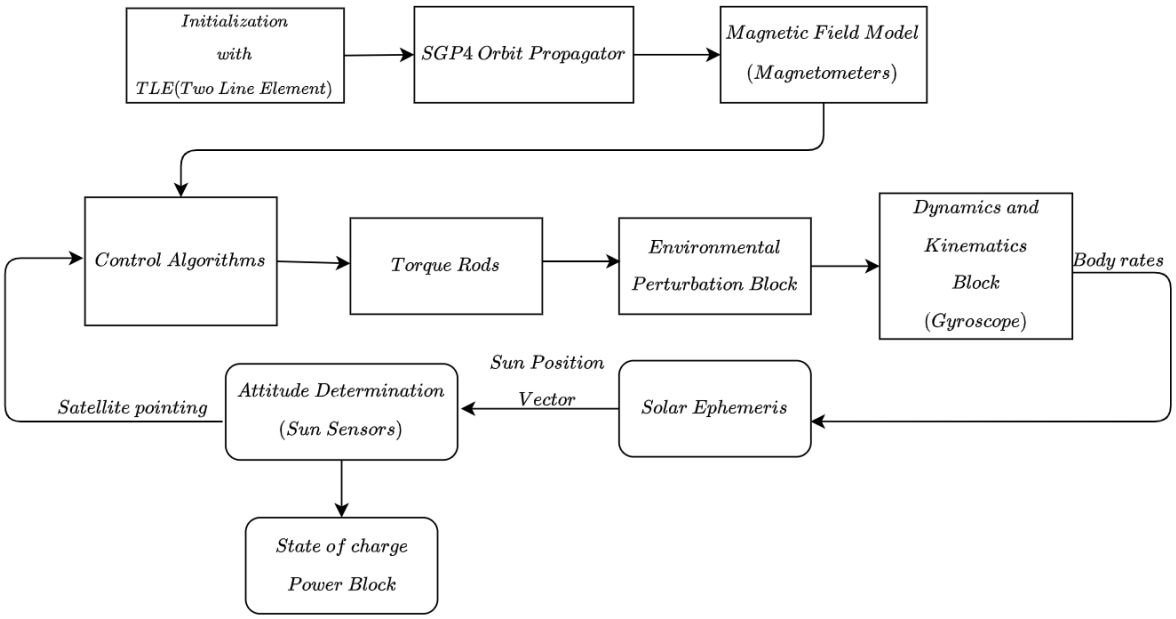


Figure 3.1: Simplified block diagram of ADCS simulation

The goal was to create sensor simulations that would accurately mimic actual hardware. In the dynamics and kinematics block, as shown in Fig. 3.1, the gyroscope takes the angular velocity from the Euler equations. The magnetometer takes the B-field in the body frame and adds realistic noise to simulate the actual magnetometer hardware characteristics. In the solar ephemeris and attitude determination block, the coordinate of the Sun vector will be simulated by finding the Sun's coordinate in the inertial frame and then change it into the body frame. Furthermore, in the eclipse the the EKF block is used to estimate the satellite's attitude.

In the following the simulation blocks will be presented in the best order possible to describe all inputs and outputs.

3.1 SGP4 Orbit Propagator

Designing an orbit propagator and calculating the spacecraft's position and velocity in orbit is the first step of any space mission simulation. The SGP4 orbit propagator blockset shown in Fig. 3.2 is implemented based on the Keplerian orbit calculations and takes J2 perturbations into account,

i.e. second degree zonal harmonics or Earth oblateness. The source of the J2 perturbation is Earth's oblateness, as the Earth is not a perfect sphere, and its mass is not uniformly distributed.

Additionally, NORAD's Two Line Elements are employed as the initialization data for the propagator, as seen in Table 3.1. The TLE is not updated in the simulation, and this feature is not considered since there is no knowledge of updated TLEs.

The orbital elements used in the simulation are derived from the TLE which corresponds to International Space Station(ISS). The SGP4 orbit propagator calculates the spacecraft's position and velocity provided by the orbital elements listed below. For this purpose, the SGP4 orbit propagator is implemented in the toolbox.

Element	Symbol	Value
Epoch	epoch	20035 (JD)
Inclination	i	52.99 (deg)
Right Ascension of the Ascending Node	RAAN	262.1814 (deg)
Eccentricity	e	1.36e-4
Argument of Perigee	ω	51.2982 (deg)
Mean Anomaly at Epoch	M	110.10 (deg)
Mean Motion	n	15.4 (rev/day)
Semi Major axis	a	6824 (m)
Orbit Period	T	5610 (s)
Day of year	D	34.58

Table 3.1: TLE Orbital Elements

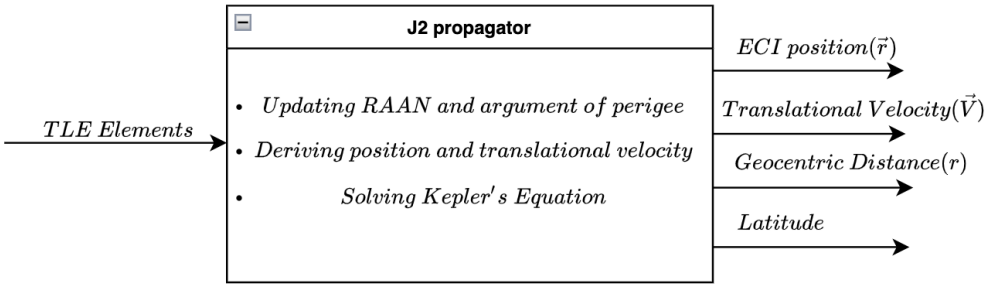


Figure 3.2: Simplified block diagram of SGP4 propagator algorithm

The J2 perturbation affects all the orbital elements except the semi-major axis, eccentricity

and inclination (equation 3.1). The variations in the RAAN and the argument of perigee are most sensitive to the J2 perturbation. These two variations are known as the regression of line of nodes (variation of RAAN) and precession of the line of apsides (variation of the argument of perigee) which are given below in equations 3.2 and 3.3:

$$\dot{a} = 0, \dot{e} = 0, \quad \dot{i} = 0 \tag{3.1}$$

$$\dot{\Omega} = \frac{-3J_2R^2 \cos i}{2(1-e^2)^2}\sqrt{\frac{\mu}{a^7}} \tag{3.2}$$

$$\dot{\omega} = \frac{3J_2R^2(5(\cos i)^2 - 1)}{4(1-e^2)^2}\sqrt{\frac{\mu}{a^7}} \tag{3.3}$$

where J2 is equal to 0.0010836 and μ is the gravitational parameter that is equal to $3.987e14\ \frac{m^3}{s^2}$. In order to determine the semi-major axis (a), since the eccentricity is near zero and the orbit is circular, from the Earth center it can be written as:

$$a = (\frac{\mu}{(\frac{2\pi n}{24\times 3600})^2})^{\frac{1}{3}} \tag{3.4}$$

where n is the mean motion mentioned in Table. 3.1.

Equation 3.5 calculates the periapsis time, which is a requirement for the true anomaly.

$$t_0 = \frac{M_0 T}{2\pi} \tag{3.5}$$

where M_0 is the mean anomaly in radians extracted from the TLE and T is the orbit period.

Then the updated mean anomaly can be calculated as in equation 3.6.

$$M = 2\pi\frac{t - t_0}{T} \tag{3.6}$$

The next step is solving the Kepler equation with an iterative loop which is expressed as

equation 3.7.

$$E = M + e \sin E \tag{3.7}$$

where E is the eccentric anomaly and e is the eccentricity. The updated true anomaly (θ) will take E into account and will be calculated by:

$$\tan\left(\frac{\theta}{2}\right) = \sqrt{\frac{1+e}{1-e}} \tan\left(\frac{E}{2}\right) \tag{3.8}$$

which will lead to:

$$\theta = 2tan^{-1}(\sqrt{\frac{1+e}{1-e}} \tan\left(\frac{E}{2}\right)) \tag{3.9}$$

The inertial position $\vec{r}$ and velocity $\vec{v}$ can be determined from the following equations.

$$\vec{r} = (r\cos\theta)\hat{o}_1 + (r\sin\theta)\hat{o}_2 \tag{3.10}$$

$$\vec{v} = \sqrt{\frac{\mu}{p}}\,[-(\sin\theta)\hat{o}_1 + (\cos\theta + e)\hat{o}_2] \tag{3.11}$$

where $\hat{o}_1$ and $\hat{o}_2$ correspond to the axis of orbital frame in the form of $\hat{o}_1 = [1; 0; 0]$ and $\hat{o}_2 = [0; 1; 0]$. The geocentric distance denoted by r is the norm value of $\vec{r}$.

Further, the latitude (λ) simply could be derived by equation 3.12 which will be used in Earth magnetic field block to calculate the magnetic field.

$$\lambda = sin^{-1}\frac{\vec{r}_z}{r} \tag{3.12}$$

3.2 Earth Magnetic Field Block

The Earth's magnetic field as seen in 3.3 is caused by the Earth's solid iron core surrounded by high-temperature liquid metal.

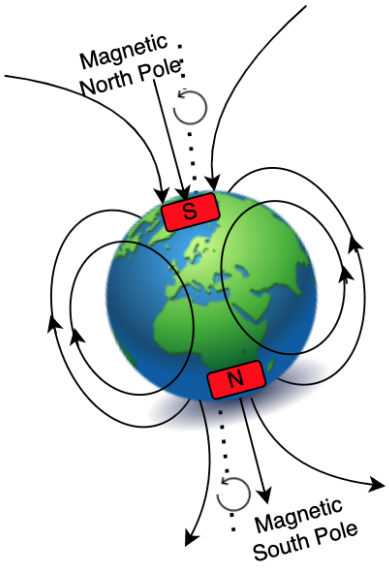


Figure 3.3: Schematic of Earth magnetic field

Figure 3.4 represents the Simulink block of the Earth magnetic field which inputs the inertial position ($\vec{r}$) and outputs the magnetic field in ECI frame.

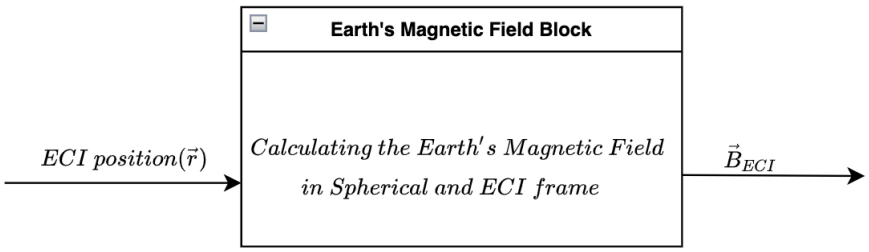


Figure 3.4: Simplified block diagram of Earth's magnetic field algorithm

The magnetic field of the planet Earth can be represented by a magnetic potential:

$$\phi_m = -\frac{\mu_m}{r^2} sin\lambda \tag{3.13}$$

Where r is the satellite's distance to the center of Earth (geocentric distance), λ is the latitude from the geomagnetic equatorial plane, and μ_m is the dipole strength of the Earth ($7.96 \times 10^{15}\ T.m^3$). As seen in Fig. 3.3 the magnetic North Pole is not aligned with the geographic North Pole, but in this research, the two are considered to be the same. So then, the geomagnetic equatorial plane is the same as a geographic equatorial plane. Similarly, geomagnetic latitude is the same as geocentric latitude because the axes are the same.
Then, the magnetic field could be written as a potential function:

$$\vec{B}_{ECI} = -\vec{\nabla}\phi_m \tag{3.14}$$

Geocentric spherical coordinates, as seen in Fig. 3.5 are comprised of the geocentric radial vector ($\vec{r}$), the east longitude or azimuth angle (α) and the latitude angle (λ).

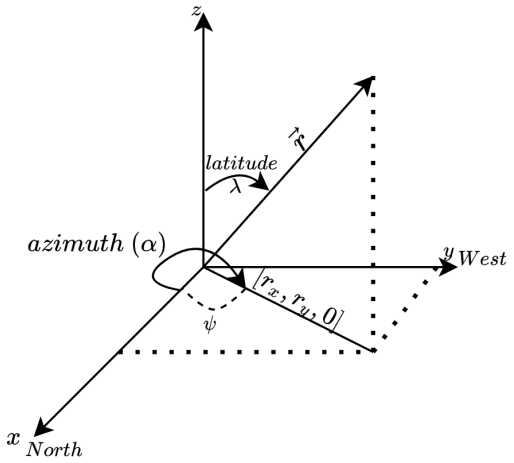


Figure 3.5: Azimuth angle is measured in degrees clockwise from x axis or the North

In spherical coordinates, $(\vec{r}, \alpha, \lambda)$, the gradient takes the form:

$$\nabla f(\vec{r}, \alpha, \lambda) = \frac{\partial f}{\partial r}\hat{r} + \frac{1}{rsin\lambda}\frac{\partial f}{\partial \alpha}\hat{\alpha} + \frac{1}{r}\frac{\partial f}{\partial \lambda}\hat{\lambda} \tag{3.15}$$

The potential is not a function of the azimuth angle, so the second term is equal to zero.

$$B_r = \frac{\partial \phi_m}{\partial r} = \frac{2}{r^3}\mu_m \sin\lambda \tag{3.16}$$

$$B_\alpha = 0 \tag{3.17}$$

$$B_\lambda = \frac{1}{r}\frac{\partial \phi_m}{\partial \lambda} = \frac{\mu_m}{r^3}\cos\lambda \tag{3.18}$$

where B_r and B_λ represent the field strength in spherical coordinates, and the other variables defined as before.

From equations 3.16, 3.17 and 3.18 one can obtain:

$$\vec{B}_{spherical} = \begin{bmatrix} B_r \\ 0 \\ B_\lambda \end{bmatrix} \tag{3.19}$$

In order to compute the azimuth angle, regarding Fig. 3.5, the dot product of the x axis and the projection of the satellite's position vector ($\vec{r}$) will help.

Therefore, let's examine $\hat{x} = [1, 0, 0]$ so:

$$p = \hat{x}. \begin{bmatrix} r_x \\ r_y \\ 0 \end{bmatrix} \tag{3.20}$$

Then the azimuth angle can be derived from the definition of the dot product. However, it's easier to find the ψ angle as shown in Fig. 3.5. The azimuth angle would be equal to $2\pi - \psi$ or $-\psi$:

$$\psi = cos^{-1}(\frac{p}{\sqrt{{r_x}^2 + {r_y}^2}}) \tag{3.21}$$

Finally, to perform the rotation from the spherical frame to the ECI frame, two successive rotations about latitude (λ) and azimuth ($-\psi$) angles are defined. First, it is a 2-axis rotation about λ angle:

$$C_1 = \begin{bmatrix} \cos(\lambda) & 0 & -\sin(\lambda) \\ 0 & 1 & 0 \\ \sin(\lambda) & 0 & \cos(\lambda) \end{bmatrix} \tag{3.22}$$

And then it is a 3-axis rotation about $-\psi$ angle:

$$C_2 = \begin{bmatrix} \cos(\psi) & -\sin(\psi) & 0 \\ \sin(\psi) & \cos(\psi) & 0 \\ 0 & 0 & 1 \end{bmatrix} \tag{3.23}$$

This yields the necessary rotation matrix from the spherical to the ECI frame.

$$C_{spherical}^{ECI} = C_1 C_2$$

Finally, in order to find the magnetic field in the ECI frame, it becomes:

$$\vec{B}_{ECI} = C_{spherical}^{ECI} \vec{B}_{spherical} \tag{3.24}$$

$\vec{B}_{ECI}$ represents the magnetic field in the ECI frame, which will later be rotated to the body frame to simulate the magnetometer measurements.

3.3 Environment Block

The environment block in the simulation includes the perturbation torques. The major disturbance torques for satellites are as the following:

1. Gravity-gradient torque

2. Residual Magnetic Dipole torque

3. Unknown disturbances and dynamic uncertainties

The dominant disturbances in LEO orbit at $400\ km$ altitude are gravity gradient and aerodynamic torques. Additionally, a Gaussian white noise can be considered to simulate the unknown perturbations and dynamic uncertainties. Any other known disturbance torque, such as aerodynamic torque due to drag and solar pressure, which are hard to simulate, is included in the white noise. The simulation block is shown in Fig. 3.6. According to equation 1.1 in this block the disturbance torque (T_d) is added to the magnetorquer torque (T_{mag}).

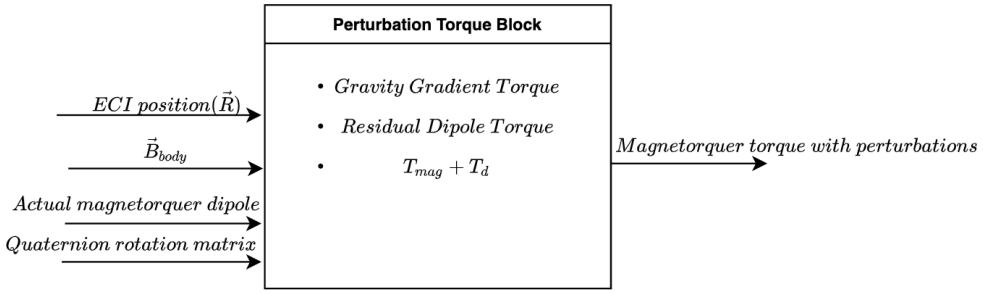


Figure 3.6: Simplified block diagram of disturbance torques

3.3.1 Gravity-Gradient Torque

Gravity gradient torque is one of the predominant perturbations over LEO orbits. This torque appears because different satellite parts will experience different gravitational pulls from the slight difference in distance from the Earth. A perturbation torque can be derived from Newton's law of gravitation by treating the satellite as a body with volume rather than a point mass, as seen in Fig. 3.7.

Equation 3.25 is the final expression for the gravity-gradient perturbation torque in a body-fixed frame [19]:

$$\vec{T}_{gravity\ gradient} = \frac{3\mu_e}{r^5}\vec{r}\times I\vec{r} \tag{3.25}$$

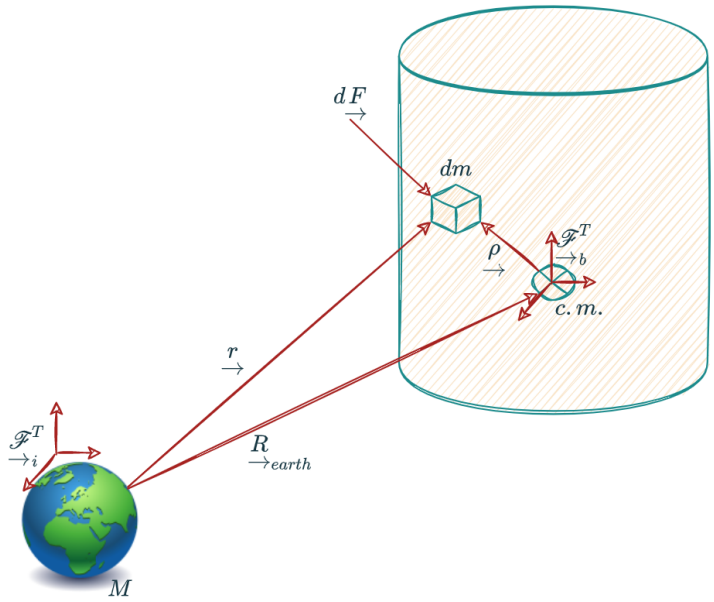


Figure 3.7: Gravitational Force exerted on the satellite regarding Newton's Law of Gravitation

where

$$\mu_e = GM_e = 3.986 \times 10^{14}\ \mathrm{m}^3/\mathrm{s}^2$$

μ_e is the gravitational constant of the large mass M (Earth) and $G = 6.672\times\ 10^{-11}\ \mathrm{m}^3/\mathrm{kg}\cdot\mathrm{s}^2$ is the universal gravitation constant. $\vec{r}$ is the position vector of the satellite in the body frame. r is the satellite geocentric distance or the magnitude of the satellite position vector from the Earth. Given that the vectors are expressed in a body-fixed frame, I is the satellite moment of inertia in the body frame, which is constant when considering the satellite as a rigid body.

3.3.2 Residual Magnetic Torque

Due to the CubeSat's small moment of inertia, residual magnetic torque is one of the significant disturbances for CubeSats in LEO. The interaction of the magnetic field of Earth and Iris actuators generates a dipole field called the magnetic dipole moment. This interaction is desired, and magnetorquers use this effect for attitude control with regulated current output. However, power harnessing can induce an undesired magnetic disturbance that acts in the same direction or at odds with the magnetorquers. This undesired torque shall be accounted for in the design.

There are three strategies for reducing the residual magnetic moment. First, the CubeSat's hardware harnessing should minimize the residual dipole moment. For instance, the harnessing could be coated with aluminum foils to prevent the magnetic field from adversely affecting the spacecraft. Additionally, the structure of the power harness shall be designed to avoid the formation of wiring loops that contribute to the components of magnetic moment noted by $\vec{m}$.

As the second strategy, the total residual dipole moment can be further reduced by forming loops with the reversed flow direction in the CubeSat and solar panels. The undesired magnetic torques cancel each other out.

The third strategy is to build the satellite from magnetically clean material. In some cases, the magnetic cleanliness of the CubeSat would cause the manufacturing costs to rise, which would eventually surpass the CubeSat monetary budget. Hence, the passive or active controller should compensate for the residual dipole moment.
The residual dipole moment from the abovementioned sources produces a disturbance torque on the spacecraft according to:

$$\vec{T}_{residual\ dipole} = \vec{m}_{residual\ dipole} \times \vec{B} \tag{3.26}$$

The residual magnetic dipole of the spacecraft is challenging to quantify and is often not considered one of the disturbances in the research studies. However, regarding Iris's small size and weight and the usage of solar panels, the residual dipole is assumed to be a significant source of perturbations after the gravity gradient torque. In the simulation done in this thesis, I estimated the order and magnitude of the residual dipole moment.

Often the CubeSats should be able to cancel $0.001\ Am^2$ residual dipole on each axis. Since the solar panels are on the $y-z$ plane (Fig. 2.1), the residual dipole may appear on the y or z axis. On the other hand, if both solar arrays are illuminated, the residual dipole due to power harnessing would be cancelled. However, if just one of the panels is illuminated, the disturbance torque would just appear on the z axis. Therefore, the magnetorquers compensate for the residual

magnetic moment of the satellite to within $0.001\ Am^2$ on the z-axis. To sum up, the residual dipole is asymmetric in the Iris mission and written out in scalar detail:

$$\vec{m}_{residual\ dipole} = [0; 0; 0.001] \tag{3.27}$$

3.4 Kinematics and Dynamics

The goal of the dynamics block, is to find the angular velocity as shown in Fig. 3.8 which reconsiders Euler's equation from equation 2.1.

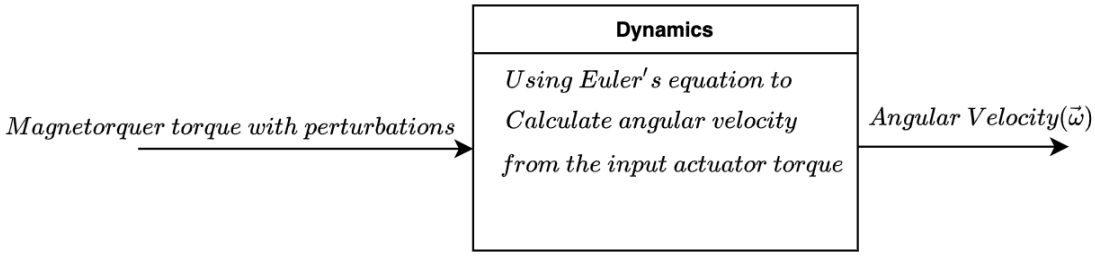


Figure 3.8: Simplified block diagram of Dynamics algorithm

The quaternion block in Fig. 3.9 computes the quaternion parameters of ϵ and η to feed the quaternion rotation block in equation 2.7. Written out in scalar detail:

$$\dot{\epsilon} = \frac{1}{2}(\eta 1 + \epsilon^{\times})\omega_{21} \tag{3.28}$$

$$\dot{\eta} = -\frac{1}{2}\epsilon^{T}\omega_{21} \tag{3.29}$$

Then the ϵ and η can be derived by integrating the equations 3.28 and 3.29.

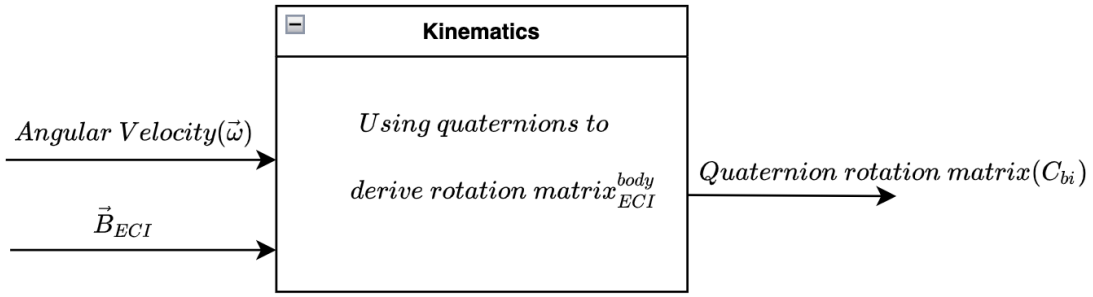


Figure 3.9: Simplified block diagram of Kinematics algorithm

Finally, according to Fig. 3.10 the rotation matrix (C_{bi}) is used to find the magnetic field in body frame (B_{body}). C_{bi} is the quaternion-derived rotation matrix which is elaborated in Section 2.4.

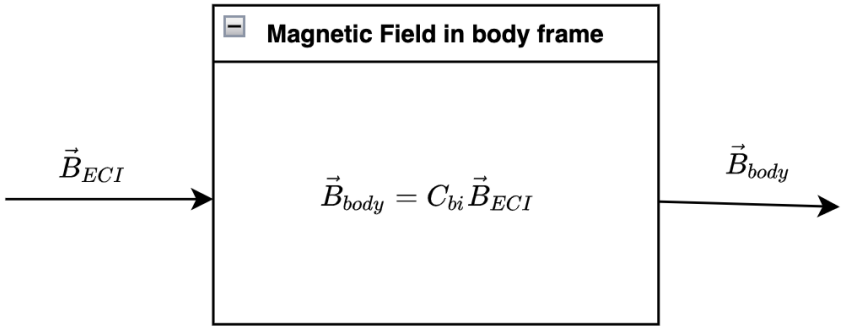


Figure 3.10: Simplified block diagram of B_{body} algorithm

3.5 Solar Ephemeris

The relative position of the satellite and Sun is simulated using the solar ephemeris block. The solar ephemeris block, as seen in Fig. 3.12 calculates the Sun's position vector according to the body frame.

The Sun's location can be approximated by noting that the Earth's spin axis is tilted at an angle of $23.5°$ about the Aries direction. The position where the vernal equinox meets the celestial equator plane is known as the First Point of Aries, as seen in Fig. 3.11.

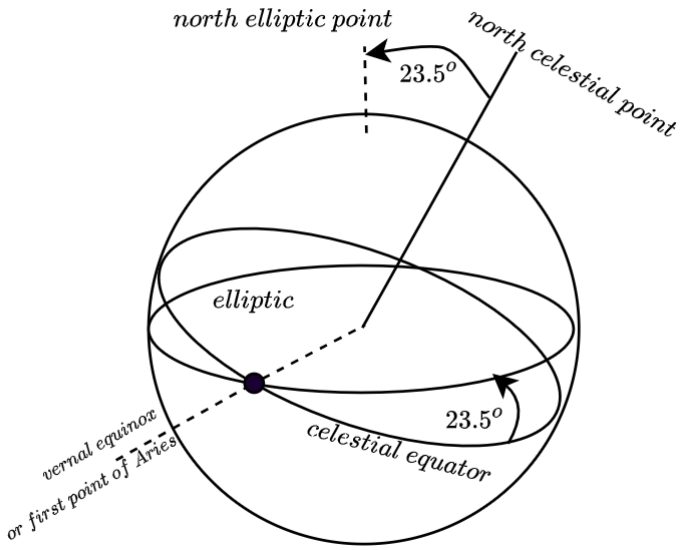


Figure 3.11: The tilt angle between ECI frame and Elliptic Frame

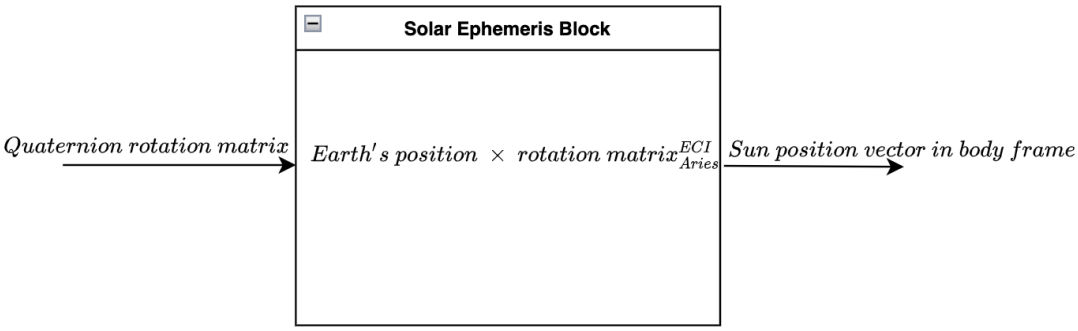


Figure 3.12: Simplified block diagram of solar ephemeris algorithm

Thus, one can write the orientation of the $\overrightarrow{\mathcal{F}}_i$ frame with respect to the $\overrightarrow{\mathcal{F}}_\epsilon$ frame as:

$$\overrightarrow{\mathcal{F}}_i = C_{i\epsilon}\overrightarrow{\mathcal{F}}_\epsilon \tag{3.30}$$

Where

$$C_{i\epsilon} = C_1\left(23.5^\circ\right) \tag{3.31}$$

Assuming a circular orbit of the Earth about the Sun, the Earth's position vector in the $\overrightarrow{\mathcal{F}}_\epsilon$ frame

is simply:

$$\hat{r}_\epsilon = \begin{bmatrix} \cos\theta_\epsilon \\ \sin\theta_\epsilon \\ 0 \end{bmatrix} \tag{3.32}$$

The periapsis ($\theta_\epsilon = 0$) is defined as the first day of autumn, which is September 21st. A good approximation for the true anomaly is:

$$\theta_\epsilon = \frac{2\pi}{365} D \tag{3.33}$$

Where D is the number of days since September 21 as stated in Table.3.1. Finally, using equations 3.31 and 3.32 the Sun direction in the body frame can then be computed as:

$$\hat{s}_b = C_{bi} C_{i\epsilon} \hat{r}_\epsilon \tag{3.34}$$

where C_{bi} is the rotation matrix for the inertial to body frame stated in equation 2.7.

3.6 Attitude Determination

As seen in Fig. 3.13, the Sun vector position output from the ephemeris block is used in the attitude determination block to find the satellite's attitude towards the Sun. Since the payloads should always be facing the Sun, the Sun pointing reference axis would be considered the payload's normal vector.

$$\hat{r}_{ref} = \begin{bmatrix} -1 \\ 0 \\ 0 \end{bmatrix}$$

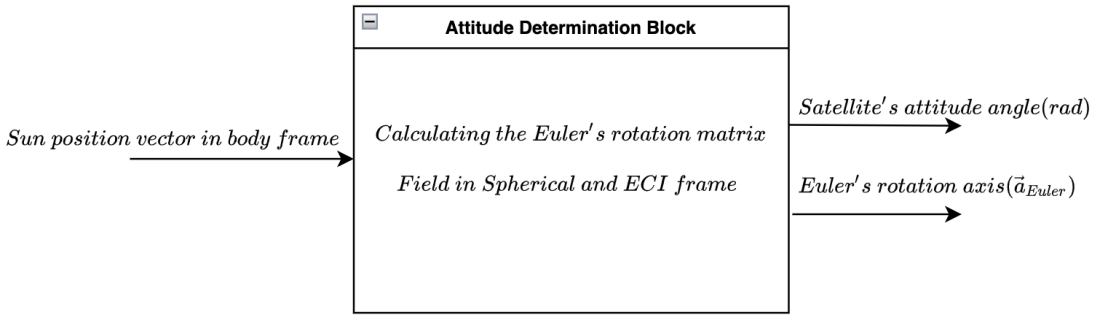


Figure 3.13: Simplified block diagram of attitude determination algorithm

Further, the Euler's rotation axis ($\vec{a}_{Euler}$) according to the Euler's theorem can be written as:

$$\vec{a}_{Euler} = \hat{r}_{\text{sun}} \times \hat{r}_{\text{ref}} \tag{3.35}$$

using cross product properties, one can obtain:

$$\begin{aligned} |\vec{a}_{Euler}| &= |\hat{r}_{\text{sun}}|\,|\hat{r}_{\text{ref}}|\sin\theta_p \\ |\hat{r}_{\text{sun}}| &= |\hat{r}_{ref}| = 1 \\ |\vec{a}_{Euler}| &= \sin\theta_p = |\hat{r}_{\text{sun}} \times \hat{r}_{\text{ref}}| \\ \theta_p &= sin^{-1}|\vec{a}_{Euler}| \end{aligned} \tag{3.36}$$

θ_p in the equation 3.36 is the satellite's pointing angle in $radian$ according to the sun attitude reference and would be further used to determine the battery's State of Charge (SOC). All these assumptions are true as long as the sun is in the sun sensor's view.

As described earlier, when the illumination phase ends and the CubeSat enters the eclipse, the sun sensors do not provide any measurement output. The EKF algorithm is used in the eclipse to estimate the satellite's attitude using gyroscope measurements. Figure 3.14 shows a schematic of the EKF block ports.

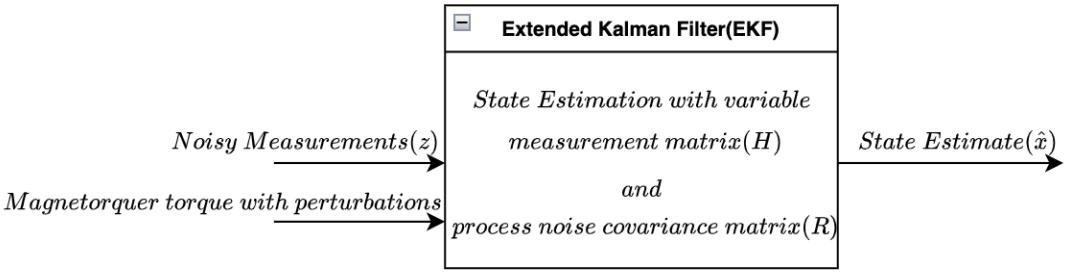


Figure 3.14: Simplified block diagram of EKF Block

In the EKF input port, the noisy measurements would change size from 5 in illumination time to 3 in eclipse. The noises are added to the gyroscope and sun sensor measurements as a vector input and consequently to the block. Further, the algorithm is running in real-time without any delay. Moreover, the algorithm would automatically adjust itself to the number of measurements by switching to a different size of the measurement matrix(H) and process noise covariance(R) matrices. A detailed explanation of EKF is given in the next chapter.

3.7 Controller Block

Most spacecraft are stabilized through a combination of passive control (dynamics only) and active control in which the spacecraft use at least one sensor, one actuator, one energy source, and control law. Iris in detumbling mode is stabilized by an active controller (detumbling control) and by passive-active strategies in fine pointing mode shown in Fig. 3.15. Both controllers are elaborated on in the following.

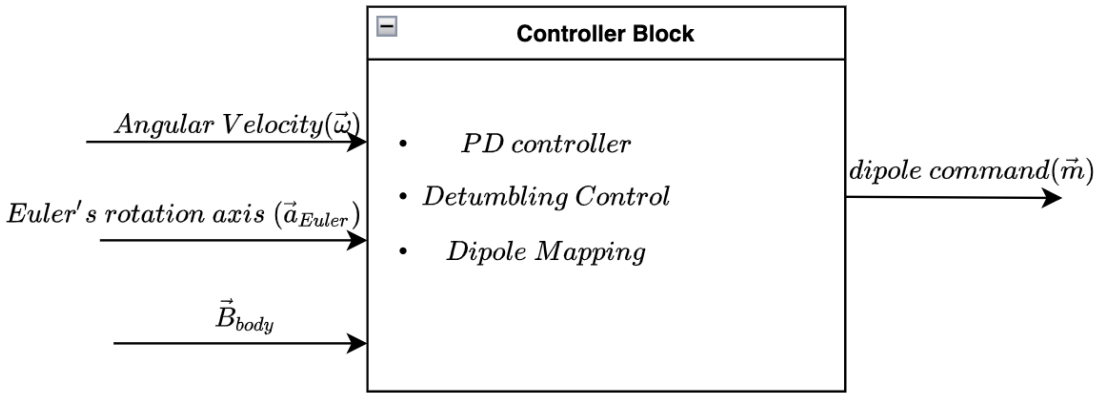


Figure 3.15: Simplified block diagram of controller algorithm

3.7.1 Detumbling Mode

Following separation from the launch deployer, Iris will have residual body rates resulting from imperfect springs that push the spacecraft away from the deployer, which would be up to a maximum of $5°/s$ per axis. A detumble control law is desired that relies on the magnetometer rather than the gyros.

As said earlier in the mission description, Iris is an under-actuated system, being controlled only by three orthogonal magnetorquer rods. The torque generated by the torque rods depends on the local magnetic field per:

$$\vec{T}_{\text{mag}} = \vec{m} \times \vec{B}$$

Therefore reconsidering the equations 1.1 and 1.2, the system dynamics for magnetic control yield:

$$\vec{m} \times \vec{B}_b = I\dot{\vec{\omega}} + \vec{\omega} \times I\vec{\omega}$$

Where $\vec{m}$ is the magnetorquer produced magnetic dipole moment and $\vec{B}_b$ is the Earth's magnetic field vector in Tesla in the body frame. Hence, the detumbling controller will take the form of B-dot control laws command expressed in equation 3.37 [13].

$$\vec{m} = -K_{det}\dot{\vec{B}} \tag{3.37}$$

The ADC subsystem will implement a linear filtered derivative on the magnetometers' noisy measurements to differentiate the magnetic field. The derivative is defined using a first-order state variable filter:

$$H(s) = \frac{\dot{\vec{B}}_b}{\vec{B}_b}(s) = \frac{s\omega_c}{s + \omega_c} \tag{3.38}$$

where $\dot{\vec{B}}_b$ is the estimate of the time derivative of $\vec{B}_b$ and ω_c is the filtering cut off frequency which is considered as 0.2 Hz. The actuator's duty cycle would be 50% since the magnetorquers are not operating while the magnetometers are sampling the measurement.

3.7.2 Fine pointing Mode

The goal of the pointing controller can be mathematically expressed as applying the required torques to maintain the desired pointing orientation, which will be Sun-facing. Spin stabilization will be used as a passive control method to maintain the pointing orientation during periods of uncontrollability. For the Iris ADC design, a desired spin rate about the major axis is chosen:

$$\vec{\omega}_{spin} = \begin{bmatrix} \omega_{\text{spin}} \\ 0 \\ 0 \end{bmatrix} \text{deg/sec} \tag{3.39}$$

where ω_{spin} in equation 3.39 is the spinning rate about the x-axis. Regarding equation 3.39, the controller is tracking a $1\ \mathrm{deg/sec}$ spinning rate about the $-x$-axis. The spinning axis as seen in Fig. 3.19 is normal to the payload window and the norm of spin rate is determined through the performance tuning. The spin rate is chosen big enough to make the effect of the disturbing torque smaller. That is, any spin rate less than $1\ deg/sec$ can not completely reject the disturbances and guarantee the stability.

The control law for pointing is a conventional PD, based on the attitude axis and the angular velocity with respect to the body frame expressed in equation 3.40:

$$\vec{T}_{controller} = K_p \vec{a}_{Euler} + K_d \left(\vec{\omega}_{spin} - \vec{\omega}_b\right) \tag{3.40}$$

where ω_b is the gyroscope measurements of body rates and K_p and K_d are the proportional term and the rate damping term, respectively. The control law will damp the body rates alongside tracking the sun vector position.

As stated in equation 3.36, and regarding the Euler's theorem, $\vec{a}_{Euler}$ represents the Euler axis which describes the angular deviation (θ_p) between the desired pointing orientation and the actual pointing orientation.

Equation 3.40 is the entire torque that actuators provide. However, the only torques that are effective are those that are perpendicular to $\vec{B}$. A mapping function ensures that the dipole moment is always perpendicular to the magnetic field. Therefore, to remove the component of the moment vector which contributes no torque, it can be obtained [13]:

$$\vec{m}_{mapped} = \frac{\vec{B}_b}{\left|\vec{B}_b\right|^2} \times \vec{T}_{controller} \tag{3.41}$$

The torque mapping in equation 3.41 may result in dipole commands that cause the magnetic actuators to saturate. When one or more axes are saturated, it may cause incorrect directions of control dipoles. This could lead to instabilities as the controller may be applying torques in the wrong direction.

To overcome the magnetorquer saturation challenge, the entire commanded dipole vector, $\vec{m}$ is scaled by a factor that reduces the maximum dipole to be at the saturation limit, with all other axes at smaller magnitudes that maintain the desired direction. The dipole scaling is effective only when at least one magnetorquer is saturated and is not always happening. Shown in Fig. 3.16 and written out mathematically, the scaling gain is noted with K_s and is equal to:

$$K_s = \frac{m_{sat}}{\max |\vec{m}_{mapped}|} \tag{3.42}$$

where m_{sat} corresponds to the saturation threshold value and is equal to $0.1731\ (A.m^2)$. Finally, then, the actual commanded dipole to the magnetorquers is:

$$\vec{m}_{command} = K_s\ \vec{m}_{mapped} \tag{3.43}$$

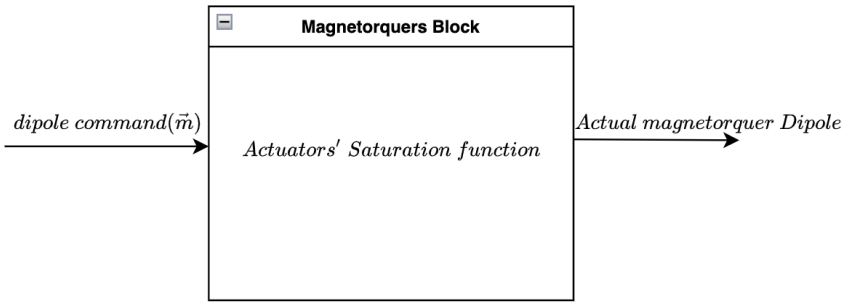


Figure 3.16: Saturation block will adjust the dipole moment below threshold while preventing actuators saturation at the same time

As the last step, it should be considered that according to the angle control, the satellite may stabilize backward at $180\ (deg)$. Hence the pointing angle should be adjusted. Figure 3.17 demonstrates the actual Simulink block, which redirects the control input after the saturation adjustment.

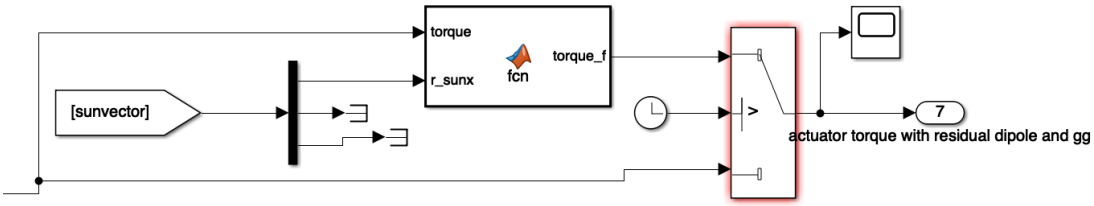


Figure 3.17: Negating torque in order to control the angle not to stabilize backward

In order to describe the situation, let's examine the frame as depicted in Fig. 3.19. Whenever the x component of the sun position vector is in the positive region, the controller torque will be negated. This torque command will result in tracking the reference vector of $[-1, 0, 0]$ in the body frame.

3.7.3 MOI Tensor

After being released from the launch system, the Iris satellite is stowed and tumbling before the initial commissioning of ADCS start. The solar panels will be deployed after a few orbits when the CubeSat is detumbled by the B-dot control algorithm. Below is the moment of inertia from the Iris satellite while stowed (Fig. 3.18):

$$I_{stowed} = \begin{bmatrix} 3.57 & 0.00752 & 0.000647 \\ 0.00752 & 3.61 & 0.0108 \\ 0.000647 & 0.0108 & 0.737 \end{bmatrix} \times 10^{-2}\ kg\ m^2 \tag{3.44}$$

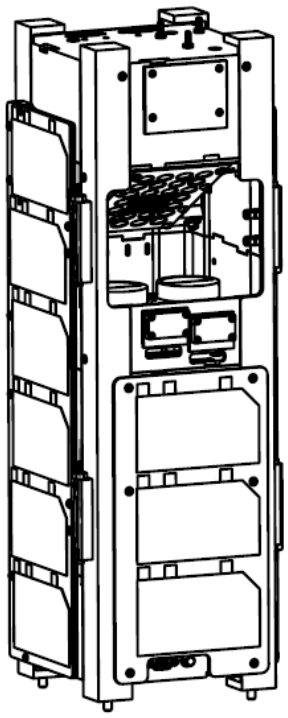


Figure 3.18: Iris full assembly stowed

Using diagonalization techniques, the MOI tensor in the principal axis could be written as:

$$I_{stowed,prin} = \begin{bmatrix} 3.57 & 0 & 0 \\ 0 & 3.61 & 0 \\ 0 & 0 & 0.74 \end{bmatrix} \times 10^{-2}\ kg\ m^2 \tag{3.45}$$

After deployment of the solar arrays and the antenna, as shown in figure 3.19, the new inertia tensor is predicted as:

$$I_{deployed} = \begin{bmatrix} 4.53 & -0.0015 & 0.2375 \\ -0.0015 & 4.36 & -0.0070 \\ 0.2375 & -0.0070 & 1.30 \end{bmatrix} \times 10^{-2}\ kg\ m^2 \tag{3.46}$$

Similar to the stowed position, the MOI tensor after deployment about the principal axis could be written as:

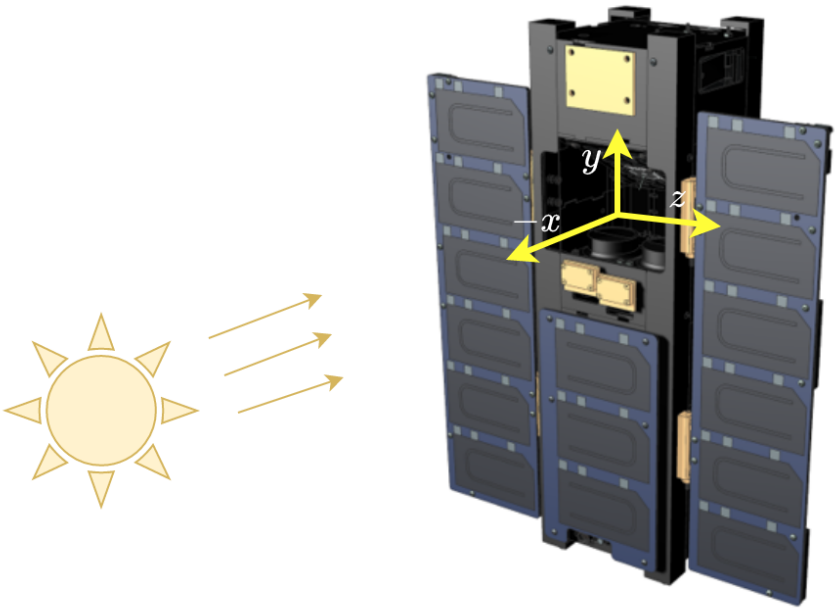


Figure 3.19: Iris full assembly deployed

$$I_{deployed,prin} = \begin{bmatrix} 4.55 & 0 & 0 \\ 0 & 4.36 & 0 \\ 0 & 0 & 1.28 \end{bmatrix} \times 10^{-2}\ kg\ m^2 \tag{3.47}$$

Regarding the major axis rule, spinning solely about the major axis (which is the axis with the maximum inertia) is stable and the gyric stiffness of the spin help with the energy dissipation and disturbance rejection while providing stability [19]. After the solar panels' deployment, the major axis changes from the y axis to the x axis. Regarding Fig. 2.1 the $1\ deg/sec$ spin about the $-x$ axis does not affect the payload science data or the power generation of the solar panels.

It is essential to know accurately and update and switch the spacecraft moments of inertia between the stowed and deployed modes in the simulation.

3.8 Magnetorquers Power Consumption

The power consumption block's goal is to observe the torque rods and how much it would affect the total power, specifically in detumbling mode when the power is scarce. The block diagram is shown in Fig. 3.20.

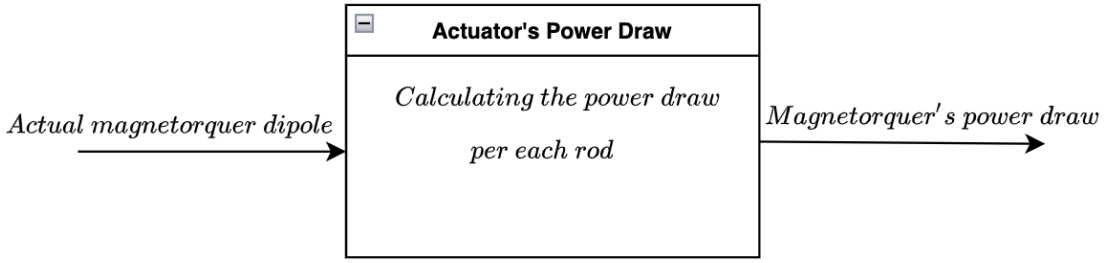


Figure 3.20: Simplified block diagram of torque rod's power algorithm

The ratio of dipole moment to power can be calculated with a second-order function shown below:

$$P = (\frac{m}{N})^2 \tag{3.48}$$

Where N is a constant that, when calculated for the torque rods, is 0.3979 [10]. The maximum power generated by torque rods is $0.2\ (W)$. Other properties of magnetorquers are elaborated in Table 3.2. The ADCS hardware specifications are shown below [54]:

Parameter (Variable)	Value	Units
Maximum Power (P)	0.2	W
Voltage (V)	5	V
Total Resistance (R)	125	Ω
Length of Wire (l_w)	91.91	m
Radius of Wire (r_w)	0.0625	mm
Density of Wire (ρ_w)	8.96	$\mathrm{g/cm^3}$
Resistivity of Wire (W_w)	1.36	$\frac{\Omega}{\mathrm{m}}$
Number of Turns (N)	5119	
Number of Wraps (N_{wr})	13	
Radius of Core (r_c)	2.8575	mm
Length of Core (l_c)	5	cm
Density of Core (ρ_c)	8.74	$\mathrm{g/cm^3}$
Relative Permittivity of the Core (μ_r)	$100,000$	
Demagnetising Factor (N_d)	0.0253	
Maximum Magnetic Moment (D)	0.1731	$\mathrm{A/m^2}$
Total Mass (m_{total})	21.6	g
Total Wound Radius (r_{total})	4.5	mm

Table 3.2: ADCS Hardware specifications [54]

3.9 Power Analysis Block

The Power Analysis block, as seen in Fig. 3.21 is a modification from a thesis done as the ground station and power system design of the Iris Satellite in 2019-2021 [55]. This block focuses on Iris's SOC, as it is a helpful indicator if a spacecraft can complete the attitude maneuvers before the batteries are drained. As a specific example, an analysis has been done to find the worst-case scenario for the power subsystem.

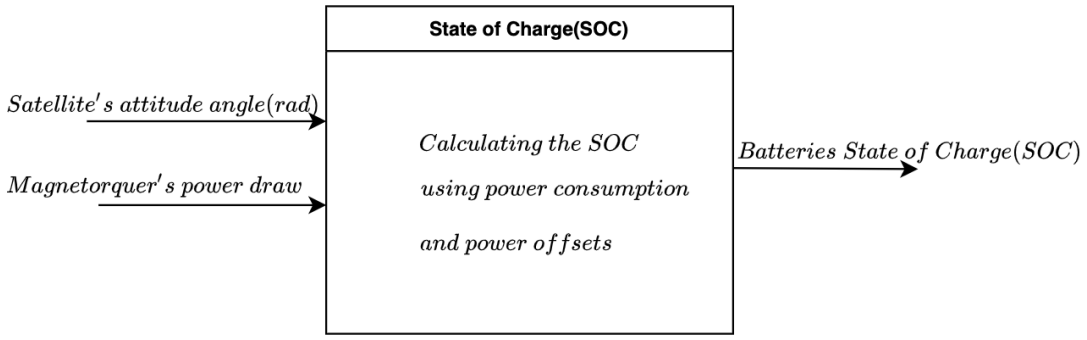


Figure 3.21: Simplified block diagram of power analysis algorithm [55]

As seen in Figs. 3.18 and 3.19, the power generation would be different in the stowed configuration mode compared to the deployed configuration. In the stowed configuration, as seen in Fig. 3.18, the solar panels are normal to the $\pm z\ axis$ while after deployment, the panels are normal to the $-x\ axis$.

The power subsystem consists of seven solar arrays in total. As seen in Fig. 3.18, in stowed configuration, one solar array is installed below the geology samples normal to the $-x\ axis$. Two arrays are installed normal to the $+x$ axis, and two arrays are installed on each of the solar panels normal to the $+z$ or $-z$ axes. However, when the solar panels are deployed as in Fig.3.19, there are five solar arrays normal to the $-x$ face and two solar arrays on the $+x$ face which are generating power.

When the satellite is released from the deployer, the CubeSat is in the stowed configuration. It's assumed that the detumbling phase starts in this state while the magnetorquers, microcontroller, magnetometer, thermal heaters and power subsystem are operating. The values considered as the power consumption offsets in the stowed configuration are presented in Table. 3.3.

After the detumbling controller successfully reduces the body rates to less than $0.5\ deg/sec$, the solar panels and the antenna deploy. Table. 3.4 demonstrates the component-wise power consumption in the deployed configuration. At this point, it's assumed that the commissioning is over and all the subsystems operate in the nominal mode.

Parameter	Value	Units
Magnetorquers Power draw	$simulation$	W
Micro controller and magnetometer	0.0017292	W
Thermal Subsystem offset	1.5	W
Power Subsystem offset	0.5	W
Maximum Subsystems' Power usage (before commissioning and deployment)	4.964	W

Table 3.3: Power consumption offsets in stowed configuration mode by components

Parameter	Value	Units
Magnetorquers Power draw	$simulation$	W
ADCS sensors and micro controller	0.06685	W
Thermal Subsystem offset	1.5	W
Power Subsystem offset	0.5	W
COMMS Subsystem offset	0.9	W
CDH Subsystem offset	1.38	W
Payload Subsystem offset	0.85	W
Maximum Subsystems' Power usage (in nominal mode)	5.745	W

Table 3.4: Power consumption offsets in deployed configuration mode by components

In order to find the actual solar current in the solar arrays, the satellite's attitude must be used. The cosine of the attitude known from the attitude determination block ($cos\theta$) is multiplied by the total solar current as seen in equation 3.49 to find the remaining charge of the power subsystem.

$$I_{actual} = I_{total} cos\theta \tag{3.49}$$

$$SOC = \int (I_{actual} - I_{battery}) dt \tag{3.50}$$

The method used in equation 3.50 is called "Coulomb counting" and calculates the SOC by integrating the current in time [56].

In the stowed configuration mode, the satellite's attitude must be calculated relative to the reference axes of $\pm x$ and $\pm z$ while multiplying the cosine of the angle in the corresponding current. In the deployed configuration mode, the satellite's attitude is considered only with respect to $\pm x$ as reference vectors.

The worst-case scenario will happen if the CubeSat is released from the deployer, spinning

about the intermediate z-axis in the body frame with $[0; 0; -5]\ deg/sec$. The result will efficiently show a sharp decline in the SOC at the beginning of the detumbling, which would recover after seven orbits. The corresponding results and mission requirements are shown in Section 5.6.

3.10 Summary of the Chapter

This chapter presents the simulation design and development of the Iris CubeSat attitude determination and control subsystem (ADCS). The design factor for the ADCS is to spin up the CubeSat to $1\ deg/sec$ and to acquire the $\pm 21\ deg$ attitude during the illumination phase.

Nine blocks were designed to support the mission requirements. I chose the order of the blocks so that the inputs and output ports can be explained accurately.

The SGP4 propagator initiates with the TLE borrowed from the ISS mission and propagates the orbital elements in time. The earth's magnetic field block uses the earth's dipole potential function to calculate the magnetic field in ECI or inertial frame and simulate the three-axis magnetometer. The environmental block adds the disturbance torques to the torque of the magnetic actuator, acting similar to the actual mission environment. The dynamics block simulates the three-axis gyroscopes by mathematically deriving the angular velocity vector. The solar ephemeris and attitude determination blocks efficiently simulate the two-axis sun sensor. The EKF block inputs the controller block with attitude estimation in the eclipse. The controller block simulates the torque rods and the control signals, which the onboard computer will command. Finally, the magnetorquer power consumption and power analysis block simulate the power interface. The simulation fulfills all mission requirements.

Chapter 4

EKF Based Sun Vector Estimation

Although it would add to the computational effort, designing an estimator would improve the control. For instance, when the satellite is in the eclipse, the attitude prediction would aid the CubeSat in performing maneuvers and maintaining its pointing without sun sensor measurements.

There are several methods available to estimate the sun position vector, such as deterministic single-point methods and filtering algorithms [57]. Filtering algorithms such as Kalman Filter combine sensor measurements over a continuous time with a dynamic model to estimate the state variable.

Extended Kalman Filter (EKF) is similar in principle to the Kalman Filter. The EKF involves locally linearizing the nonlinearities present in the system's process and measurement models. The linear equations, linearized about the latest available estimate, are used to propagate the next state and covariance matrix estimate.

Two different scenarios based on Extended Kalman Filter approach are presented in this thesis.

First, both sun vector position and angular velocity are estimated during the illumination and eclipse phase. The sun sensors would not identify the sun's attitude in the eclipse phase, so an estimator would help estimate the sun attitude states with gyroscope measurements. In section 5.3.3, in an offline simulation, both sun sensor and gyroscope sensors are available and estimated. While in eclipse the attitude vector is estimated with gyroscope output.

Second, the EKF algorithm is implemented in the simulator to provide the real-time system with attitude estimates during eclipse. The EKF-based attitude vector output improves the control and the steady state pointing error. The simulation steps and the results are examined in Section

5.5.

In this chapter first the system model will be presented. Hence, an innovative dimension reduction strategy and system state variables would be introduced. Finally, the EKF algorithms and the definitions would be defined.

4.1 System Model

This section defines the mathematical expressions of the system model for the Iris mission. In this research, the EKF algorithm would provide a reliable estimate for the sun-direction vector and body rates using sun sensors and gyroscopes. During the eclipse phase the algorithm would only rely on gyroscopes measurements.

If $\vec{S}$ indicates the sun direction vector, from vector calculus the equation 4.1 can be derived which would relate the angular velocity ($\vec{w}_b$) and sun vector.

$$\overset{o}{\vec{S}} = \dot{\vec{S}}_b + \vec{w}_b \times \vec{S}_b \tag{4.1}$$

where $\overset{o}{\vec{S}}$ is the derivative of S in the inertial frame and the $\dot{\vec{S}}$ is the derivative of S in body frame. The left-hand side of equation 4.1 is very small relative to the right hand side terms since the variation of the sun position vector in the Inertial frame is negligible and can be treated as a noise [58].

Now it can be inferred:

$$\dot{\vec{S}}_b = \vec{S}_b \times \vec{w}_b \tag{4.2}$$

Thus from equation 4.2, it can be obtained:

$$\dot{S}_b = S_b^{\times} w_b \tag{4.3}$$

Or in vector form the rate of change of S_b can be defined as:

$$\dot{S}_b = \begin{bmatrix} \dot{s}_1 \\ \dot{s}_2 \\ \dot{s}_3 \end{bmatrix} = \begin{bmatrix} 0 & -s_3 & s_2 \\ s_3 & 0 & -s_1 \\ -s_2 & s_1 & 0 \end{bmatrix} \begin{bmatrix} w_1 \\ w_2 \\ w_3 \end{bmatrix} = \begin{bmatrix} -s_3 w_2 + s_2 w_3 \\ s_3 w_1 - s_1 w_3 \\ -s_2 w_1 + s_1 w_2 \end{bmatrix} \tag{4.4}$$

On the other hand the variation of body rates shall be defined. Equation 2.1 is repeated below, which represents the Euler equation:

$$T = I\dot{w}_b + w_b \times (Iw_b)$$

If the $\dot{\omega}$ is isolated:

$$\dot{w_b} = I^{-1}(T - w_b \times (Iw_b)) \tag{4.5}$$

As mentioned before the (I) matrix will be the principal moment of Inertia. Equation 4.5 can be written in vector form with respect to the principal frame:

$$\begin{bmatrix} \dot{w}_1 \\ \dot{w}_2 \\ \dot{w}_3 \end{bmatrix} = \begin{bmatrix} \frac{1}{I_1} & 0 & 0 \\ 0 & \frac{1}{I_2} & 0 \\ 0 & 0 & \frac{1}{I_3} \end{bmatrix} \left(\begin{bmatrix} T_1 \\ T_2 \\ T_3 \end{bmatrix} - \begin{bmatrix} (I_3 - I_2) w_2 w_3 \\ (I_1 - I_3) w_1 w_3 \\ (I_3 - I_1) w_1 w_2 \end{bmatrix} \right) = \begin{bmatrix} \frac{T_1}{I_1} - \frac{(I_3 - I_2) w_2 w_3}{I_1} \\ \frac{T_2}{I_2} - \frac{(I_1 - I_3) w_1 w_3}{I_2} \\ \frac{T_3}{I_3} - \frac{(I_2 - I_1) w_1 w_2}{I_3} \end{bmatrix} \tag{4.6}$$

In summary, from the two dynamic equations (equations 4.4 and 4.6) the state rate of change for S_b and w_b is obtained:

$$\begin{bmatrix} \dot{S}_b \\ \dot{w}_b \end{bmatrix} = \begin{bmatrix} \dot{s}_1 \\ \dot{s}_2 \\ \dot{s}_3 \\ \dot{w}_1 \\ \dot{w}_2 \\ \dot{w}_3 \end{bmatrix} = \begin{bmatrix} -s_3 w_2 + s_2 w_3 \\ s_3 w_1 - s_1 w_3 \\ -s_2 w_1 + s_1 w_2 \\ \frac{T_1}{I_1} - \frac{(I_3 - I_2) w_2 w_3}{I_1} \\ \frac{T_2}{I_2} - \frac{(I_1 - I_3) w_1 w_3}{I_2} \\ \frac{T_3}{I_3} - \frac{(I_2 - I_1) w_1 w_2}{I_3} \end{bmatrix} \tag{4.7}$$

The equation 4.7 will be used to derive the final state space for the system model.

4.2 Sun Sensor Representation of Sun Position Vector

As it can be seen in Fig. 4.1, the sunbeam reaches the sun sensor via an aperture on the sun sensor mask. Therefore, the sun sensor would have a 2D representation of the sun vector.

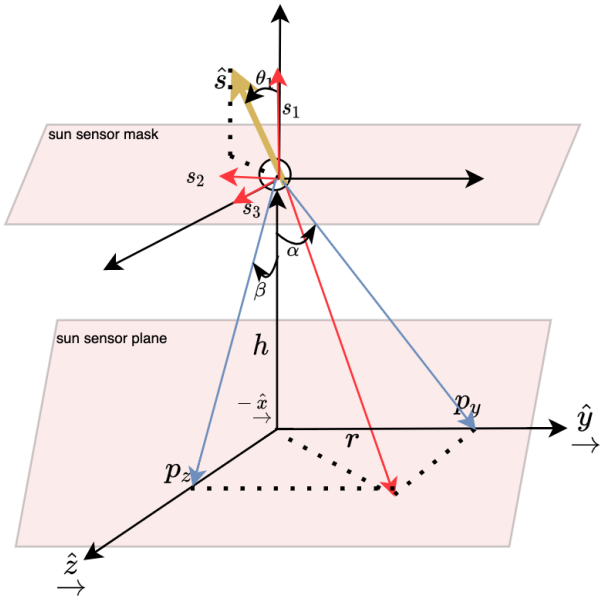


Figure 4.1: Geometric representation of the Sun sensor and sun sensor's mask. The unit sun vector is shown with $\hat{s}$ and the angle θ_1 is the satellite's attitude angle towards sun. α is the angle between the sun vector projection and $-x$ axis. Similarly, β is the angle between the sun vector projection on the $x-z$ plane and $-x$ axis.

The $-x$ axis is normal to the sun sensor plane hence the sun vector would be projected on the $y-z$ plane. In this way, the sun vector would be presented by:

$$r_{pr} = \begin{bmatrix} 0 \\ p_y \\ p_z \end{bmatrix} \tag{4.8}$$

where r_{pr} is the projected sun attitude on the sun sensor plane.

Here to better illustrate the geometry of the 2D problem, Figures 4.2 and 4.3 are presented.

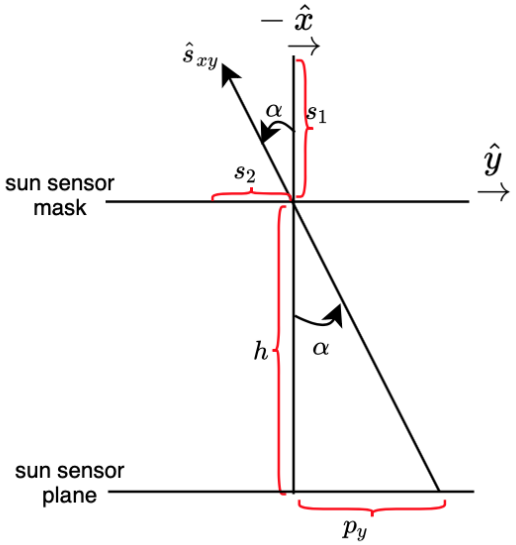


Figure 4.2: 2D Projection of sun vector on the x-y plane

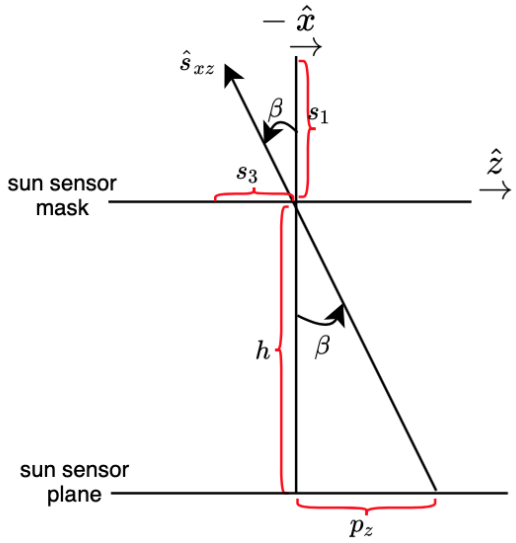


Figure 4.3: 2D Projection of sun vector on the x-z plane

Regarding Fig. 4.2 it can be inferred:

$$tan\alpha = \frac{s_2}{s_1} = \frac{p_y}{h} \tag{4.9}$$

Isolating p_y and since we know the mask and sensor's plane fits in $y - z$ axes plane:

$$p_y = h\frac{s_2}{s_1} = h\frac{s_2}{\sqrt{1 - s_2^2 - s_3^2}} \tag{4.10}$$

Similarly, for p_z regarding Fig .4.3 from the tangent relation it can be written:

$$tan\beta = \frac{s_3}{s_1} = \frac{p_z}{h} \tag{4.11}$$

Hence:

$$p_z = h\frac{s_3}{s_1} = h\frac{s_3}{\sqrt{1 - s_2^2 - s_3^2}} \tag{4.12}$$

To sum up, the state vectors in this study includes 5 states and is defined as equation 4.13:

$$x = \begin{bmatrix} p_y \\ p_z \\ w_1 \\ w_2 \\ w_3 \end{bmatrix} \tag{4.13}$$

where p_y and p_z are the measurements of two-axis sun sensor and w_1,w_2 and w_3 are the output of three-axis gyroscopes.

4.2.1 Dimension Reduction Strategy in EKF

As mentioned before, the sun vector is always constrained to be a unit vector. Therefore, the third element can be written as an algebraic relation of the first two elements which also represent the two degrees of freedom (DOF) of the sun sensor. In this scenario, a state that is not truly independent cannot be reliably estimated, so a reduced order strategy is needed to reduce the order of the EKF algorithm from 6 to 5.

As the presented EKF algorithm will be used autonomously onboard CubeSat, computational speed is essential due to computer processing limitations. The dimension reduction strategy also improves the processing speed.

I have defined the projection of the sun attitude vector on the $y-z$ plane with two elements of p_y and p_z. Additionally, I've assumed h is $1\ mm$ in the simulation. Generally, as seen in Fig. 4.1 the sun beam can be described by a vector (here called as P_{ss}) such as equation 4.14 after passing the aperture:

$$P_{ss} = \begin{bmatrix} h \\ p_y \\ p_z \end{bmatrix} \tag{4.14}$$

In order to derive the required $\dot{p}_y$ and $\dot{p}_z$ states, the equation 4.40 and 4.12 are differentiated

and simultaneously $\dot{h} = 0$.

$$\dot{p}_y = h\left(\frac{s_1\dot{s}_2 - s_2\dot{s}_1}{s_1^2}\right) = h\left(\frac{\dot{s}_2}{s_1} - \frac{s_2\dot{s}_1}{s_1^2}\right) \tag{4.15}$$

$$\dot{p}_z = h\left(\frac{s_1\dot{s}_3 - s_3\dot{s}_1}{s_1^2}\right) = h\left(\frac{\dot{s}_3}{s_1} - \frac{s_3\dot{s}_1}{s_1^2}\right) \tag{4.16}$$

Substituting $\dot{s}_1 = -s_3w_2 + s_2w_3$, $\dot{s}_2 = s_3w_1 - s_1w_3$ and $\dot{s}_3 = -s_2w_1 + s_1w_2$ and isolating the fractions, the equations yield:

$$\dot{p}_y = h\left(\frac{s_3w_1 - s_1w_3}{s_1} - \frac{s_2(-s_3w_2 + s_2w_3)}{s_1^2}\right) = h\left(\frac{s_3}{s_1}w_1 - w_3 - \frac{s_2}{s_1}\left(\frac{-s_3}{s_1}w_2 + \frac{s_2}{s_1}w_3\right)\right) \tag{4.17}$$

$$\dot{p}_z = h\left(\frac{-s_2w_1 + s_1w_2}{s_1} - \frac{s_3(-s_3w_2 + s_2w_3)}{s_1^2}\right) = h\left(\frac{-s_2}{s_1}w_1 + w_2 - \frac{s_3}{s_1}\left(\frac{-s_3}{s_1}w_2 + \frac{s_2}{s_1}w_3\right)\right) \tag{4.18}$$

Substituting $p_y = h\frac{s_2}{s_1}$ and $p_z = h\frac{s_3}{s_1}$, it can be inferred:

$$\dot{p}_y = h\left(\frac{p_z}{h}w_1 - w_3 - \frac{p_y}{h}\left(\frac{-p_z}{h}w_2 + \frac{p_y}{h}w_3\right)\right) = p_zw_1 - hw_3 - p_y\left(\frac{-p_z}{h}w_2 + \frac{p_y}{h}w_3\right) \tag{4.19}$$

$$\dot{p}_z = h\left(\frac{-p_y}{h}w_1 + w_2 - \frac{p_z}{h}\left(\frac{-p_z}{h}w_2 + \frac{p_y}{h}w_3\right)\right) = -p_yw_1 + hw_2 - p_z\left(\frac{-p_z}{h}w_2 + \frac{p_y}{h}w_3\right) \tag{4.20}$$

Finally:

$$\dot{p}_y = p_zw_1 - hw_3 + \frac{p_yp_z}{h}w_2 - \frac{p_y^2}{h}w_3 \tag{4.21}$$

$$\dot{p}_z = -p_yw_1 + hw_2 + \frac{p_z^2}{h}w_2 - \frac{p_yp_z}{h}w_3 \tag{4.22}$$

Finally, using equations 4.21, 4.22 and 4.6 the state-space formulation of the reduced 5 state

variables can be assembled as in equation 4.23:

$$\dot{x} = \begin{bmatrix} f_1 \\ f_2 \\ f_3 \\ f_4 \\ f_5 \end{bmatrix} = \begin{bmatrix} \dot{p_y} \\ \dot{p_z} \\ \dot{w}_1 \\ \dot{w}_2 \\ \dot{w}_3 \end{bmatrix} = \begin{bmatrix} p_z w_1 - h w_3 + \frac{p_y p_z}{h} w_2 - \frac{p_y^2}{h} w_3 \\ -p_y w_1 + h w_2 + \frac{p_z^2}{h} w_2 - \frac{p_y p_z}{h} w_3 \\ \frac{T_1}{I_1} - \frac{(I_3 - I_2) w_2 w_3}{I_1} \\ \frac{T_2}{I_2} - \frac{(I_1 - I_3) w_1 w_3}{I_2} \\ \frac{T_3}{I_3} - \frac{(I_2 - I_1) w_1 w_2}{I_3} \end{bmatrix} \tag{4.23}$$

The Runge-Kutta fourth-order method has been coded so that the nonlinear equations are integrated as a coupled system of differential equations.

4.3 EKF Algorithm and Definitions

In the EKF, estimation and update are the two main steps. As seen in Fig. 4.4, if measurements are not available the algorithm relies on the first step for either state vector or error covariance estimation [59]. If the non-measurement period is too long, the error would be accumulated, and the final results may not be accurate.

Below are the definitions of the variables used in the EKF algorithm and a summary of the algorithm is shown in Fig 4.4. In the following sections each variable would be elaborated.

- $\hat{x}_k^-$ = A priori state estimate based on knowledge of the process in step $k-1$
- $\hat{x}_k$ = A posteriori state estimate based on knowledge of measurements in step k
- P_k^- = A priori estimate error covariance
- P_k = A posteriori estimate error covariance
- A_k = The Jacobian of the system model equations
- K_k = The Kalman gain that minimizes the posteriori estimate of error covariance P_k
- H = Measurement matrix

- Q_k = Covariance Matrix of process noise
- R = Covariance Matrix of sensor noise

The reason behind the names priori and posteriori, is the measurement updates.

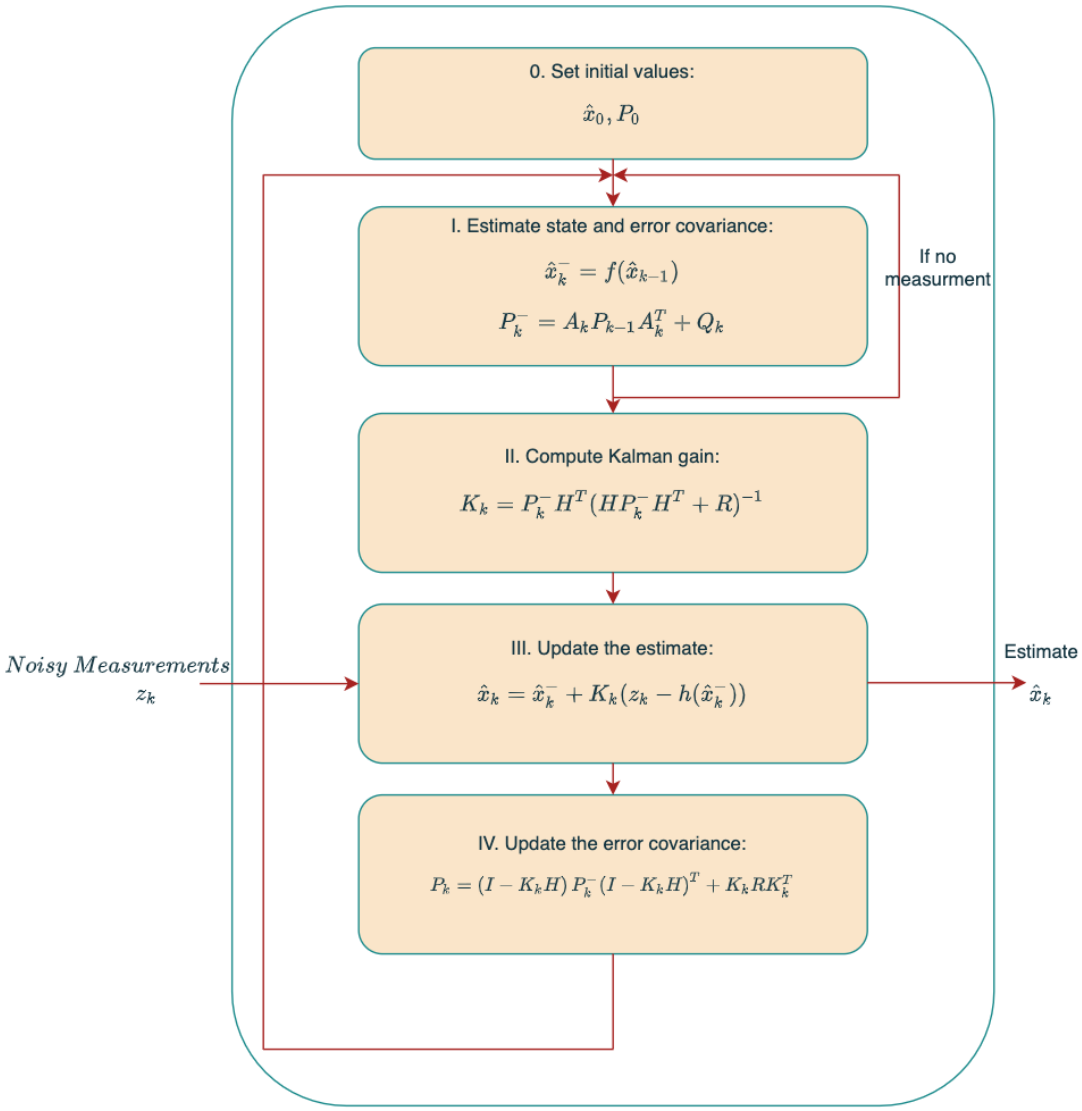


Figure 4.4: EKF general flow diagram

4.3.1 EKF Model Linearization

Before addressing the EKF algorithm, topics such as linearization and discretization should be raised. For nonlinear continuous systems, the general differential equation may be written as (equations 4.24 and 4.25):

$$\dot{x} = f(x, u) + w \tag{4.24}$$

and

$$z = h(x) + v \tag{4.25}$$

Where x is the state vector, z is the measurement vector and w and v parameters are white Gaussian noise with zero mean added to the system dynamics and measurements respectively.

Since the EKF deals with discrete systems, the discrete form of the general difference equation for a nonlinear system can be defined as:

$$x_k = f(x_{k-1}, u_{k-1}) + w_{k-1} \tag{4.26}$$

and

$$z_k = h(x_k) + v_k \tag{4.27}$$

where k shows the discrete time step.

The variables w_k and v_k are represented by their covariance matrices Q and R respectively.

$$w \sim N(0, Q), \quad v \sim N(0, R). \tag{4.28}$$

where N defines a normal distribution.

The system dynamic equations should be locally linearized then descritized. Linearizing the

two governing equations of system model yield:

$$\begin{aligned} \dot{x}(t) &= \boldsymbol{A}x(t) + \boldsymbol{B}\boldsymbol{u}(t) \\ z(t) &= \boldsymbol{H}x(t) + \boldsymbol{D}\boldsymbol{u}(t) \end{aligned} \tag{4.29}$$

with

$$\boldsymbol{A} = \frac{\partial f}{\partial x}|_{x_0(t),u_0(t)} = \begin{bmatrix} \frac{df_1}{dx_1} & \dots & \frac{df_1}{dx_n} \\ \dots & \dots & \dots \\ \frac{df_n}{dx_1} & \dots & \frac{df_n}{dx_n} \end{bmatrix} \tag{4.30}$$

and

$$\boldsymbol{B} = \frac{\partial f}{\partial u}|_{x_0(t),u_0(t)} = \begin{bmatrix} \frac{df_1}{du_1} & \dots & \frac{df_1}{du_n} \\ \dots & \dots & \dots \\ \frac{df_n}{du_1} & \dots & \frac{df_n}{du_n} \end{bmatrix} \tag{4.31}$$

H is the Jacobian of the measurement function which is this case is defined as measurement matrix with respect to x which can be written as:

$$\boldsymbol{H} = \frac{\partial h}{\partial x}|_{x_0(t)} = \begin{bmatrix} \frac{dh_1}{dx_1} & \dots & \frac{dh_1}{dx_n} \\ \dots & \dots & \dots \\ \frac{dh_n}{dx_1} & \dots & \frac{dh_n}{dx_n} \end{bmatrix} \tag{4.32}$$

And D is the feed-forward matrix which is zero in this study and defined by:

$$\boldsymbol{D} = \frac{\partial h}{\partial x}|_{u_0(t)} = \begin{bmatrix} \frac{dh_1}{du_1} & \dots & \frac{dh_1}{du_n} \\ \dots & \dots & \dots \\ \frac{dh_n}{du_1} & \dots & \frac{dh_n}{du_n} \end{bmatrix} \tag{4.33}$$

Further the rate of change of the system parameters and state vector, respectively is defined as:

$$\dot{x} = \begin{bmatrix} f_1 \\ f_2 \\ f_3 \\ \dots \\ \dots \\ f_n \end{bmatrix}, \quad x = \begin{bmatrix} x_1 \\ x_2 \\ x_3 \\ \dots \\ \dots \\ x_n \end{bmatrix} \tag{4.34}$$

And the control inputs are:

$$u = \begin{bmatrix} u_1 \\ u_2 \\ \dots \\ u_n \end{bmatrix} \tag{4.35}$$

The first line of equation 4.29 states that the rate of change of the system parameters can be predicted using a linear combination of the present parameters and a linear combination of control inputs. The second line states that the measurement vector combines the system parameters and a linear combination of the present control inputs.

In terms of the system model, using the equations 4.30 and 4.31 to derive the partial derivatives of the matrices A and B, it can be concluded:

$$A = \begin{bmatrix} \frac{p_z}{h}w_2 - 2\frac{p_y}{h}w_3 & w_1 + \frac{p_y}{h}w_2 & p_z & \frac{p_y p_z}{h} & -h - \frac{{p_y}^2}{h} \\ -w_1 - \frac{p_z}{h}w_3 & 2\frac{p_z}{h}w_2 - \frac{p_y}{h}w_3 & -p_y & h + \frac{p_z^2}{h} & \frac{-p_y p_z}{h} \\ 0 & 0 & 0 & -\frac{(I_3 - I_2)w_3}{I_1} & -\frac{(I_3 - I_2)w_2}{I_1} \\ 0 & 0 & -\frac{(I_1 - I_3)w_3}{I_2} & 0 & -\frac{(I_1 - I_3)w_1}{I_2} \\ 0 & 0 & -\frac{(I_2 - I_1)w_2}{I_3} & -\frac{(I_2 - I_1)w_1}{I_3} & 0 \end{bmatrix} \tag{4.36}$$

$$B = \begin{bmatrix} 0 & 0 & 0 \\ 0 & 0 & 0 \\ \frac{1}{I_1} & 0 & 0 \\ 0 & \frac{1}{I_2} & 0 \\ 0 & 0 & \frac{1}{I_3} \end{bmatrix} \tag{4.37}$$

Using the partial differentiation, the control inputs are defined as equation 4.38 associated with the three magnetic actuators:

$$u = \begin{bmatrix} T_1 \\ T_2 \\ T_3 \end{bmatrix} \tag{4.38}$$

Up until now, everything has been in the continuous form. EKF model discretization would be discussed in the following.

4.3.2 EKF Model Discretization

Subsequently, after linearization, to begin with the EKF algorithm, discretization of A and Q is needed. A is the continuous state dynamics matrix, and Q is the continuous process noise covariance matrix.

The continuous Q is defined by:

$$Q = (\sigma_{\text{unmodaccel}}) (\sigma_{\text{unmodaccel}})^T = Bw^2B^T \tag{4.39}$$

where

$$w^2 = \begin{bmatrix} w_x^2 \\ w_y^2 \\ w_z^2 \end{bmatrix} \tag{4.40}$$

$\sigma_{unmodaccel}$ refers to the unmodelled accelerations in the dynamics which should be precomputed and w is a zero-mean Gaussian noise. Inaccurate process noise modelling causes large errors in the error covariance estimate and filter divergence.

At this point, the discrete version of A and Q can be formed. To discretize both the state dynamics and the process noise covariance at the same time, first, the matrix in equation 4.41 is created [60]:

$$M = \begin{bmatrix} -A & Q\Delta t \\ \mathbf{0} & A^T \end{bmatrix} \Delta t \tag{4.41}$$

M is a block-style matrix where the dimension of the $\mathbf{0}$ block is the same dimension as A and Δt is the time step of the EKF algorithm. Next, the matrix exponential of M should be computed as equation 4.42:

$$N = e^M \tag{4.42}$$

The resulting N matrix as seen in equation 4.43 has a useful block form, from which A_k and Q_k can be derived [61]:

$$N = \begin{bmatrix} \Gamma & A_k^- Q_k \\ \mathbf{0} & A_k^T \end{bmatrix} \tag{4.43}$$

The discretized state dynamics matrix, A_k, can be obtained by transposing the lower right portion of N. Finally, if V represents the upper right portion of N, the discretized process noise covariance matrix, Q_k can be written as:

$$Q_k = A_k V \tag{4.44}$$

Q_k is the discretized process noise covariance matrix that estimates the strength of the noise entering into the system dynamic model and quantifies the accuracy of the process model. The covariance matrix consists of the variance of the variables.

Finally the discretized version of the equation 4.29 can be written as:

$$\begin{aligned} x_k &= Ax_{k-1} + Bu_{k-1} \\ z_k &= Hx_k \end{aligned} \tag{4.45}$$

4.3.3 Estimation Phase

As stated earlier, the extended Kalman filter functions as an estimation-update algorithm. The algorithm initializes with a guess. Further, the state vector and error covariance are propagated, denoted by a superscript $-$, using the state dynamics model. Then both are updated when measurements are available and the state vector and error covariance are shown without any superscript.

Equation 4.46 represents the predicted or a priori state estimate.

$$\hat{x}_k^- = F(\hat{x}_{k-1}) \tag{4.46}$$

where $\hat{x}_k^-$ is the minimum variance estimate vector at a future time in the absence of measurements. In this case it is the states derived from solving the nonlinear equations of the system model which will be discussed in Section 4.1.

In the next step, the predicted or priori error covariance estimate can be defined as shown in equation 4.47.

$$P_k^- = A_k P_{k-1} A_k^T + Q_k \tag{4.47}$$

Equation 4.47 is also called partial update of error covariance.

4.3.4 Update Phase

As shown in Fig. 4.4, if measurements exist, the optimal Kalman gain is computed.

$$K_k = P_k^- H^T (H P_k^- H^T + R)^{-1} \tag{4.48}$$

As seen in equation 4.48, (K) is the Kalman filter gain which is obtained based on the covariance matrices of the measurement noise (R), the priori error covariance estimate (P_k^-) and the measurement matrix (H).

At the time of a measurement update, the measurement equation is linear and the measurement matrix is given by equation 4.49 which is a unity matrix in illumination phase when the solar arrays are facing the sun. Due to the difference in the number of measurements in the illumination phase and the eclipse the measurement matrices change size. In eclipse the measurement matrix is reduced to a 3×5 matrix as shown in equation 4.50.

$$H_{lit} = \begin{bmatrix} 1 & 0 & 0 & 0 & 0 \\ 0 & 1 & 0 & 0 & 0 \\ 0 & 0 & 1 & 0 & 0 \\ 0 & 0 & 0 & 1 & 0 \\ 0 & 0 & 0 & 0 & 1 \end{bmatrix} \tag{4.49}$$

In eclipse the measurement matrix is:

$$H_{ecl} = \begin{bmatrix} 0 & 0 & 1 & 0 & 0 \\ 0 & 0 & 0 & 1 & 0 \\ 0 & 0 & 0 & 0 & 1 \end{bmatrix} \tag{4.50}$$

Afterward the estimate shall be computed.

$$\hat{x}_k = \hat{x}_k^- + K_k(z_k - h(\hat{x}_k^-)) \tag{4.51}$$

The $h(\hat{x}_k^-)$ term on the right hand side of equation 4.53 is the measurement equation which is linear with the state vector and can be written as equation 4.52:

$$h(\hat{x}_k^-) = H_k \hat{x}_k^- \tag{4.52}$$

Thus reconsidering equation 4.53 with a linear form measurement matrix:

$$\hat{x}_k = \hat{x}_k^- + K_k(z_k - H_k \hat{x}_k^-) \tag{4.53}$$

In the last step the updated or posteriori estimate covariance is calculated as in equation 4.54:

$$P_k = (I - K_k H)\, P_k^- \,(I - K_k H)^T + K_k R_k K_k^T \tag{4.54}$$

4.4 Conclusion

This chapter examined the system dynamic model, the general algorithm of EKF and the problem-solving method. An order-reduction technique is introduced by mapping the sun vector position on the sun sensor plane. Furthermore, the MOIs are updated throughout the simulation when transitioning from detumbling mode to fine pointing mode.

The two matrices A and Q are critical to the initial estimate result. The matrix A depends on an accurate system model, and matrix Q depends on an appropriate estimate of the process noise. Otherwise, the filter's estimate will deviate from the true value.
The numerical results and discussion will be presented in the following chapter.

Chapter 5

Results and Discussion

The control method and Simulink blocks were discussed in Chapter 3, and the EKF algorithm was elaborated in Chapter 4. This chapter starts with the implementation of control methods and their numerical simulation. The results will be presented while explaining the functionality of controllers. The best scenario in terms of power management and attitude angle error is spending 1 orbit in detumbling mode. Then a check on the residual angular rates would be done. The solar panels would deploy if the body rates were less or equal to $0.5\ deg/s/axis$. In the next level, the CubeSat starts spinning up for 2 orbits with high gains. After that, the controller would switch to a low-gain PD controller. Fig. 5.1 shows a simplified functional flow diagram.

In the following, first, the detumbling simulation will be presented. Second, the fine pointing controller and the gain scheduling technique will be discussed. Third, the offline EKF algorithm is tested, and the plots will be shown and examined. Finally, the Simulink model tests the full integrated simulation. The final model starts with the detumbling phase, followed by fine pointing and includes the real-time embedded EKF algorithm to monitor the improvement of attitude control. Finally, the power worst case will be discussed.

To avoid duplication of simulation properties in each section, Table 5.1 lists common items in all simulations.

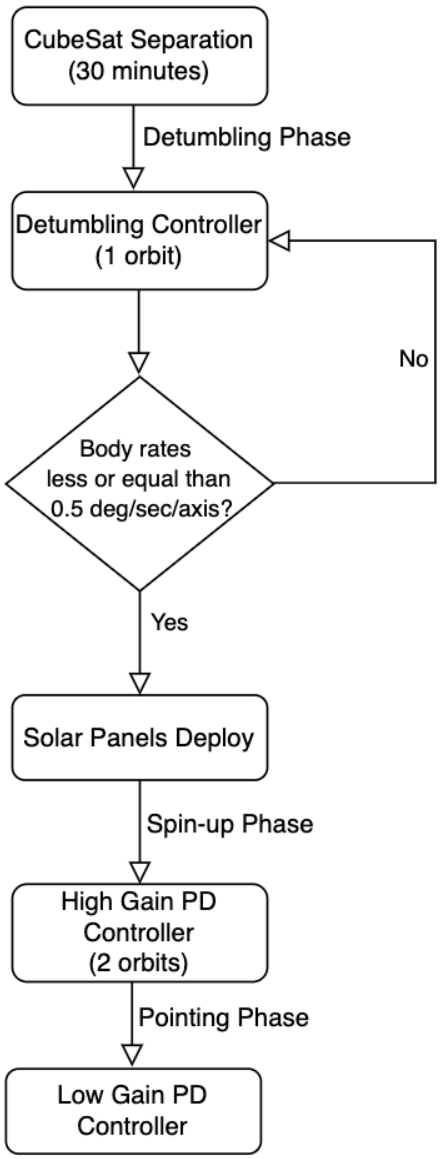


Figure 5.1: ADCS Algorithm Functional Flow Block Diagram

Time step	$0.1(\text{sec})$
Simulink integrator	$ode4(Runge-Kutta)$
Detumbling orbits	$1\ orbit$
Spin-up orbits	$2\ orbits$
Principal MOI in detumbling	$diag([3.57; 3.61; 0.74]) * (10^{-}2)(\text{kg.m}^2)$
Principal MOI in fine pointing mode	$diag([4.55; 4.36; 1.28]) * (10^{-}2)(\text{kg.m}^2)$
Residual Magentic Dipole	$[0; 0; 0.001]\ (\text{A.m}^2)$
Magnetometer noise	σ = 0.4 e-7 (T)
Dynamic uncertainties (process noise)	White noise σ= 1.2923e-08 per axis (N.m)
Simulation time for fine pointing control	$15\ orbits$
Detumbling Controller gain	6000
First controller proportional gain	$6e-5$
First controller derivative gain	$3e-1$
Second controller proportional gain	$9e-7$
Second controller derivative gain	$1e-3$
EKF-based controller proportional gain	$1e-8$
EKF-based controller derivative gain	$1e-3$

Table 5.1: Common properties used in all simulations

Regrading Table 5.1, the time step is always $0.1\ sec$, which grants a frequency of $10\ Hz$ to the controller and the sensors. All simulations include dynamic uncertainties and unknown perturbations, simulated as Gaussian white noise added to the gravity gradient and residual dipole torque.

In the following, the active magnetic attitude control system time-response with respect to the detumbling and PD controller is analyzed.

5.1 Detumbling Controller Analysis

Detumbling mode initiates with the initial value of $[5, 5, 5]\ deg/sec$ body rate as the worst case. The ADC subsystem requirement indicates the angular velocity on each axis shall be reduced to $0.5\ deg/sec$ or less before deploying the antenna and solar arrays. During the simulations, it was concluded that the number of detumbling orbits significantly affects the control of the following fine pointing state, which will be discussed in Section 5.4. The following will demonstrate and discuss the 1 orbit detumbling results.

5.1.1 1 Orbit Detumbling

In the presence of external perturbation and dynamic uncertainties, the following results are obtained when the detumbling controller runs in the first orbit.

The body rates, as seen in Fig. 5.2 successfully show a body rate damping from the initial value of $[5, 5, 5]\ deg/sec$.

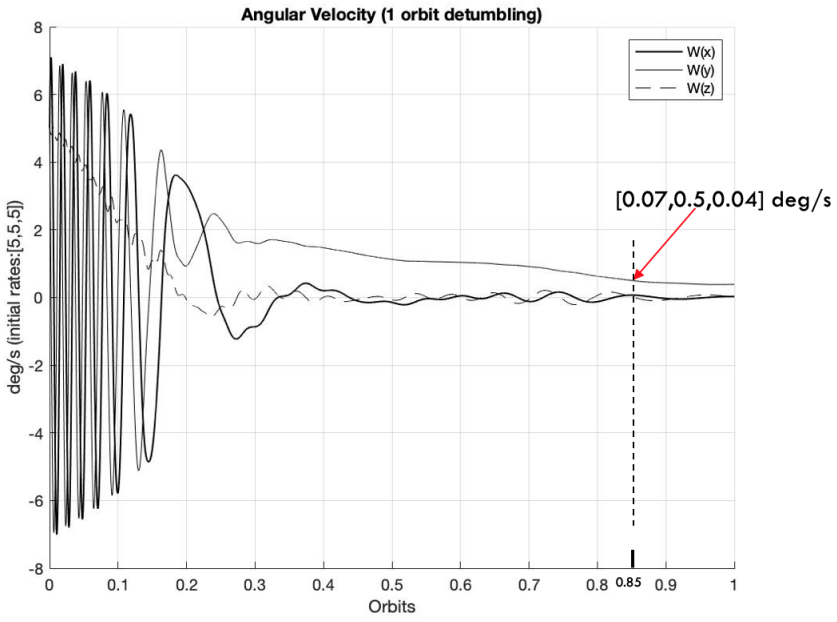
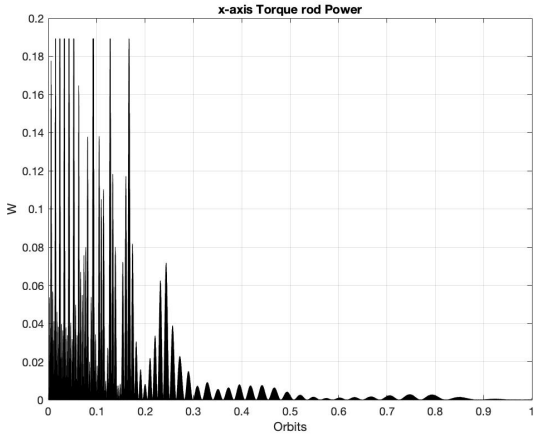


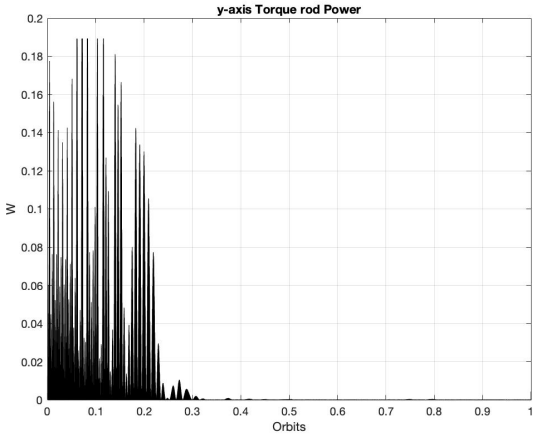
Figure 5.2: Body rates of Iris during detumbling with initial angular velocity of $[5, 5, 5]\ deg/sec$ after 1 orbit

The y-axis is the major axis with the maximum moment of inertia as stated in equation 3.45. Therefore, the w_y takes longer to decay, and the intermediate and minor axis take less to track near-zero angular velocity.

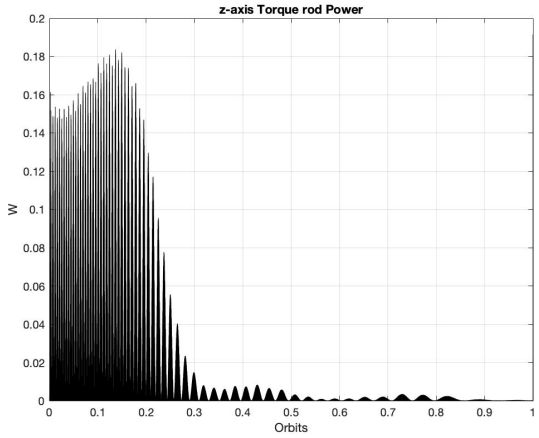
Figure 5.3 shows the torque rods that are mostly active during the first 0.2 orbit and then the power consumption is reduced considerably as the body rates are damped and the angular velocity is tracking $0\ deg/sec$ on all three axes. As seen, the torque rods are prevented from saturating simultaneously.



(a) Torque rod power on x-axis



(b) Torque rod power on y-axis



(c) Torque rod power on z-axis

Figure 5.3: Torque rod power consumption of satellite during detumbling with initial angular velocity of $[5, 5, 5]$ deg/sec after 1 orbit

Figure 5.4 shows the magnetic field in the body frame which is changing rapidly while the CubeSat is spinning.

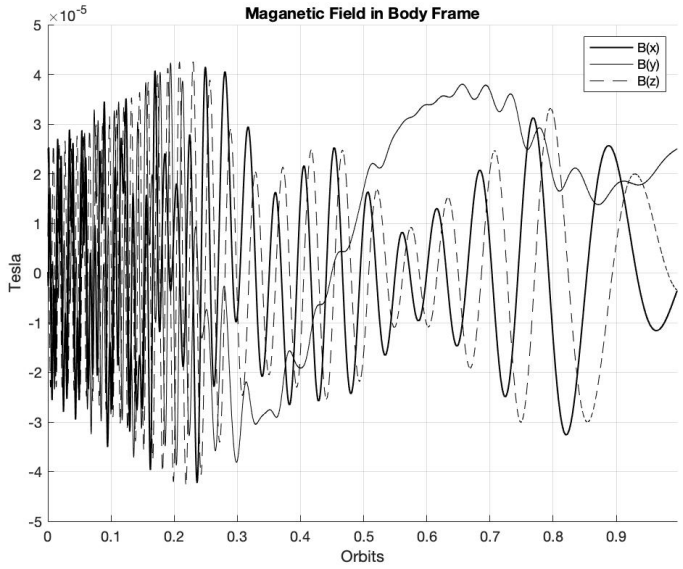


Figure 5.4: Noisy measurements of the magnetic Field ($\vec{B}$) strength in the body frame during the first orbit while detumbling measured by the magnetometers

For the purpose of comparison, 5 different initial values for detumbling has been considered. Below the summary of detumbling simulations is presented. The $0.5\ deg/sec$ settling time refers to the condition when the body rates of all axis fall below $0.5\ deg/sec$ but not necessarily simultaneously.

Summary (Detumbling)		
Initial Body Rate	Steady State Body Rate	0.5 deg/sec settling time
[5,5,5]	[0.028,0.38,0.011] deg/sec	0.85 orbit
[-5,-5,-5]	[0.013,-0.21,0.004] deg/sec	0.77 orbit
[0,0,5]	[0.04,-0.09,-0.08] deg/sec	0.26 orbit
[5,0,5]	[0.085,0.176,0.0915] deg/sec	0.72 orbit
[0,0,-5]	[0.073,-0.019,0.0425] deg/sec	0.26 orbit

Table 5.2: Detumbling Simulation Summary for various initial body rates

The worst-case detumbling as seen in Table. 5.2 results from the initial body rate of $[5, 5, 5]\ deg/sec/axis$, which takes 0.85 of the orbit to reduce body rates on all axis to below $0.5\ deg/sec$. As seen in

Table. 5.2 the satellite is detumbled within the first orbit, and the residual body rates are below the ADC subsystem requirements in order to deploy the solar panels and the antenna.

5.2 Fine Pointing

In this section, the fine pointing phase in the simulation is investigated. The simulations start with an initial body rate of $0.5\ deg/s$ on each axis. This requirement for stopping detumble can be considered the worst-case scenario for deploying the solar arrays. Figure 5.5 shows the result of numerical simulation regarding the satellite's body rates. EKF-based control is not considered in the eclipse, so there is no control during the eclipse, and the torque rods are not operating.

In the beginning, the satellite starts spinning with high rates about all 3 axes. After 2 orbits spinning with high PD gains, the proposed method damps the excess body rate and tracks the desired $[1, 0, 0]$ sun position vector.

With a reference to Fig. 5.6 the steady-state body rates are $[0.998, 4.5e-3, -1e-3]\ deg/sec$ after 15 orbits.

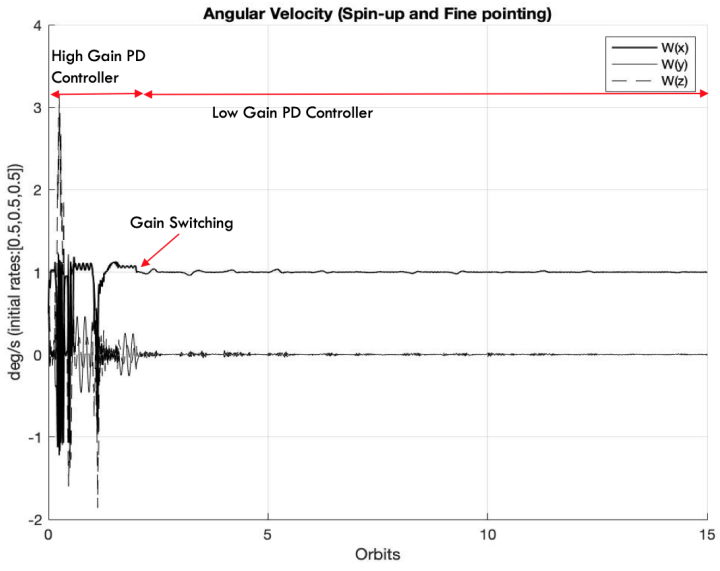


Figure 5.5: Body rates of Iris during fine pointing with initial angular velocity of $[0.5, 0.5, 0.5]\ deg/sec$ after 15 orbits

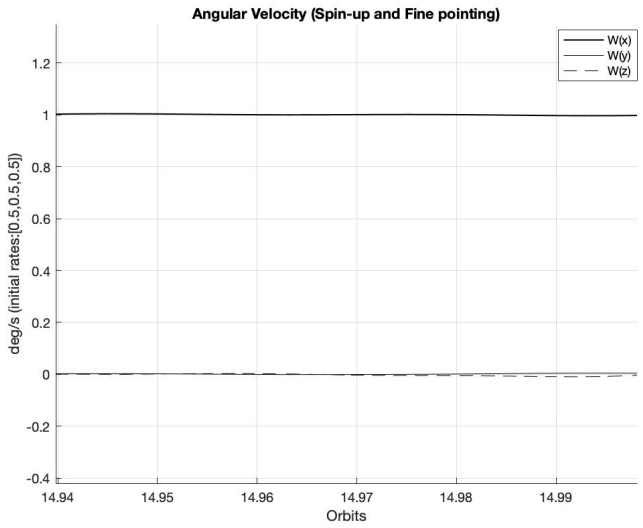


Figure 5.6: Close up view of residual body rates of Iris during fine pointing with initial angular velocity of $[0.5, 0.5, 0.5]$ deg/sec after 15 orbits

The fine pointing scenario starts with 2 orbits of high-gain spin stabilization, which allows for alignment of the satellite's $-x$ reference axis with the sun. After that, the low-gain PD controller reduces the pointing error to 1 deg as seen in Figures. 5.7 and 5.8. The pointing angle plot is seen in Fig. 5.9 which shows the promising result of providing the required pointing of ± 21 after six orbits.

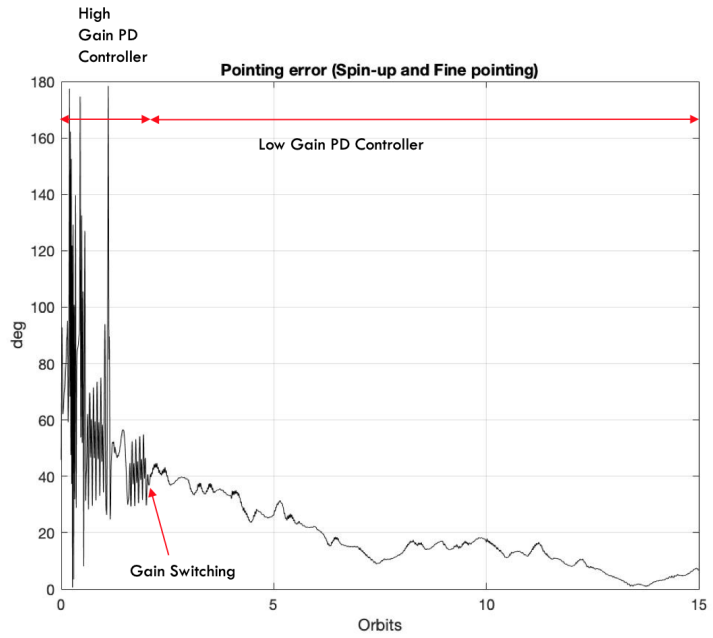


Figure 5.7: Attitude angle of satellite during fine pointing with initial angular velocity of $[0.5, 0.5, 0.5]$ deg/sec including all perturbation after 15 orbits

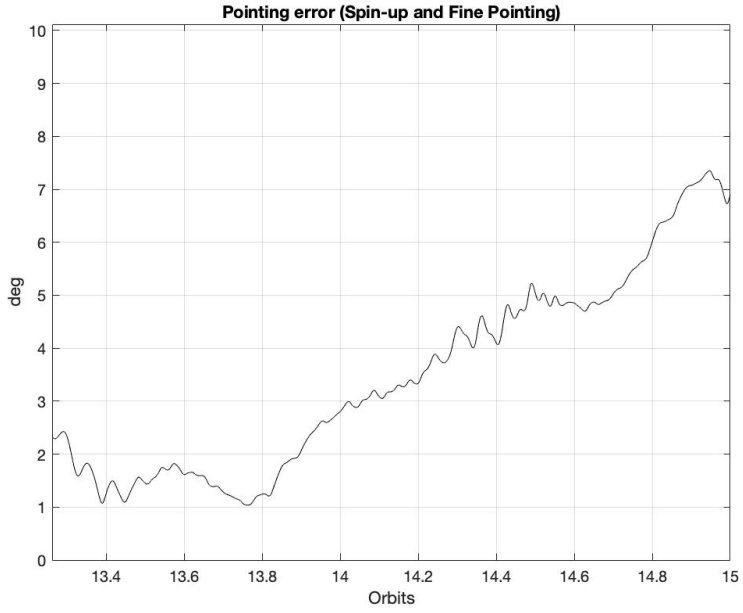


Figure 5.8: A close up view of attitude angle of satellite during fine pointing with initial angular velocity of $[0.5, 0.5, 0.5]$ deg/sec with all perturbation after 15 orbits

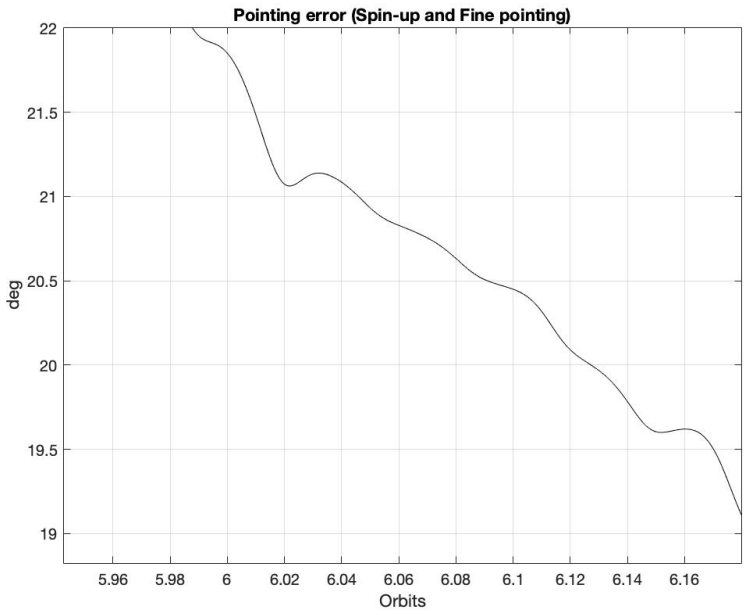
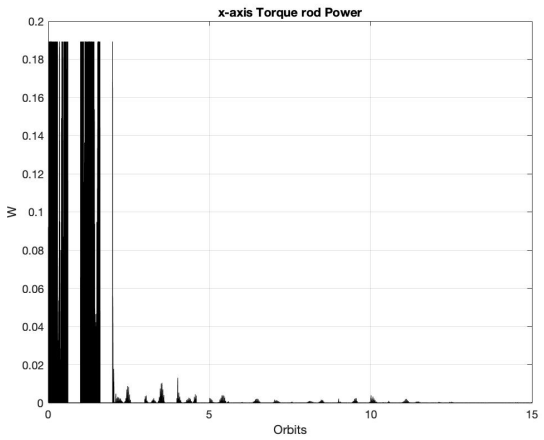
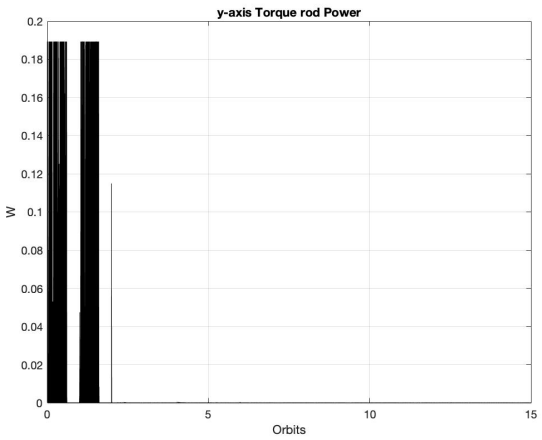


Figure 5.9: A close up view of attitude angle of satellite at 6th orbit during fine pointing with initial angular velocity of $[0.5, 0.5, 0.5]$ deg/sec when the pointing accuracy enters the 21 deg window

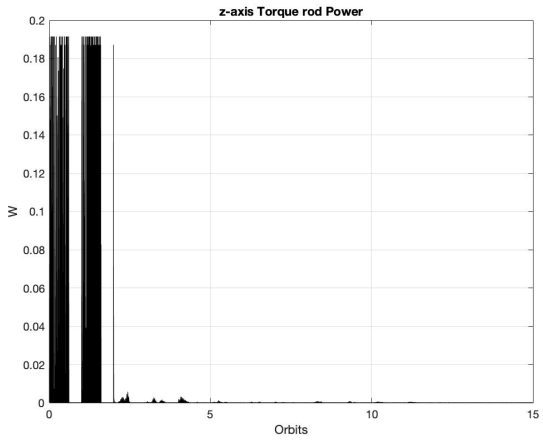
The torque rods show active power usage during the high-gain spin, as seen in Fig. 5.10. The scenario reduces the total power consumption of the magnetorquers as the torque rods are in full power while damping excess body rates and tracking the desired one. Afterwards, the CubeSat benefits from the gyric stiffness to maintain stability, and the power consumption converges to almost zero.



(a) Torque rod power on x-axis



(b) Torque rod power on y-axis



(c) Torque rod power on z-axis

Figure 5.10: Torque rod power consumption of satellite during fine pointing with initial angular velocity of $[0.5, 0.5, 0.5]$ deg/sec with all perturbation after 15 orbits and power management strategy

5.3 Extended Kalman Filter Approach for State Estimation

The sun sensors cannot measure the sun's position in the eclipse. Therefore the sun vector is estimated with the help of body rates. Iris will be in eclipse for each orbit for 37 minutes, which is added to the simulation with a switch block. The launch date is unknown, so calculating the exact eclipse start time is impossible. For this reason, the simulation starts with the illumination phase and then proceeds to the eclipse.

5.3.1 Measurement Noise

In the Iris mission, the EKF algorithm employs actual sensors (magnetometer, sun sensor, gyroscope) noise from data sheet. The table below presents the measurement noise used in the simulation.

Summary (Sensor noise in EKF)		
Sensor	Noise Value	Frequency Value
Gyroscope	σ = [4.089;4.089;4.089] e-3 (rad/sec)	10 (Hz)
Sun sensor	σ = 3.33 e-6 (m)	10 (Hz)
Magnetometer	σ = 0.4 e-7 (T)	10 (Hz)

Table 5.3: Sensor's properties used in EKF simulation

Gyroscope noise density regarding the data-sheet is $0.03\ dps/\sqrt{Hz}$. Therefore the true noise can be written as below:

$$True\ noise = (0.03 \times \frac{pi}{180}) \times \sqrt{1.22 \times 50} = 4.089e-3$$

The $0.1\ deg$ sun sensor noise in the Iris mission corresponds to a $3.33e-6\ (m)$ deviation on the $y-z$ axis. In order to derive the error, a spin stabilized scenario was considered as the CubeSat is spinning with $[1,0,0]\ deg/sec$ and with $30\ deg$ attitude angle. The same procedure is repeated with the $29.9\ deg$ angle, and the subtraction of the two values on the y axis is considered the sun sensor noise.

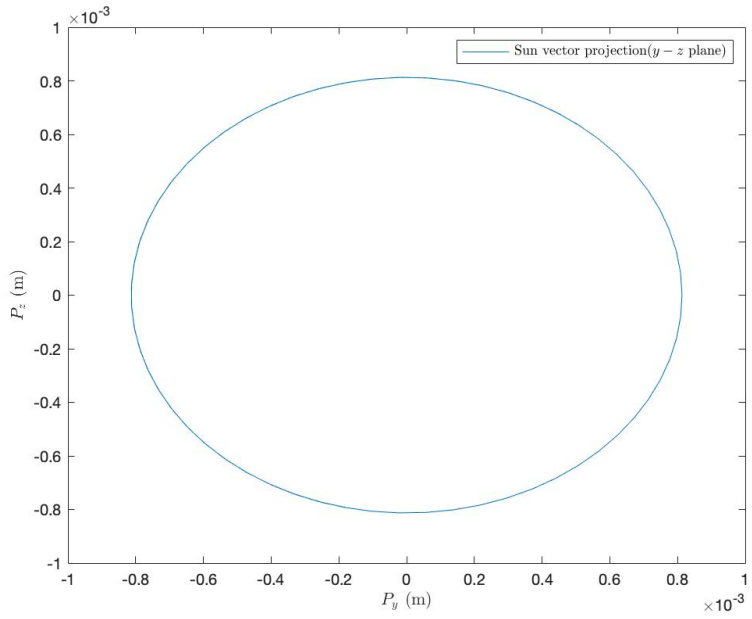


Figure 5.11: Sun vector Projection on $y-z$ plane while the sun pointing CubeSat is spinning with $[1,0,0]\ deg/sec$

5.3.2 Process Noise

There is no straightforward method to detect the process noise (q). Modelling approximation, unmodeled dynamics, model linearization, continuous and discrete model integration errors, and parameter uncertainties would be combined to shape the process noise in the state estimator, which are not easy to measure. Therefore, in this thesis I chose the process noise with trial and error to be $\sigma = 1.2923e-08\ per\ axis\ (N.m)$ which is added to the actual model in simulation.

In the estimator algorithm, when the diagonal elements of the process noise covariance matrix, Q, is decreased, the estimate will rely more on the dynamics, and will be affected less by the measurements. Similarly, by increasing the Q, more information for the estimation will be taken from the measurements.

In this system, by observing the error covariance bounds of the actual estimation error, the ω in equations 4.39 and 4.40 which form the continuous covariance matrix has been chosen as $1e-7\ per\ axis$ from the fourth orbit. As mentioned earlier the EKF is not operative during the

first three orbits (detumbling and the spin-up phase) by choosing a large process noise covariance matrix.

5.3.3 EKF including 2 sensors and 5 states

In this research, both the sun and gyroscope sensors' measurements are considered within the EKF algorithm. As mentioned before, all perturbation and unknown uncertainties are included in the simulation.

During detumbling and spin-up, the accuracy of attitude estimation is not essential as long as the satellite can dampen its body rate in detumbling and reach the desired state after spin-up. The results in fine pointing mode after the spin-up phase in the 4th orbit will be examined. Thus, this simulation conveys the adequate performance of the algorithm.

Below a summary of the steps done in the offline EKF simulation is presented:

- The actual sensors' measurements output are extracted from the Simulink model. The sensor's output in the simulation does not include the noise, but the control input torque consists of the process noise.
- The simulation is initialized with a guess as the starting point for the state vector.
- The nonlinear equations stated in equation 4.23 are integrated with the Runge-Kutta fourth-order method and then implemented in the EKF algorithm as the initial estimation, which propagates the states to the next time step.
- Sensor's noises are added to actual sensor output for measurements.
- The last step of the Kalman filter is to update the estimation of state variables with measurements input which will be the next initial point for the nonlinear propagator to start with.

In the following, the different components of the algorithm, including the real and estimated data and estimated uncertainty of state-space, have been displayed.

In Fig. 5.12 the estimated sun attitude vector is depicted against the actual data. After spin-up, the sun sensor measurements are propagated with low error, and the estimated states follow the actual values during the eclipse.

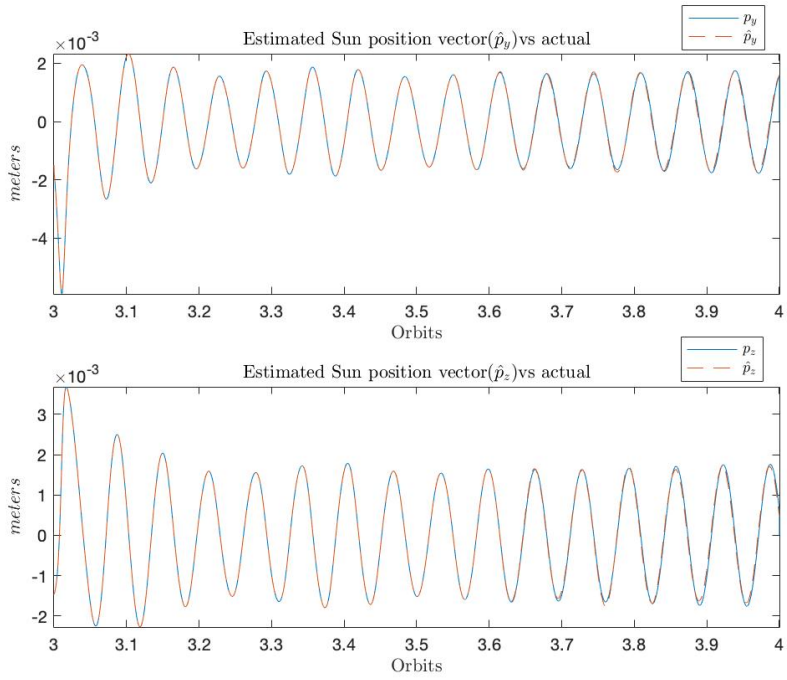


Figure 5.12: Estimated sun attitude vector projection vs sun sensor output within the 4th orbit

A magnified view of the eclipse moments is seen in Fig. 5.13. The actual error is displayed in Fig. 5.14. As seen, the error increases in the eclipse while the sun sensor's measurements are missing to the order of 10^{-4} and decreases in the illumination phase to the order of 10^{-6} as seen in Fig. 5.15.

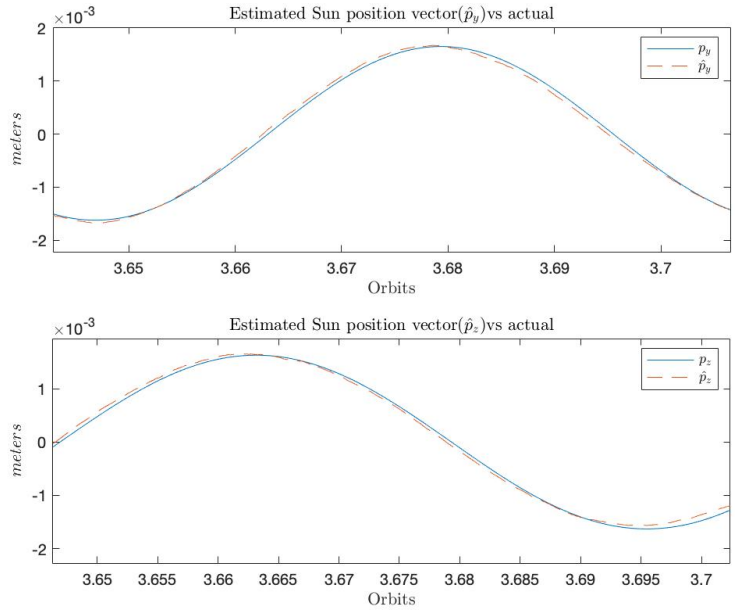


Figure 5.13: A close-up view of estimated sun attitude vector projection vs sun sensor output within the eclipse time of the 4th orbit

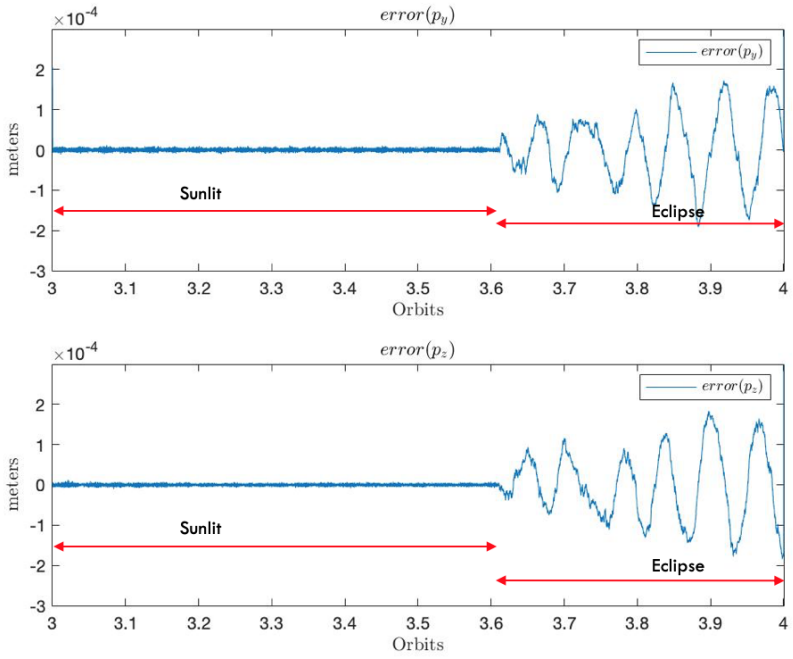


Figure 5.14: Estimation error of sun attitude vector projection within the 4th orbit

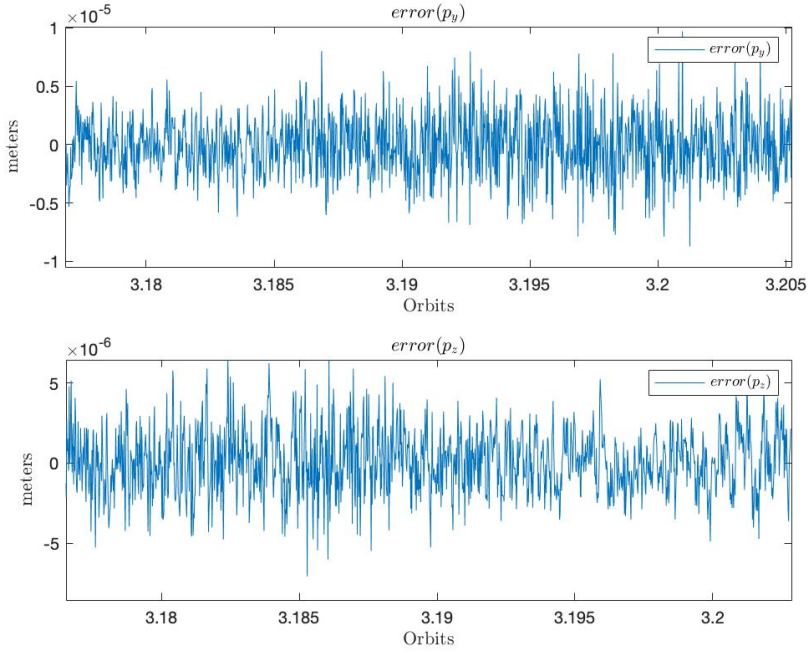


Figure 5.15: A close up view of estimation error of sun attitude vector projection within the illumination phase of the 4th orbit

Figure 5.16 shows the initialization of the EKF algorithm from the identity matrix. The estimated error reduces to the order of 10^{-9} and then rise again in eclipse to the order of 10^{-3} as shown in Fig. 5.17.

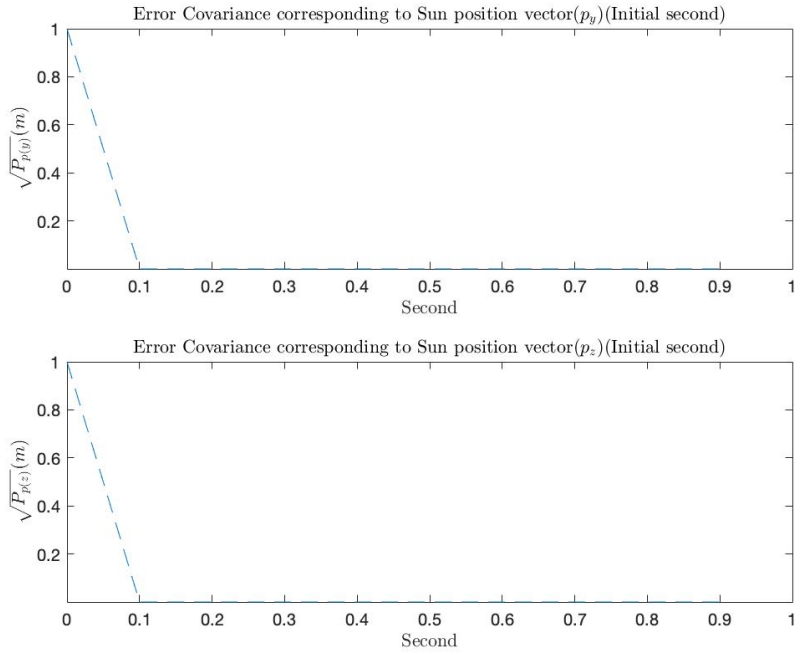


Figure 5.16: Square root of estimated error covariance matrix corresponding to sun vector projection during the 1st second

The sun attitude feedback is unavailable during the eclipse, as seen in Fig. 5.17. The dashed line, which is the square root of the covariance estimate, rises in eclipse. Figure 5.17 shows that the error covariance should bound the estimation error. The 1σ bounds are directly calculated from the error covariance matrix as they are the square root of the diagonal elements. In the eclipse of fourth orbit, error spikes reach up to 31 (deg) however the mean estimation error would be $0.035\ (deg)$ and the standard deviation is 6.39(deg). The spikes in attitude angle takes almost 12 orbits to reach estimation error less than 2.44(deg).

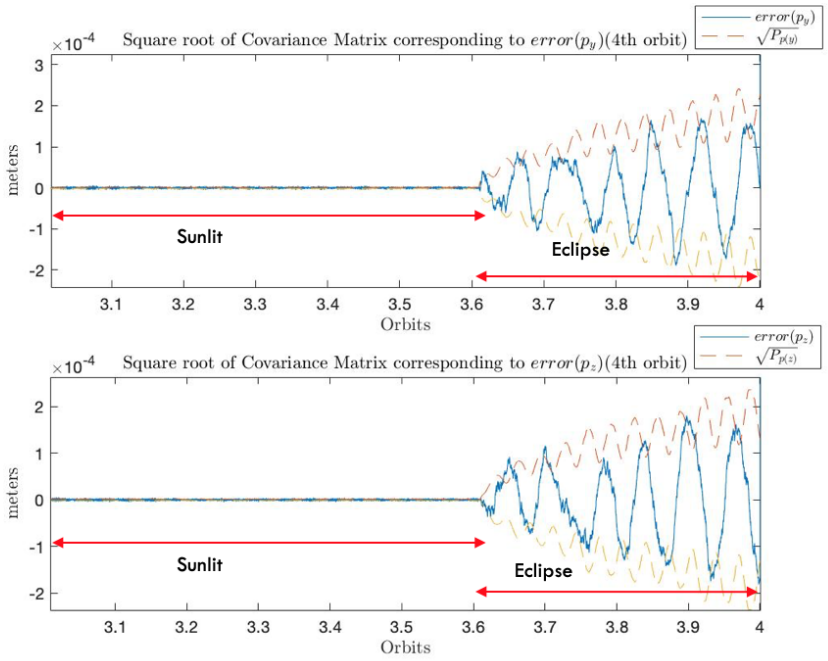


Figure 5.17: Square root of error covariance matrix corresponding to estimation error of sun attitude vector projection on y and z axes in the 4th orbit

Having a closer look at some moments in the illumination phase of the fourth orbit, the estimation error is shown in solid blue lines, and the dashed red line is the square root of diagonal elements of the error covariance matrix (Figure 5.18). As seen, the actual error is well bounded by the estimated error, which shows the functionality of the EKF algorithm.

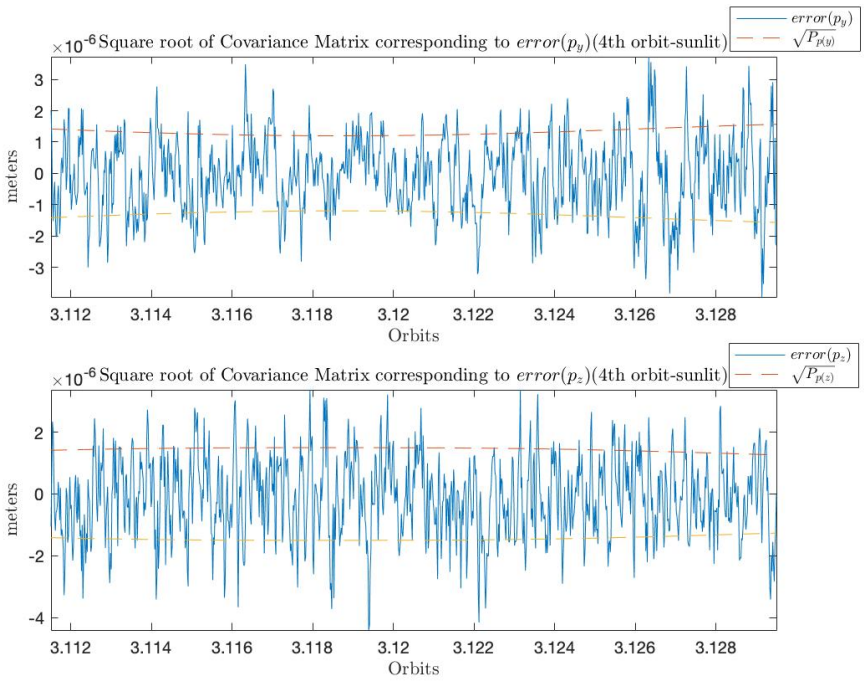


Figure 5.18: A close up view of estimation error of sun vector projection in y and z axes bounded by square root of the error covariance matrix in 4th orbit

The table below summarizes the sun vector estimation of the EKF algorithm.

Summary (error)			
State	Orbit No	Error in sunlit phase(std)	Error in eclipse (std)
$\begin{bmatrix} p_y \\ p_z \end{bmatrix}$	4	$\begin{bmatrix} 0.23\text{e-}5(m) \\ 0.22\text{e-}5(m) \end{bmatrix}$ or 0.1(deg)	$\begin{bmatrix} 0.16\text{e-}3(m) \\ 0.17\text{e-}3(m) \end{bmatrix}$ or 6.39(deg)
$\begin{bmatrix} p_y \\ p_z \end{bmatrix}$	12	$\begin{bmatrix} 0.91\text{e-}6(m) \\ 0.85\text{e-}6(m) \end{bmatrix}$ or 0.06(deg)	$\begin{bmatrix} 0.37\text{e-}4(m) \\ 0.37\text{e-}4(m) \end{bmatrix}$ or 2(deg)

Table 5.4: EKF Estimation Error Summary

As mentioned before, the system state matrix included five variables. Two are the sun attitude vector projection interpreted as the two-axis sun sensor outputs, and three other states are the angular velocity in the body frame.

As seen in Fig. 5.19, the actual and estimated angular velocity are plotted. Since the measurements are fed into the system, the EKF algorithm can precisely track the actual body rates within the scenario. As such, In Fig. 5.21, the estimation error of body rates is almost constant throughout the scenario. Additionally, Fig. 5.20 provides a magnified view of the noisy estimated

body rates against the actual data.

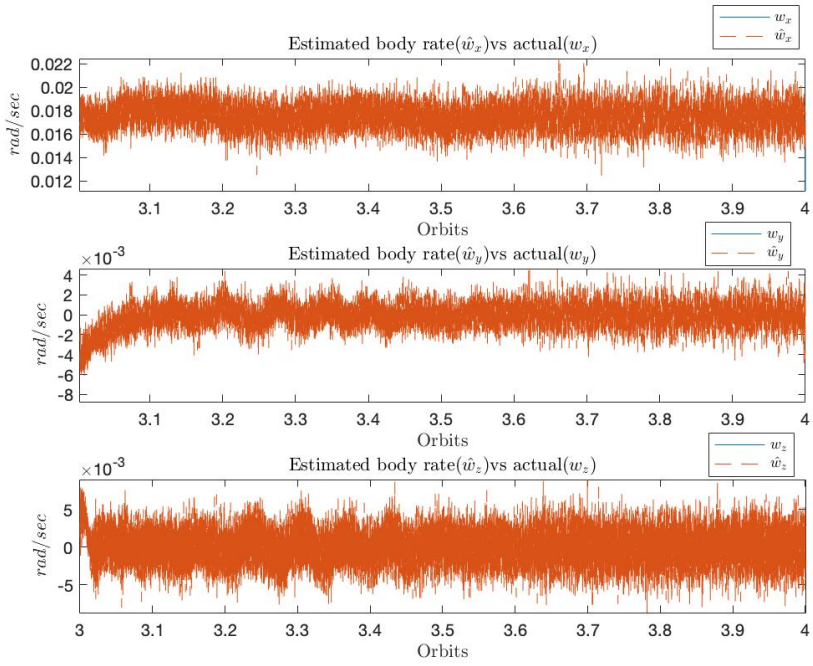


Figure 5.19: Estimated body rates vs the actual data during the 4th orbit (after spin-up)

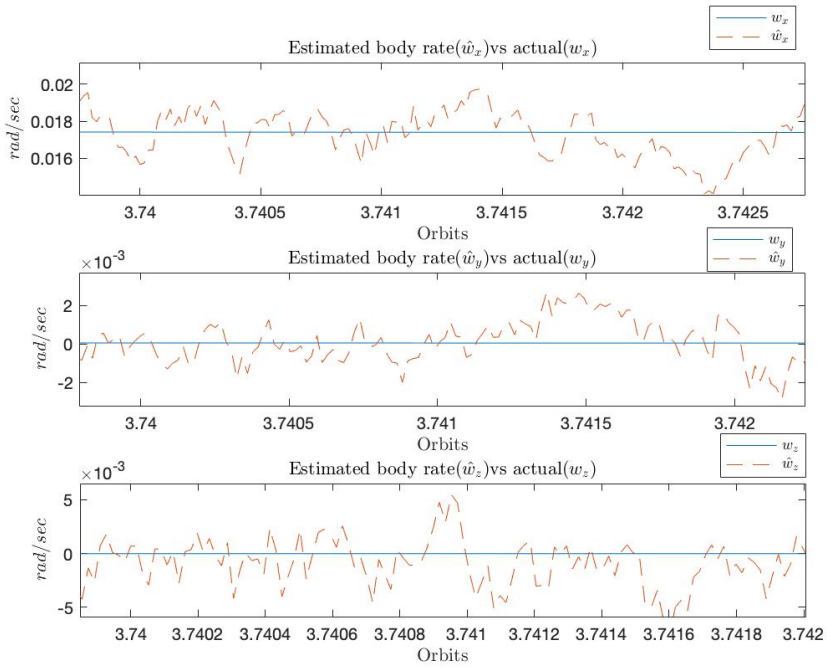


Figure 5.20: A close up view of the estimated body rates vs the actual data during the 4th orbit (after spin-up)

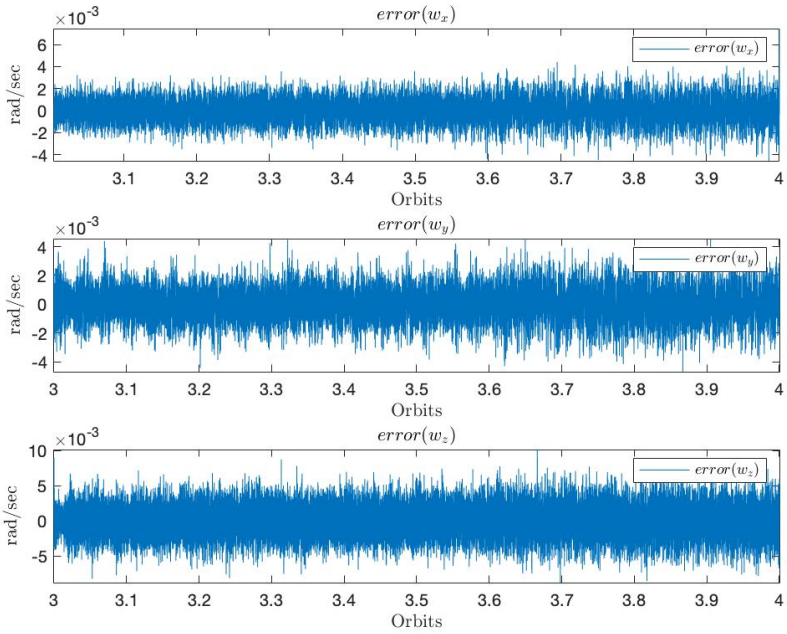


Figure 5.21: Estimation error of body rates during the 4th orbit (after spin-up)

As seen in Fig. 5.22, the EKF algorithm initiates with an identity matrix for the covariance matrix. In the subsequent iterations, the estimated error covariance reduces to the order of 10^{-9}.

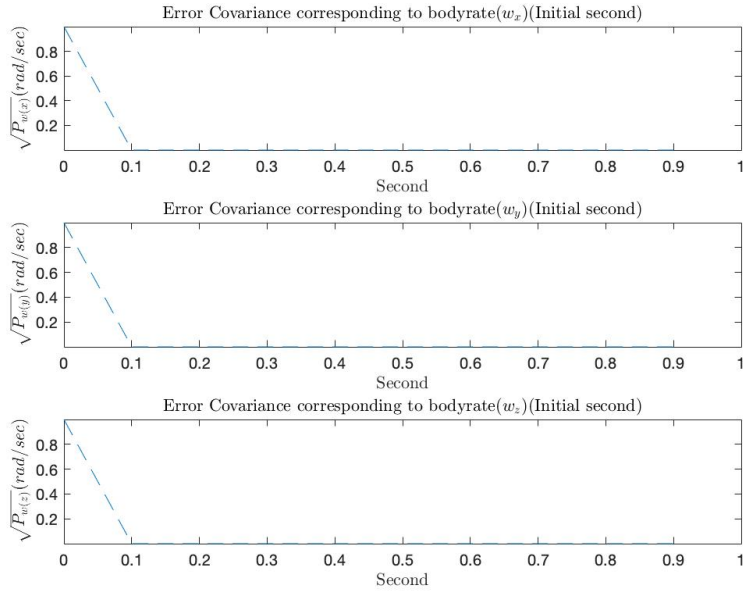


Figure 5.22: Square root of error covariance matrix corresponding to body rates during the 1st second

The estimation error was shown previously. Finally, both square root of the covariance matrix and estimation error are drawn on the same plot in Fig. 5.23. The actual error for body rate estimation is well-bounded by the square root of the estimated error covariance. As a result, it can be concluded that the algorithm works properly and the results are reliable.

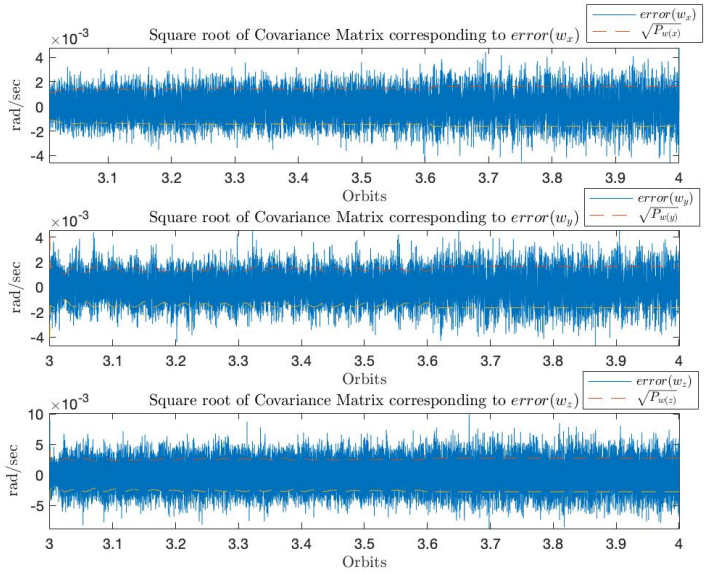


Figure 5.23: Estimation error of body rates bounded by the square root of error covariance matrix within 4th orbit

To sum up, the results of the offline implementation of the EKF algorithm with gyroscopes and sun sensors are shown in the section above. After detumbling and spin stabilization, the EKF algorithm can estimate the sun position vector with a low error. This algorithm has been tested solely with the simulated sensor's data extracted from Simulink to prove the algorithm's functionality.

5.4 Attitude Control of Satellite with Power Management Strategy

In order to provide the appropriate pointing with the desired spin rate and minimum magnetorquer power consumption, two spin stabilization controllers are used. Both controllers are in the

form of PD controllers. The first controller (high-gain controller) spins up the satellite to the desired spin rate of $[1, 0, 0]\ deg/sec$ until the satellite gains gyric stiffness. Then the first controller would switch to the second controller with lower gains. Low gains cause the actuators to use less power. The gains have been tuned by trial and error method.

In Table 5.5 the summary of simulations in terms of the number of orbits chosen is presented. All simulations include all perturbations and dynamic uncertainties.

Summary (Detumbling-Spin orbits)				
Scenario	No of Detumbling Orbits	No of Spinup orbits	Fine pointing accuracy without EKF(deg)	Fine pointing accuracy with EKF(deg)
1	1	1	± 6.1	± 5.8
2	1	2	± 4	± 0.18

Table 5.5: Detumbling-Spin Simulation Summary

In scenario 1, when the spin-up PD controller runs for one orbit, the steady-state attitude angle after 15 orbits with zero control in eclipse is about 6.1 degrees. When an EKF-based PD controller is used in eclipse, the accuracy reaches $5.8\ deg$. However, as seen in Table 5.5 if the spin-up controller runs for two orbits as in scenario 2, better pointing accuracy is obtained. That's why the design choice for applying the gain scheduling technique is 1 orbit detumbling followed by 2 orbits spin-up.

5.5 Real time EKF-based attitude feedback in Simulink

The EKF algorithm has been embedded in Simulink and provides the controller block in eclipse with the satellite's attitude. Since the detumbling controller does not require the pointing vector and the spin-up process is a transient state, the estimator is worth analyzing after this time. Regarding Fig. 5.5 it's feasible to start the EKF-based attitude feedback from the fourth orbit. The proportional and derivative gains of the EKF-based PD controller are presented in Table. 5.1.

Below a summary of the EKF simulation steps in the third scenario is presented:

- As seen in Fig. 3.14, the EKF block includes inputs (noisy measurements and actuator's torque) and output of estimated states.
- The actual noisy sensor's measurements directly enter the EKF block. Additionally, the actuator's torque includes the process noise.
- The simulation is initialized with actual data (without sensor's noise) as the starting point for the state vector.
- The nonlinear equations stated in equation 4.23 are integrated with the Runge-Kutta fourth-order method and then used in the EKF algorithm as the priori estimate, which propagates the states to the next time step without sensor noise.
- The last step of the Kalman filter is to calculate the estimate of state variables which will be the next initial point for the nonlinear propagator to start with.
- The final attitude estimate would then be used as feedback into the controller's block during the eclipse (after 3rd orbit).

As shown in Fig. 5.24, the attitude accuracy has been improved. Without EKF, a $4\,deg$ pointing accuracy is achievable at best. However, the EKF improved the accuracy to $0.18\,deg$ as seen in Fig. 5.25. Therefore, using the EKF in the eclipse enhances the control.

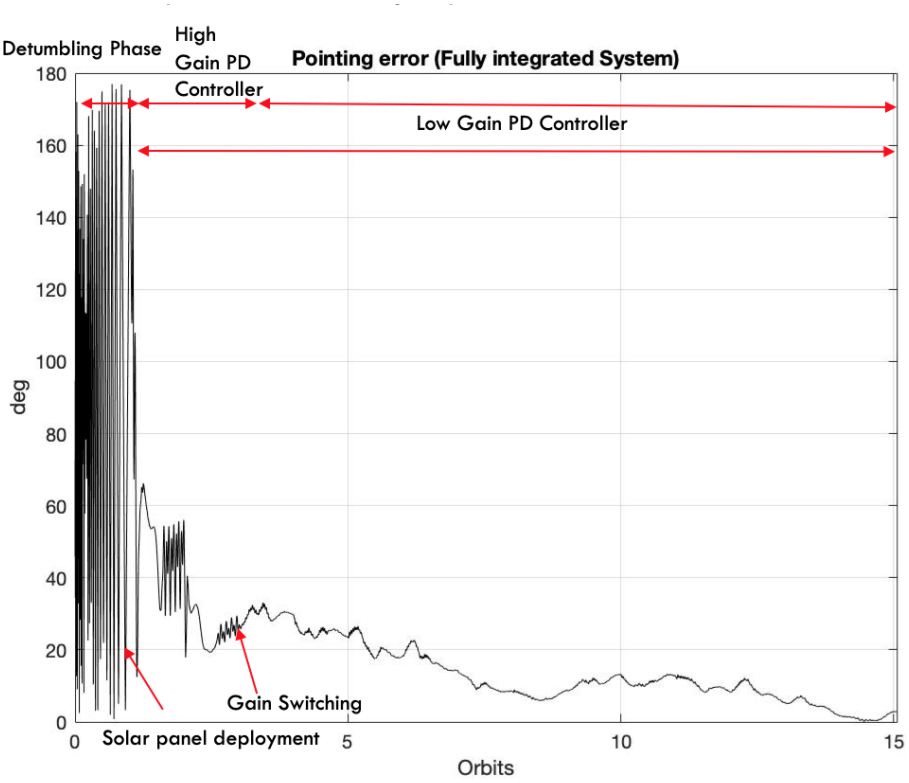


Figure 5.24: Pointing error during detumbling and spin stabilization with initial angular velocity of $[5, 5, 5]$ deg/sec within 15 orbits with real time EKF-based attitude feedback from 4th orbit

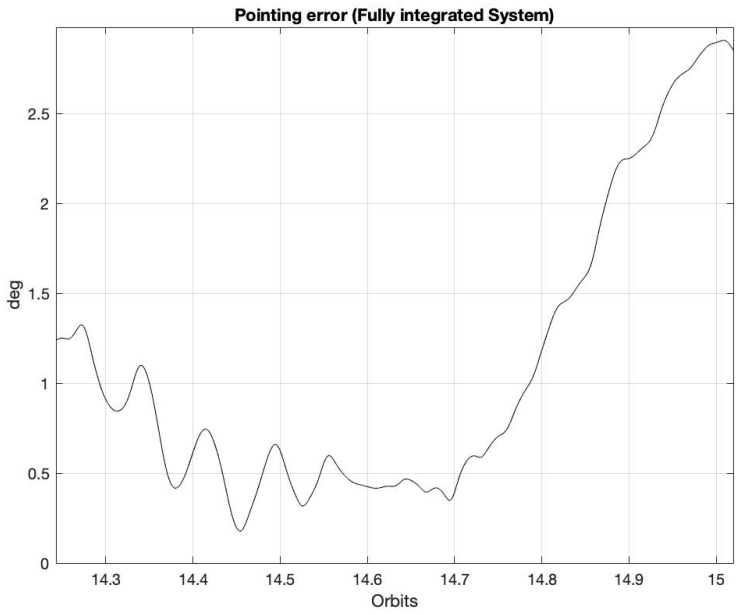


Figure 5.25: A close up view of pointing error during spin stabilization with initial angular velocity of $[5, 5, 5]$ deg/sec after 15 orbits with real time EKF-based attitude feedback from 3rd orbit

Figure 5.26 shows the body rates which are smoothly tracking the $[1, 0, 0]$ deg/sec target. It represents the effectiveness of the controller and EKF algorithm.

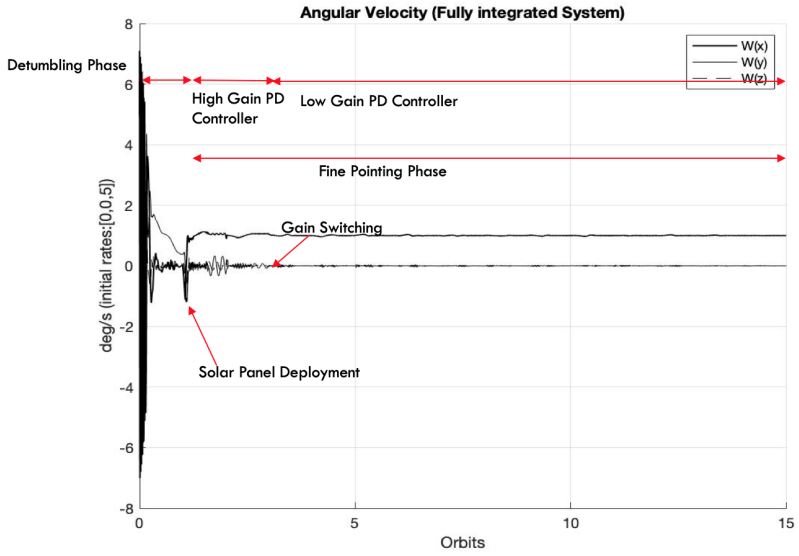
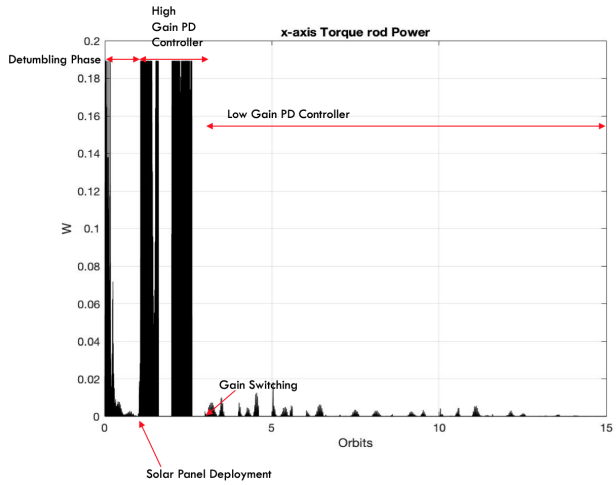
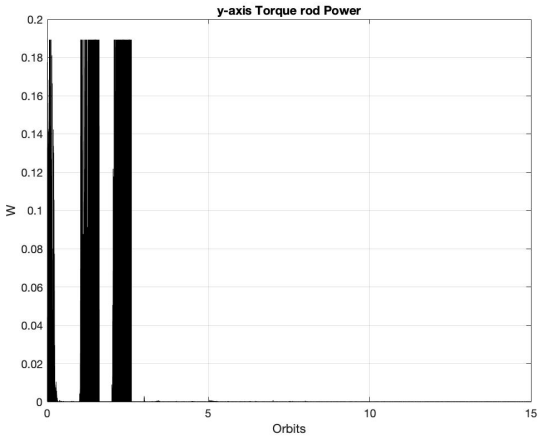


Figure 5.26: Body rates during detumbling and spin stabilization with initial values of $[5, 5, 5]$ deg/sec within 15 orbits with real time EKF-based attitude feedback from 4th orbit

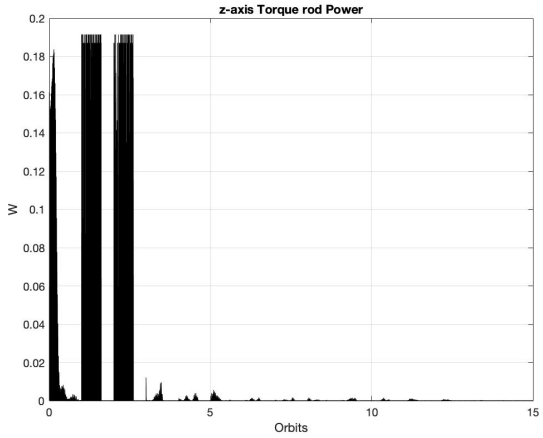
Figure 5.27 shows the magnetorquers effort. Although the EKF-feedback attitude has been added after the third orbit and the magnetorquers are operative throughout the illumination and eclipse phase, the power consumption hasn't increased.



(a) Torque rod power on x-axis



(b) Torque rod power on y-axis



(c) Torque rod power on z-axis

Figure 5.27: Torque rod power consumption of satellite with initial angular velocity of $[5, 5, 5]$ deg/sec with all perturbations after 15 orbits with real time EKF-based attitude feedback and power management strategy

While in eclipse, the attitude feedback is provided by the EKF block. Therefore, the torque rods are active during the eclipse. Although the PD gains provide a small control effort, the EKF-based feedback results in better control and pointing accuracy.

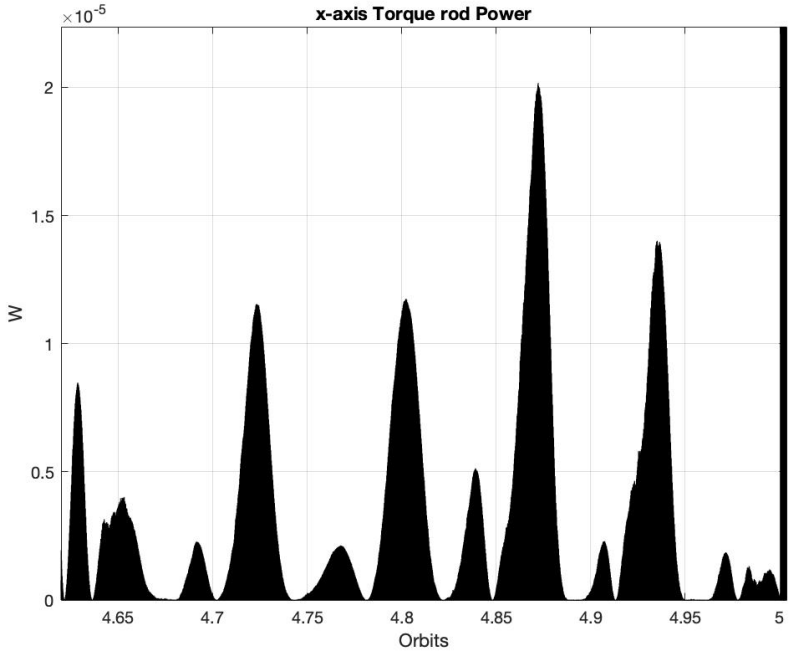


Figure 5.28: A close-up view of torque rod power consumption on x-axis during the eclipse of fourth orbit with real-time EKF-based attitude feedback

In the Fig. 5.29, the batteries will be fully charged within three orbits. During the solar panel deployment, the solar panels on the z axis would not generate any power and will be relocated to a new position that is normal to the $-x$ axis. This will cause a drop in SOC initially, but while the satellite is spinning up and the body rates are tracking the $[1, 0, 0]$ deg/sec, the charge current and consequently the SOC would increase.

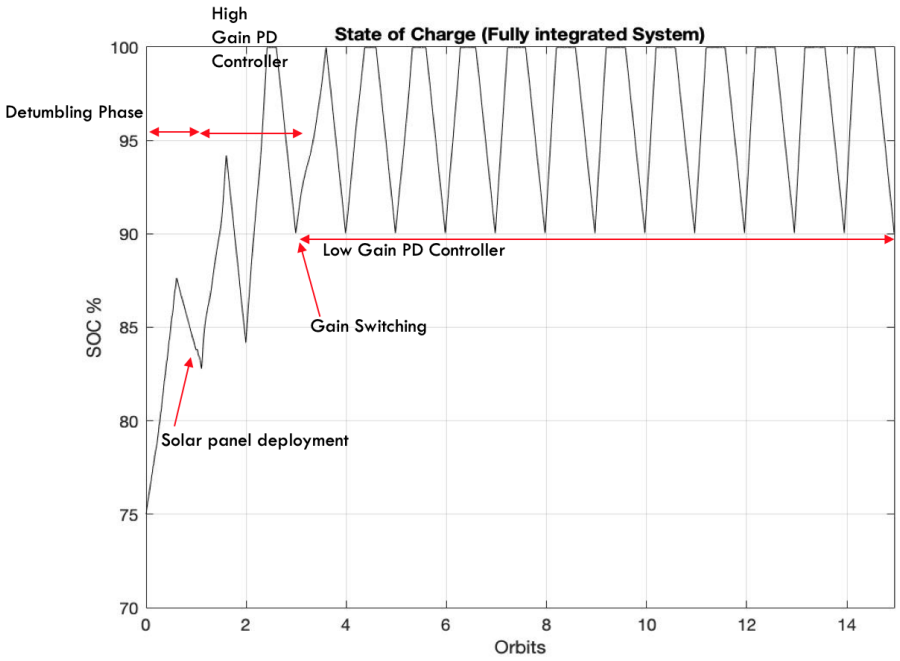


Figure 5.29: State of charge during detumbling and spin stabilization with initial angular velocity of $[5, 5, 5]$ deg/sec within 15 orbits with real time EKF-based attitude feedback from 4th orbit

5.6 Worst Power Generation Scenario

The SOC of the satellite should be kept within the range of more than $\%40$ in order to prevent low power mode. The power subsystem consists of 7 solar arrays and six Lithium Iron Phosphate (LiFePO4) batteries which collect solar energy [50]. The generated power will then be transferred to the spacecraft battery pack, eventually shown as the state of charge (SOC).

If the sun attitude is not maintained or the satellite is in the eclipse, the batteries wouldn't charge, and the state of charge (SOC) would drop. Regarding the power subsystem requirements,

the Iris CubeSat has only 4 orbits to detumble [50].

As plotted in the following diagrams, the power worst case happens when the satellite starts tumbling with the $+y$-axis pointed towards the sun, and the initial angular velocity is $[0, -5, 0]\ deg/sec$. Tumbling about the major axis of y axis wouldn't generate any power since there are no solar arrays on the $\pm y$ face.

In order to compute the initial pointing quaternion of the spacecraft, the initial attitude of satellite have to be found. With the initial quaternion of $[0.857, -0.1474, 0, 0.3584]$ the initial sun attitude of the CubeSat would be redirected to $[0, 1, 0]$.

Similar to previous scenarios, in the power worst case scenario, the detumbling controller would run for an orbit, then the CubeSat would spin up for two orbits, and finally, the controller would switch to the lower gain controller. The results are plotted in the following.

Figure 5.30 demonstrates the power generation of the CubeSat. This scenario would initially generate no power since the solar cells are not exposed to the sun. Therefore the SOC drops during the detumbling mode. Comparing the results in Figures 5.30 and 5.29, correcting the initial position from $[0, 1, 0]$ pointing causes the spacecraft to need more time to orient the solar panels towards the sun. So, in this case, the SOC is less than $\%60$ during three orbits (orbits $1 - 4$) and less than $\%50$ during one orbit but never passes the $\%40$ threshold. Additionally, a discontinuity in battery current or SOC rate is seen in Fig. 5.31 after the first orbit when the body rates dampened, and the solar panels are deployed. Compared to the normal scenario depicted in Fig. 5.29, this case can be considered the worst-case scenario.

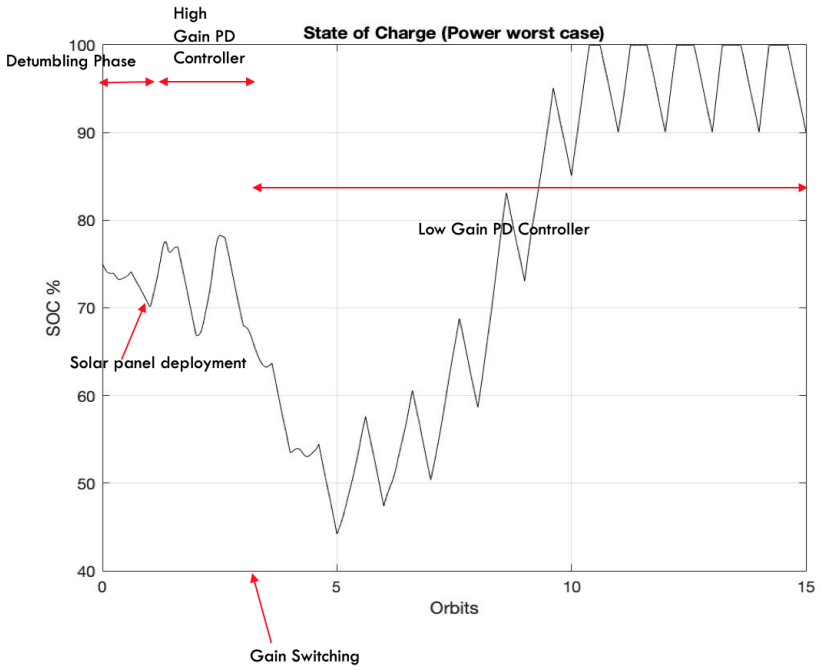


Figure 5.30: State of charge of the satellite during worst power scenario with an initial angular velocity of [0,-5,0]deg/sec

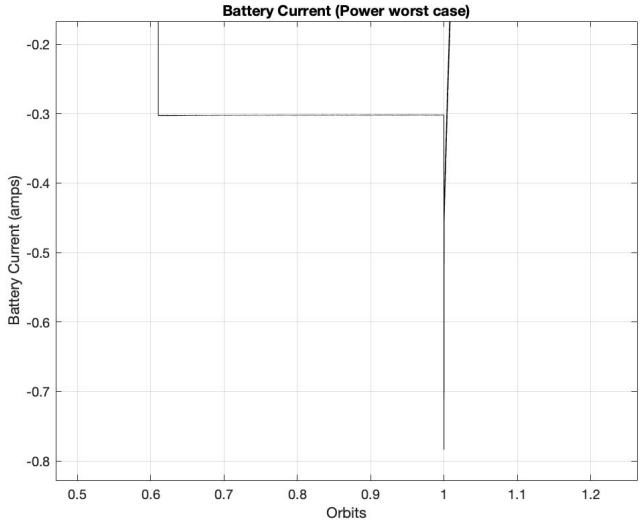


Figure 5.31: Discontinuity in the battery charge current (SOC rate) of the satellite during the solar panel deployments after detumbling (worst power scenario)

As shown in Fig. 5.32, the satellite is detumbled within one orbit. During the second orbit, the satellite is spinning up with the $[1, 0, 0]$ deg/sec rate, and the sun-pointing is lost. The satellite

gains gyric stiffness after 3 orbits.

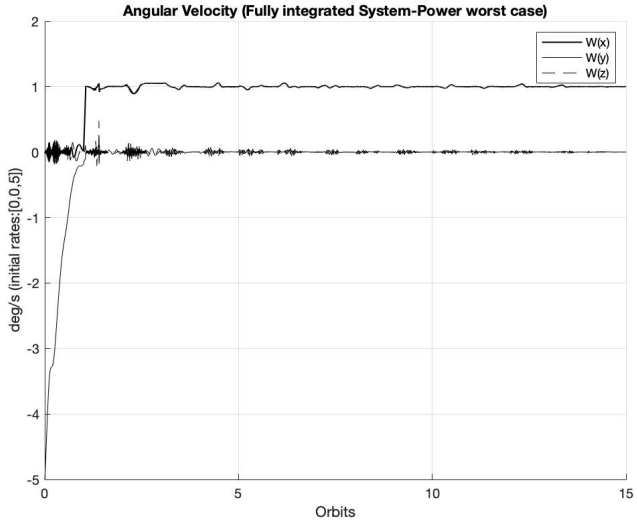


Figure 5.32: Body rates of the satellite during worst power scenario with an initial angular velocity of [0,-5,0]deg/sec

The attitude angle, as seen in Fig. 5.33 is out of range for more than 13 orbits, and the low-gain controller corrects the pointing gradually. A close-up view of the pointing error is shown in Fig. 5.34 which offers a promising accuracy of approximately $6\ deg$, which is well below the $21\ deg$ pointing accuracy requirement.

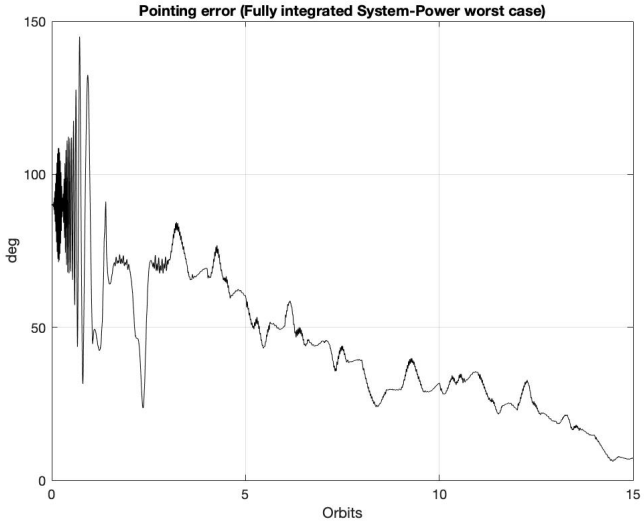


Figure 5.33: Attitude angle during worst power case scenario with initial angular velocity of [0,-5,0]deg/sec

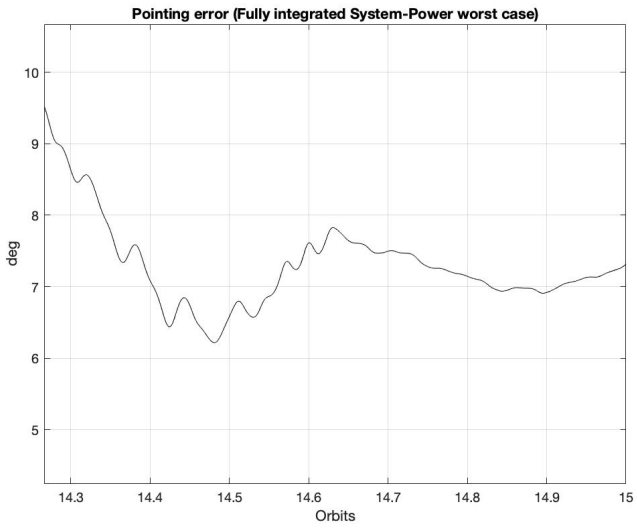
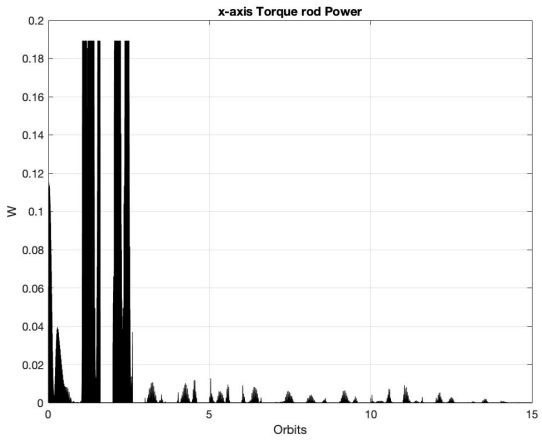
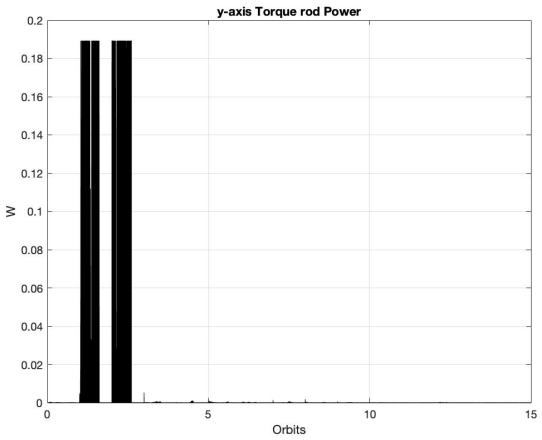


Figure 5.34: A close-up view of steady state attitude error during worst power case scenario with an initial angular velocity of [0,-5,0] deg/sec

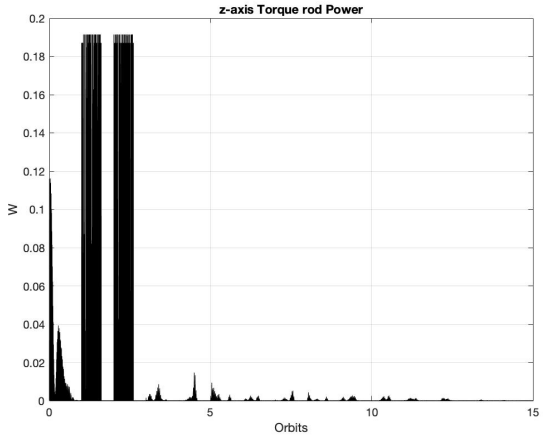
The torque rods show full power usage on the three-axis during the first orbit when the satellite is detumbling and during the orbits $2 - 3$ that it is spinning up in Fig. 5.35. After the satellite is spin-stabilized, the controller switches to the low-gain controller and reduces the power consumption. During eclipse, the control effort is not zero, and the EKF-based feedback is provided instead of sun sensor measurements.



(a) Torque rod power on x-axis



(b) Torque rod power on y-axis



(c) Torque rod power on z-axis

Figure 5.35: Torque rod power consumption of satellite with initial angular velocity of $[0, -5, 0]\ deg/sec$ with all perturbations (worst power case) after 15 orbits and power management strategy

5.7 Conclusion

In this section, the results of numerical simulations are presented. The first high-gain PD controller can command a rotation so that Iris's body frame's $-x$ axis aligns with the sun. The second low-gain PD controller maintains the attitude while gradually correcting the pointing.

In a fully operational satellite with an embedded EKF, two orbits are required to spin-up the satellite and settle the body rates with the relatively high perturbations and noise considered. In this case the accuracies of below $21\ deg$ are achievable in 6 orbits, which proves the reliability of the proposed control method.

The worst power case proves the functionality of the proposed method while changing the satellite's alignment from the $+y$ axis spin to $-x$ axis spin. Although this case would generate no power initially, the simulation proves the robustness of the planned scenario shown in flowchart of Fig. 5.1 to any unforeseen initial deployment state.

Chapter 6

Summary and Conclusion

The ADC subsystem of the Iris CubeSat is required to stabilize the spacecraft to $\pm 21\ deg$ accuracy in orienting the solar arrays toward the sun. As a result, the Iris CubeSat is modelled as an example in Simulink together with a Kalman filter for attitude estimation based on gyro measurements. Simulations characterize the attitude dynamics of the satellite, and a strategy is suggested to estimate the sun vector position with a real-time estimation algorithm. The algorithm is tested with simulated perturbation sources and sensor noise which robustly rejects the satellite's external perturbations and residual dipole to satisfy mission requirements. The desired attitude of the spacecraft requires the sun-direction vector to be aligned with the $-x$ axis. The system should be robust to environmental disturbances and perform the required attitude maneuvers. In order to design an attitude control system with power management strategy, the CubeSat is intended to be detumbled for 1 orbit, then start spinning-up to track $[1; 0; 0]\ deg/sec$ for two orbits. The spin stabilized satellite would then switch to a lower gain controller so that the magnetorquers effort wouldn't be maximum. The satellite benefits from gyric stiffness in order to maintain and improve its attitude.

Additionally, the estimator is considered effective after detumbling and spin-up process. In order to address the two-DOF sun sensor, a reduced order strategy is needed to reduce the order of the EKF algorithm from 6 to 5. Meanwhile, the accuracy of the results is improved. The algorithm runs in real-time and uses gyroscope measurements all the time, increasing the simulation robustness and providing better attitude accuracy. The sun sensor measurements are available during the illumination phase, and in the eclipse phase, the EKF algorithm estimates the attitude vector.

Thus, the overall motivation of this thesis is to set up an attitude determination and control subsystem with power management strategy for an underactuated spacecraft considering all the system constraints, dynamic uncertainties and external perturbation torques.

Finally, the following items were successfully accomplished in this study:

- I designed a simulator, initiating from the satellite launch from the ISS deployer, successfully detumbling the spacecraft and spinning up the satellite to the $[1, 0, 0]\ deg/sec$ spin rate.
- I designed a robust and reliable detumbling controller to damp the body rates with any initial angular velocity value in the presence of external disturbances and system uncertainties.
- I designed an active control law for an underactuated spacecraft with only magnetorquers to achieve three-axis stabilization in the orientation needed which provides $21\ deg$ pointing accuracy in 6 orbits which is the shortest possible time regarding the power constraints.
- I demonstrated that the torque rod power consumption for the Iris Spacecraft is reasonable and satisfactory. All values are in the predefined region and stay below the maximum $0.2\ W$ specified for the Iris mission. Additionally, the designed ADCS proved that Iris could survive the worst power case.
- I demonstrated that an underactuated spacecraft with an Extended Kalman Filter (EKF) produces an attitude estimate for nonlinear system dynamics with 3 inputs (3 rate gyros) to estimate sun vector position. The EKF block improves the attitude control accuracy to $0.18\ deg$.

6.1 Future Work

The presented research and the Simulink library lay a decent framework for succeeding work. First, an analysis of perturbation such as aerodynamic torque can be conducted to complete and

extend the achievements of this work. Additionally, more study and hardware tests need to be done to gain a detailed insight into the residual magnetic torque's characteristics. These are the factors that haven't been considered within this study.

The EKF block is a valuable structure for further investigation into different sensor frequency rates, system models or added sensors. The results are reliable and accurate since the equations are integrated as nonlinear equations.

In order to find the accurate value of the process noise, I suggest research on estimating the errors of the dynamic model discretization, linearization, model integration, and model uncertainty. This would ultimately result in a more accurate estimation of the process noise.

Finally, I recommend to integrate the EKF algorithm into a physical system, such as a drone, to plan and fly autonomously using a closed-loop control system with the estimated attitude. The actuators' saturation limit could be investigated simultaneously. The possible technical challenges for actuators were not addressed in this research which could be a baseline for future research.

Appendix A

Fine Pointing Perturbation Analysis

Four different simulation modes have been investigated to see the effect of adding each perturbations. The four simulation modes are presented in Table A.1. Dynamic uncertainties include any disturbance torque that is not considered in this study or is hard to estimate, such as aerodynamic drag torque.

Mode			
Simulator Mode	Residual Dipole Torque	Gravity gradient Torque	Dynamic uncertainties
1	×	×	×
2	✓	×	×
3	✓	✓	×
4	✓	✓	✓

Table A.1: 4 modes of Perturbation Analysis

In chapter 5, only the plots of the 4th mode plots are presented. The rest of the perturbation analysis (simulator modes 1 to 3) is discussed in this appendix.

A.1 Mode 1: Fine Pointing

Since the number of detumbling orbits has been determined and fixed to one orbit, the fine pointing controller will be discussed, and the results will be presented according to the modes in Table A.1. The body rates are shown in A.1. The CubeSat is expected to track the desired spin of $1\ deg/sec$ on the $-x$ axis. The detumbling controller reduces the angular velocity in the first orbit, but switching to PD control initially sends the CubeSat spinning about the $-x$ axis. Figure

A.1 validates this analysis.

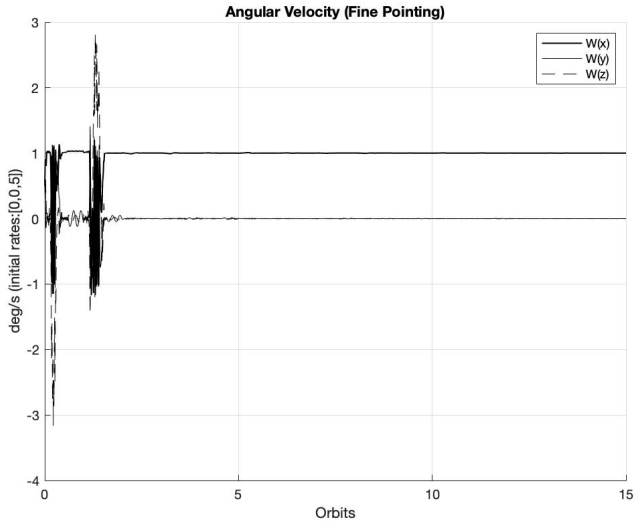


Figure A.1: Body rates of Iris during detumbling and fine pointing with initial angular velocity of $[5, 5, 5]\ deg/sec$ with no perturbation (Mode 1) after 15 orbits

The attitude angle will eventually reduce to $21\ deg$ after 3 orbits (Fig. A.2). Figure A.3 shows the residual attitude angle after 15 orbits which are about $0.6\ deg$. This result is promising and a reasonable basis to add perturbations to the next level.

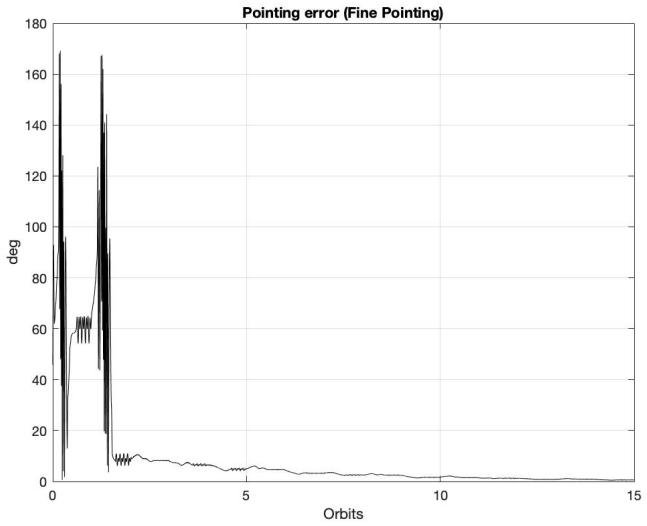


Figure A.2: Attitude Angle of satellite during detumbling and fine pointing with initial angular velocity of $[5, 5, 5]\ deg/sec$ with no perturbation (Mode 1) after 15 orbits

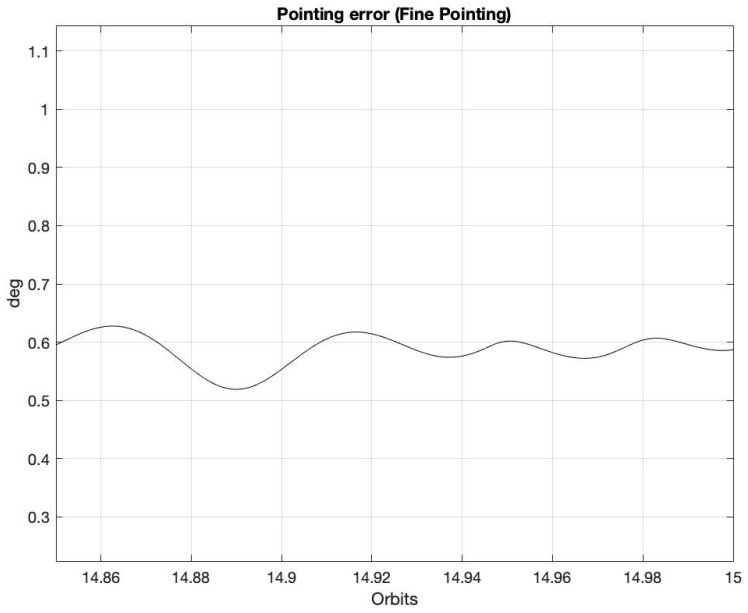
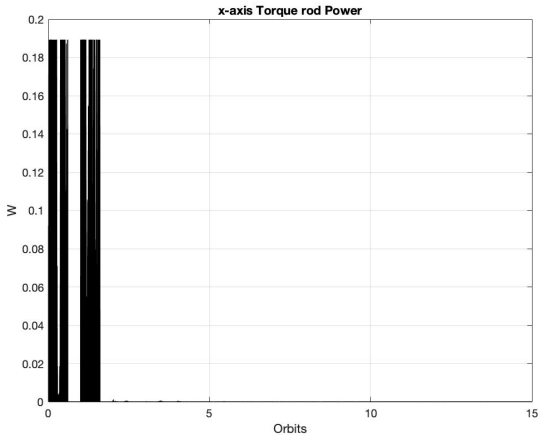
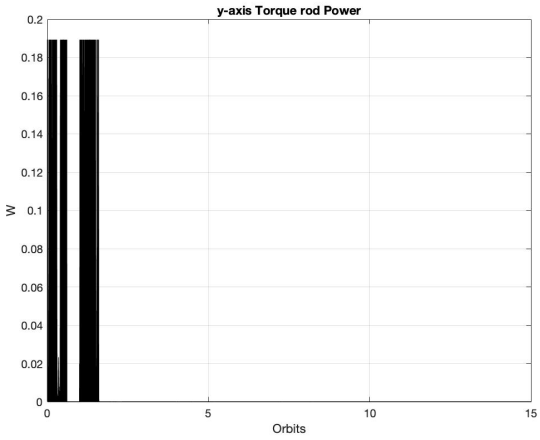


Figure A.3: A close up view of attitude angle during detumbling and fine pointing with initial angular velocity of $[5, 5, 5]\ deg/sec$ with no perturbation (Mode 1) after 15 orbits

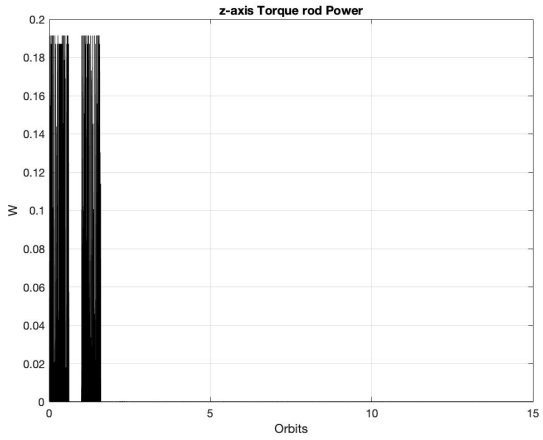
The magnetic actuators are mostly active during the detumbling and spin stabilizing phase (orbits $1-3$) as seen in Fig. A.4. When switching to low gain controller, the power draw decreases considerably.



(a) Torque rod power on x-axis



(b) Torque rod power on y-axis



(c) Torque rod power on z-axis

Figure A.4: Torque rod power consumption of satellite during detumbling with initial angular velocity of $[5, 5, 5]\ deg/sec$ with no perturbation (Mode 1) after 15 orbits and power management strategy

A.2 Mode 2: Fine Pointing

Referred to Table A.1, mode two is defined as adding residual dipole disturbance torque. Figure A.5 shows a promising result of fine pointing after adding the first disturbance torque. At the beginning of the third orbit, the instability has reduced, and the gyric stiffness has been achieved sooner. The steady-state error in attitude angle is shown in Fig. A.6. Little chattering is seen about the stability point, which seems to be related to the disturbance torque.

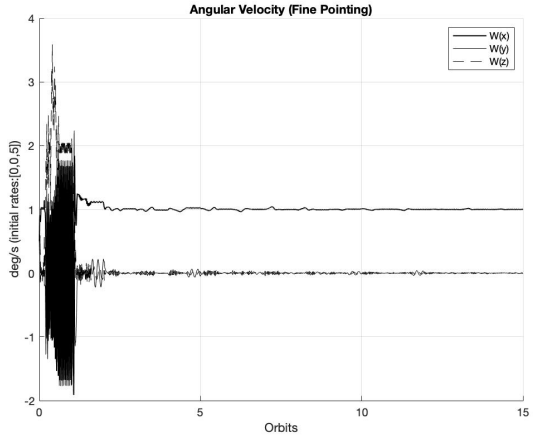


Figure A.5: Body rates of Iris during detumbling and fine pointing with initial angular velocity of $[5, 5, 5]\ deg/sec$ with residual dipole torque (Mode 2) after 15 orbits

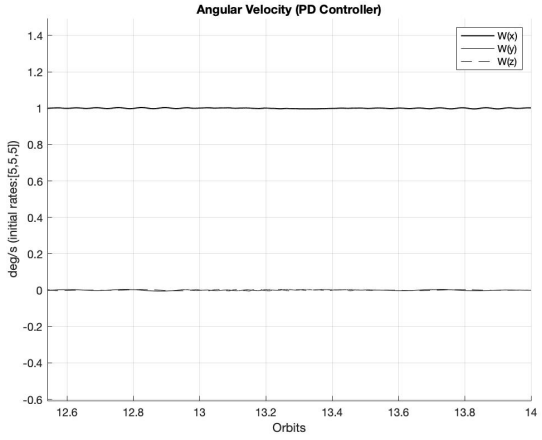


Figure A.6: A close up view of body rates during fine pointing with initial angular velocity of $[5, 5, 5]\ deg/sec$ with with residual dipole torque (Mode 2) after 15 orbits

Since the satellite gains better stability compared to mode 1, the attitude angle shown in Fig. A.7 seems to deliver a better result. For a better understating, Fig. A.8 shows a close-up view of the attitude angle between orbits 14 and 15. The pointing accuracy has remained at $\pm 5\ deg$.

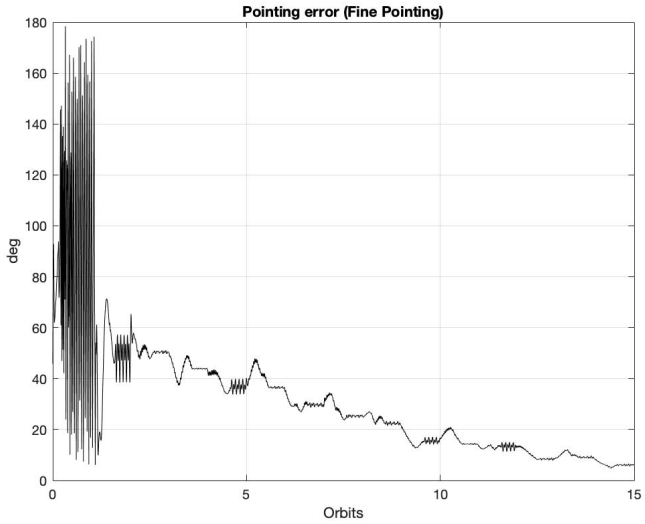


Figure A.7: Attitude Angle of satellite during detumbling and fine pointing with initial angular velocity of $[5, 5, 5]\ deg/sec$ with with residual dipole torque (Mode 2) after 15 orbits

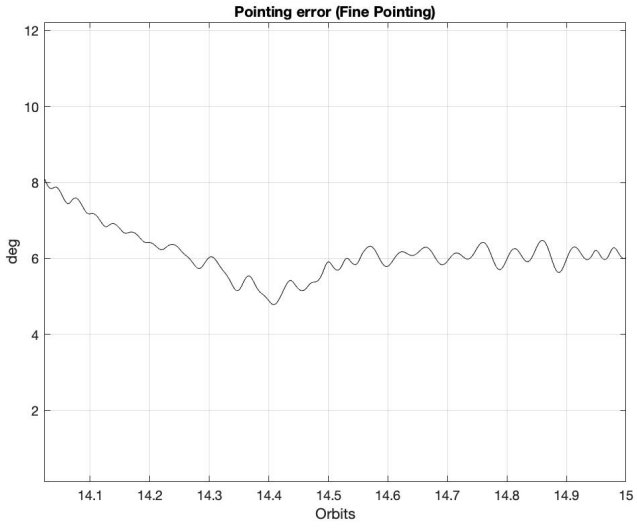
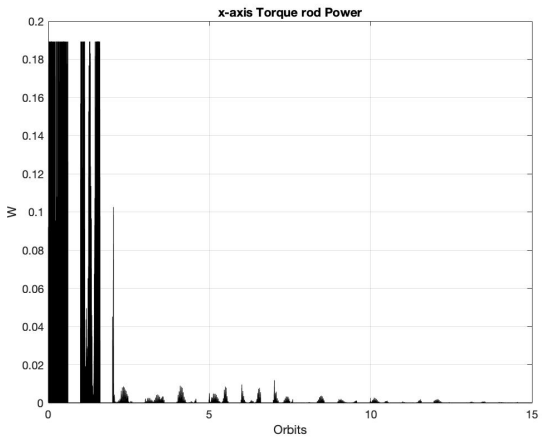
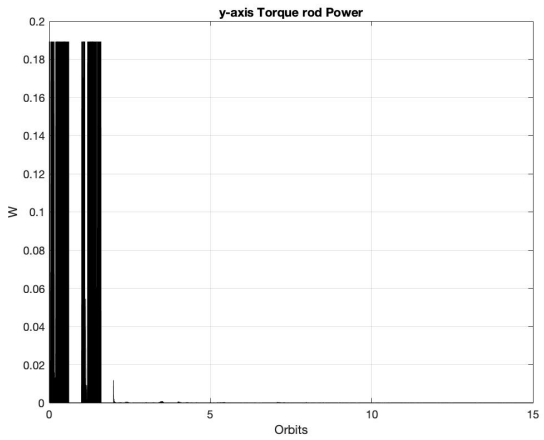


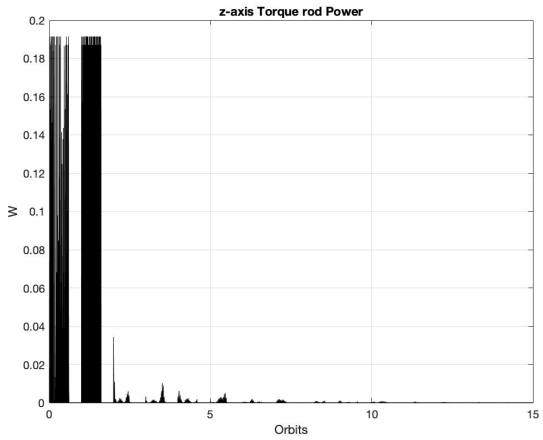
Figure A.8: A close up view of attitude angle during spin stabilization with initial angular velocity of $[5, 5, 5]\ deg/sec$ with with residual dipole torque (Mode 2) after 15 orbits



(a) Torque rod power on x-axis



(b) Torque rod power on y-axis



(c) Torque rod power on z-axis

Figure A.9: Torque rod power consumption of satellite during detumbling and fine pointing with initial angular velocity of $[5, 5, 5]\ deg/sec$ in mode 2 and power management strategy

A.3 Mode 3: Fine Pointing

In mode 3, gravity gradient torque is added, which is the dominant disturbance torque. The effect is seen in Fig. A.10, as the body rates need more time to settle. Moments of instability are seen in the third and fourth orbits. Ultimately, from the fifth orbit, the body rates track the desired angular velocity of $[1, 0, 0]\ deg/sec$.

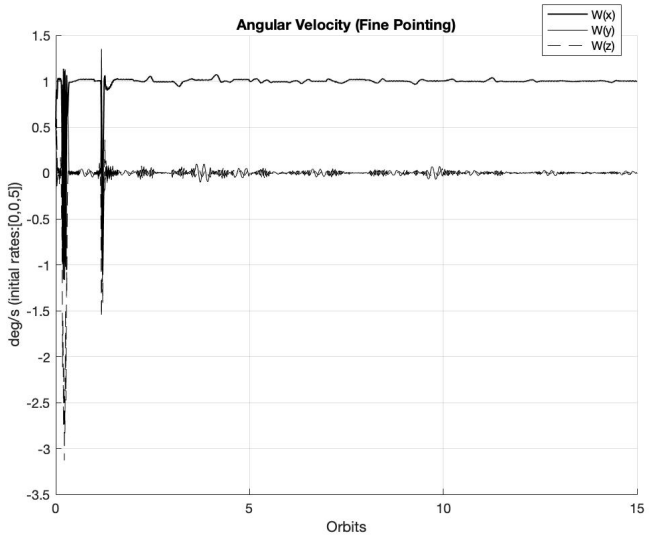


Figure A.10: Body rates of Iris during detumbling and fine pointing with initial angular velocity of $[5, 5, 5]\ deg/sec$ with residual dipole and gravity gradient torques (Mode 3) after 15 orbits

As shown in Fig. A.11 the attitude angle is more than $\pm 50\ deg$ during the first 4 orbits. Then the pointing window drops to $\pm 20\ deg$ after 12 orbits. As seen in Fig. A.12 the pointing accuracy drops to $8 - 14\ deg$ window after 15 orbits.

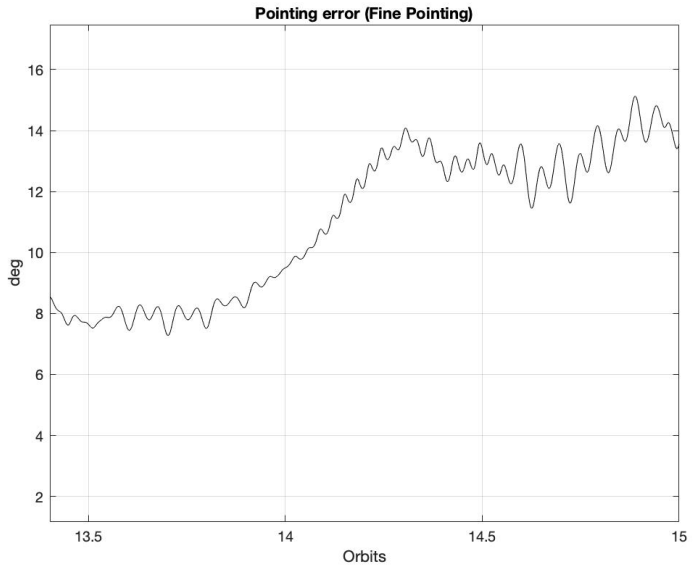


Figure A.12: Steady state attitude angle of satellite during Spin Stabilization with initial angular velocity of $[5, 5, 5]\ deg/sec$ with residual dipole and gravity gradient torques (Mode 3) after 15 orbits

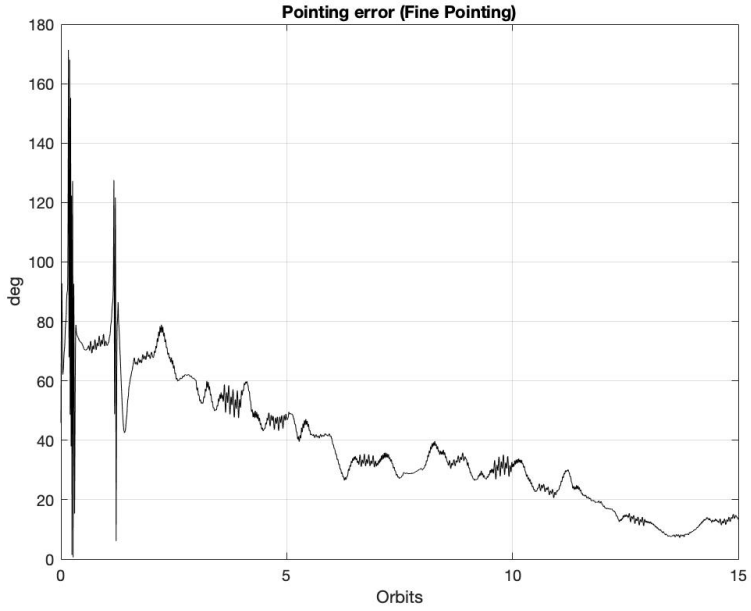
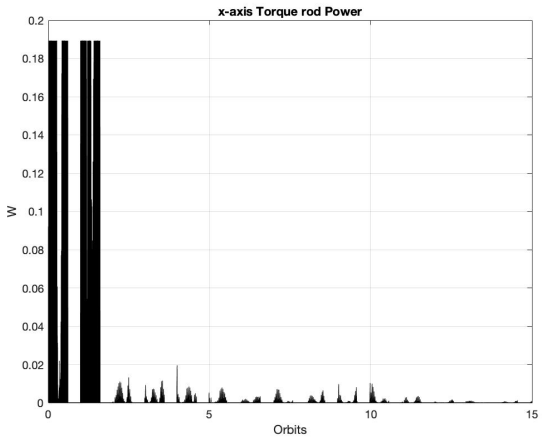
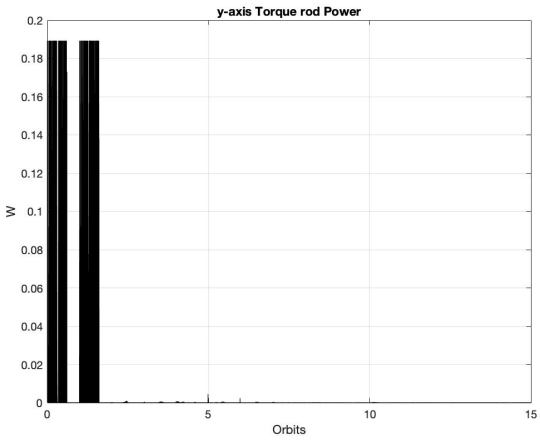


Figure A.11: Attitude angle of satellite during detumbling and fine pointing with initial angular velocity of $[5, 5, 5]$ deg/sec with residual dipole and gravity gradient torques (Mode 3) after 15 orbits

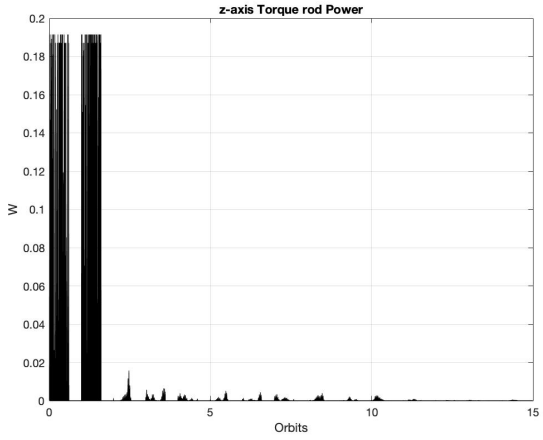
Magnetorquer's power consumption results shown in A.13 demonstrate active actuators during the first two orbits. Similar to the previous steps, the actuators consume little power after the satellite is stabilized, aligning with the $[-1, 0, 0]$ reference vector.



(a) Torque rod power on x-axis



(b) Torque rod power on y-axis



(c) Torque rod power on z-axis

Figure A.13: Torque rod power consumption of satellite during detumbling and fine pointing with initial angular velocity of $[5, 5, 5]\ deg/sec$ in mode 3 and power management strategy

Bibliography

[1] M. Sweeting, "Modern small satellites-changing the economics of space," *Proceedings of the IEEE*, vol. 106, no. 3, pp. 343–361, 2018.

[2] A. S. Gohardani, "Small satellites: Observations and considerations," *AIAA Aerospace Sciences Meeting, 2018*, no. 210059, pp. 1–12, 2018. DOI: 10.2514/6.2018-1937.

[3] G. Petroni and S. Santini, "Innovation and change? The evolution of Europe's small satellite manufacturers," *Space Policy*, vol. 28, no. 1, pp. 25–32, 2012, ISSN: 0265-9646. DOI: https://doi.org/10.1016/j.spacepol.2011.12.008. [Online]. Available: https://www.sciencedirect.com/science/article/pii/S0265964611001287.

[4] A. Poghosyan and A. Golkar, "CubeSat evolution: Analyzing CubeSat capabilities for conducting science missions," *Progress in Aerospace Sciences*, vol. 88, pp. 59–83, 2017, ISSN: 03760421. DOI: 10.1016/j.paerosci.2016.11.002. [Online]. Available: http://dx.doi.org/10.1016/j.paerosci.2016.11.002.

[5] M. Sweeting, "Uosat microsatellite missions," *Electronics & communication engineering journal*, vol. 4, no. 3, pp. 141–150, 1992.

[6] R. Sandau, K. Brieß, and M. D'Errico, "Small satellites for global coverage: Potential and limits," *ISPRS Journal of Photogrammetry and Remote Sensing*, vol. 65, no. 6, pp. 492–504, 2010, ISSN: 09242716. DOI: 10.1016/j.isprsjprs.2010.09.003. [Online]. Available: http://dx.doi.org/10.1016/j.isprsjprs.2010.09.003.

[7] D. V. A. Raghavamurthy and S. S. Rao, *Advances in Small Satellite Technologies*. 2020, p. 522, ISBN: 978-981-15-1723-5. [Online]. Available: http://link.springer.com/10.1007/978-981-15-1724-2.

[8] A. Antonello, L. Olivieri, and A. Francesconi, "Development of a low-cost sun sensor for nanosatellites," *Acta Astronautica*, vol. 144, pp. 429–436, 2018, ISSN: 00945765. DOI: 10.1016/j.actaastro.2018.01.003. [Online]. Available: https://doi.org/10.1016/j.actaastro.2018.01.003.

[9] L. He, W. Ma, P. Guo, and T. Sheng, "Developments of attitude determination and control system of microsats: A survey," *Proceedings of the Institution of Mechanical Engineers. Part I: Journal of Systems and Control Engineering*, vol. 235, no. 10, pp. 1733–1750, 2021, ISSN: 20413041. DOI: 10.1177/0959651819895173.

[10] M. F. Mehrjardi and M. Mirshams, "Design and manufacturing of a research magnetic torquer rod," in *Fourth International Conference on Experimental Mechanics*, SPIE, vol. 7522, 2010, pp. 543–549.

[11] B. A. Roberts, J. W. Kruk, T. B. Ake, T. S. Englar, B. F. Class, and D. M. Rovner, "Three-axis attitude control with two reaction wheels and magnetic torquer bars," *Collection of Technical Papers - AIAA Guidance, Navigation, and Control Conference*, vol. 4, pp. 2465–2472, 2004. DOI: 10.2514/6.2004-5245.

[12] T. Flatley, W. Morgenstern, A. Reth, and F. Bauer, "A b-dot acquisition controller for the radarsat spacecraft," in *NASA conference publication*, NASA, vol. 3345, 1997, pp. 79–90.

[13] F. Martel, P Pal, and M. Psiaki, "Active Magnetic Control System for Gravity Gradient Stabilized Spacecraft," in *Proceedings of 2nd Annual AIAA/USU Conference on Small Satellites*, 1988. [Online]. Available: http://digitalcommons.usu.edu/smallsat/1988/all1988/19/.

[14] E. Silani and M. Lovera, "Magnetic spacecraft attitude control: A survey and some new results," *Control Engineering Practice*, vol. 13, no. 3, pp. 357–371, 2005, ISSN: 09670661. DOI: 10.1016/j.conengprac.2003.12.017. [Online]. Available: https://www.sciencedirect.com/science/article/pii/S0967066103002922.

[15] N Sivaprakash and J Shanmugam, "Neural network based three axis satellite attitude control using only magnetic torquers," in *AIAA/IEEE Digital Avionics Systems Conference - Proceedings*, vol. 2, 2005, ISBN: 0780393074. DOI: 10.1109/DASC.2005.1563440. [Online]. Available: https://ieeexplore.ieee.org/abstract/document/1563440/.

[16] A. Moran, H. Odagaki, and M. Hayase, "Dynamics and control of underactuated brachiation robots," in *IEEE/ASME International Conference on Advanced Intelligent Mechatronics, AIM*, IEEE, 1997, p. 98. DOI: 10.1109/aim.1997.652965.

[17] R. Wisniewski, "Linear time-varying approach to satellite attitude control using only electromagnetic actuation," *Journal of Guidance, Control, and Dynamics*, vol. 23, no. 4, pp. 640–647, 2000.

[18] M. Wood, W. H. Chen, and D. Fertin, "Model predictive control of low earth orbiting spacecraft with magneto-torquers," *Proceedings of the IEEE International Conference on Control Applications*, pp. 2908–2913, 2006. DOI: 10.1109/CACSD-CCA-ISIC.2006.4777100.

[19] P. C. Hughes, *Spacecraft attitude dynamics*. Courier Corporation, 2012.

[20] J.-J. E. J.-J. E. Slotine and W. Li, "Applied nonlinear control," p. 459, 1991.

[21] P. J. Camillo and F. L. Markley, "Orbit-averaged behavior of magnetic control laws for momentum unloading," *Journal of Guidance, Control, and Dynamics*, vol. 3, no. 6, pp. 563–568, 1980, ISSN: 07315090. DOI: 10.2514/3.19725.

[22] R. Wiśniewski, "Three-Axis Satellite Attitude Control Based on Magnetic Torquing - Linear Optimal Approach *," *IFAC Proceedings Volumes*, vol. 29, no. 8, pp. 91–96, 1996, ISSN: 14746670. DOI: 10.1016/s1474-6670(17)43682-2.

[23] M. Y. Ovchinnikov and D. S. Roldugin, "A survey on active magnetic attitude control algorithms for small satellites," *Progress in Aerospace Sciences*, vol. 109, 2019, ISSN: 03760421. DOI: 10.1016/j.paerosci.2019.05.006.

[24] R. E. Fischell, "Magnetic Damping of the Angular Motions of Earth Satellites," *ARS Journal*, vol. 31, no. 9, pp. 1210–1217, 1961. DOI: 10.2514/8.5759. [Online]. Available: https://arc.aiaa.org/doi/abs/10.2514/8.5759.

[25] S. Rawashdeh and J. Lumpp, "Nano-satellite passive attitude stabilization systems design by orbital environment modeling and simulation," in *AIAA Infotech@ Aerospace 2010*, 2010, p. 3413.

[26] P. Wang and Y. B. Shtessel, "Satellite attitude control using only magnetorquers," in *Proceedings of the American Control Conference*, vol. 1, 1998, pp. 222–226, ISBN: 0780345304. DOI: 10.1109/ACC.1998.694663.

[27] A. Farhat, J Ivase, Y Lu, and A Snapp, "Attitude Determination and Control System for CubeSat," *BS.c Thesis, Worcester Polytechnic University*, pp. 180–184, 2013. [Online]. Available: https://digital.wpi.edu/downloads/x633f2762.

[28] E. M. Vidal, "Development of models for Attitude Determination and Control System components for CubeSat applications," *MSc Thesis, Lulea University of Technology*, 2017. [Online]. Available: https://www.diva-portal.org/smash/get/diva2:1142450/FULLTEXT01.pdf.

[29] M. L. Psiaki, "Nanosatellite Attitude Stabilization Using Passive Aerodynamics and Active Magnetic Torquing," *Journal of Guidance, Control and Dynamics*, vol. 27, no. 3, 2004. DOI: 10.2514/1.1993. [Online]. Available: https://arc.aiaa.org.

[30] A. Sofyali and E. M. Jafarov, "Three-axis attitude control of a small satellite by magnetic PD-like controller integrated with passive pitch bias momentum method," *RAST 2011 - Proceedings of 5th International Conference on Recent Advances in Space Technologies*, pp. 307–311, 2011. DOI: 10.1109/RAST.2011.5966846.

[31] S. Carletta and P. Teofilatto, "Design and Numerical Validation of an Algorithm for the Detumbling and Angular Rate Determination of a CubeSat Using Only Three-Axis Magnetometer Data," *International Journal of Aerospace Engineering*, vol. 2018, 2018, ISSN: 16875974. DOI: 10.1155/2018/9768475.

[32] M. C. Santiago, L. S. Velasco, and A. R. Aranda, "Low cost magnetic simulator for attitude control," in *Proceedings of 2018 Technologies Applied to Electronics Teaching, TAEE 2018*, Institute of Electrical and Electronics Engineers Inc., 2018, ISBN: 9781538609286. DOI: 10.1109/TAEE.2018.8476113.

[33] A. R. Walker, P. T. Putman, and K. Cohen, "Solely magnetic genetic/fuzzy-attitude-control algorithm for a CubeSat," *Journal of Spacecraft and Rockets*, vol. 52, no. 6, pp. 1627–1639, 2015, ISSN: 15336794. DOI: 10.2514/1.A33294.

[34] D. K. Giri and M. Sinha, "Robust backstepping magnetic attitude control of satellite subject to unsymmetrical mass properties," *Journal of Spacecraft and Rockets*, vol. 56, no. 1, pp. 298–305, 2019. [Online]. Available: https://doi.org/10.2514/1.A34298.

[35] G. E. Cruz and D. Bernstein, "Retrospective cost adaptive control of spacecraft attitude using magnetic actuators," in *AIAA Guidance, Navigation, and Control (GNC) Conference*, 2013, p. 4563. [Online]. Available: https://arc.aiaa.org/doi/10.2514/6.2013-4563.

[36] A. De Ruiter, "A fault-tolerant magnetic spin stabilizing controller for the JC2Sat-FF mission," *Acta Astronautica*, vol. 68, no. 1-2, pp. 160–171, 2011, ISSN: 00945765. DOI: 10.1016/j.actaastro.2010.07.012. [Online]. Available: https://www.sciencedirect.com/science/article/pii/S0094576510002687.

[37] H. S. Ousaloo, "Magnetic attitude control of dynamically unbalanced spinning spacecraft during orbit raising," *Journal of Aerospace Engineering*, vol. 27, no. 2, pp. 262–278, 2014.

[38] H. Bolandi and B. G. Vaghei, "Stable supervisory-adaptive controller for spinning satellite using only magnetorquers," *IEEE Transactions on Aerospace and Electronic Systems*, vol. 45, no. 1, pp. 192–208, 2009. DOI: 10.1109/TAES.2009.4805273.

[39] D. M. Torczynski, R. Amini, and P. Massioni, "Magnetorquer based attitude control for a nanosatellite testplatform," *AIAA Infotech at Aerospace 2010*, 2010. DOI: 10.2514/6.2010-3511. [Online]. Available: http://arc.aiaa.org.

[40] Y. Mimasu, J. C. Van Der Ha, and T. Narumi, "Attitude determination by magnetometer and gyros during eclipse," *AIAA/AAS Astrodynamics Specialist Conference and Exhibit*, 2008. DOI: 10.2514/6.2008-6932.

[41] S. Ni and C. Zhang, "Attitude determination of nano satellite based on gyroscope, sun sensor and magnetometer," *Procedia Engineering*, vol. 15, pp. 959–963, 2011, ISSN: 18777058. DOI: 10.1016/j.proeng.2011.08.177.

[42] M. Abdelrahman and S.-Y. Park, "Integrated attitude determination and control system via magnetic measurements and actuation," *Acta Astronautica*, vol. 69, no. 3-4, pp. 168–185, 2011.

[43] C. Hajiyev, D. Cilden-Guler, and Y. Somov, "Attitude determination of nanosatellites in the sun-eclipse phases," *Proceedings of 8th International Conference on Recent Advances in Space Technologies, RAST 2017*, pp. 397–401, 2017. DOI: 10.1109/RAST.2017.8002990.

[44] D Messmann, T Gruebler, F Coelho, *et al.*, "Advances in the development of the attitude determination and control system of the cubesat move-ii," in *Proceedings of the 7th European Conference for Aeronautics and Space Sciences (EUCASS), Milan, Italy*, 2017, pp. 3–6.

[45] N. Sugimura, T. Kuwahara, and K. Yoshida, "Attitude determination and control system for nadir pointing using magnetorquer and magnetometer," in *2016 IEEE Aerospace Conference*, 2016, pp. 1–12. DOI: 10.1109/AERO.2016.7500665.

[46] D. Ivanov, M. Ovchinnikov, and D. Roldugin, "Three-axis attitude determination using magnetorquers," *Journal of Guidance, Control, and Dynamics*, vol. 41, no. 11, pp. 2455–2462, 2018.

[47] D. Ivanov, D. Roldugin, S. Tkachev, *et al.*, "Attitude motion and sensor bias estimation onboard the siriussat-1 nanosatellite using magnetometer only," *Acta Astronautica*, vol. 188, pp. 295–307, 2021.

[48] S. Chirame, A. A. Joshi, R. M. K. Verma, *et al.*, "Closed-loop simulation for attitude control of nano-satellite," in *Advances in Small Satellite Technologies*, Springer, 2020, pp. 87–97.

[49] S Garcia-Gonzalez and G Sanchez-Arriaga, "Attitude determination and control for the deployment preparation phase of a space tether mission," *Acta Astronautica*, vol. 193, pp. 381–394, 2022, ISSN: 0094-5765. DOI: https://doi.org/10.1016/j.actaastro.2022.01.011. [Online]. Available: https://www.sciencedirect.com/science/article/pii/S009457652200011X.

[50] A. Yahyaabadi, M. Driedger, N. Turenne, *et al.*, "ManitobaSat-1: A Novel Approach for Technology Advancement," *IEEE Potentials*, vol. 39, no. 4, pp. 17–23, 2020, ISSN: 15581772. DOI: 10.1109/MPOT.2020.2986093.

[51] S. A. Connell, E. A. Cloutis, D. M. Applin, *et al.*, "Overview Of The 3-U Manitobasat-1 Cubesat Payload To Study The Effects Of Space Weathering On Geological Samples," in *51st Lunar and Planetary Science Conference*, 2020, p. 1773.

[52] Y. J. Morton, F. van Diggelen, J. J. Spilker Jr, B. W. Parkinson, S. Lo, and G. Gao, *Position, Navigation, and Timing Technologies in the 21st Century: Integrated Satellite Navigation, Sensor Systems, and Civil Applications*. 2021, ISBN: 1119458412.

[53] Y. Yang, *Spacecraft Modeling, Attitude Determination, and Control Quaternion-based Approach*. CRC Press, 2019. DOI: 10.1201/9780429446580.

[54] N. Najafizadeh, R. Clark, S. Connell, N. Turenne, and P. Ferguson, "Spin Stabilized Sun Pointing CubeSat For Space Geology," in *16th International Conference on Space Operations, Cape Town, South Africa – 3 - 5 May 2021*, 2021.

[55] V. Parthasarathy, "Virtual ground station for automated spacecraft operations," 2021. [Online]. Available: https://mspace.lib.umanitoba.ca/xmlui/handle/1993/35224.

[56] W.-Y. Chang, "The state of charge estimating methods for battery: A review," *International Scholarly Research Notices*, vol. 2013, 2013.

[57] H. Moodi and D. Bustan, "On deterministic approaches to attitude determination with magnometer in eclipse," in *2010 Chinese Control and Decision Conference*, IEEE, 2010, pp. 3754–3759.

[58] K. Zhai, "Angular velocity determination of spinning solar sails using only a sun sensor," *Chinese Journal of Aeronautics*, vol. 30, no. 1, pp. 412–418, 2017, ISSN: 10009361. DOI: 10.1016/j.cja.2016.12.009. [Online]. Available: http://dx.doi.org/10.1016/j.cja.2016.12.009.

[59] G. Welch, G. Bishop, *et al.*, "An introduction to the kalman filter," 1995.

[60] R. G. Brown and P. Y. Hwang, "Introduction to random signals and applied kalman filtering: With matlab exercises and solutions," *Introduction to random signals and applied Kalman filtering: with MATLAB exercises and solutions*, Wiley, 1997.

[61] C. Van Loan, "Computing integrals involving the matrix exponential," *IEEE transactions on automatic control*, vol. 23, no. 3, pp. 395–404, 1978.